Czech Technical University in Prague
Faculty of Nuclear Sciences and Physical Engineering

DISSERTATION

Prague 2024   Ing. Sebastian Lorenz

Czech Technical University in Prague
Faculty of Nuclear Sciences and Physical Engineering

DISSERTATION

Development of gas targets for laser-driven electron acceleration

Prague 2024   Ing. Sebastian Lorenz

Bibliografický záznam

Autor: Ing. Sebastian Lorenz, České vysoké učení technické v Praze, Fakulta jaderná a fyzikálně inženýrská, Katedra fyzikální elektroniky

Název práce: Vývoj plynových terčů pro urychlování elektronů laserem

Studijní program: Aplikace přírodních věd

Studijní obor: Fyzikální inženýrství

Školitel: prof. Ing. Jiří Limpouch, CSc., České vysoké učení technické v Praze, Fakulta jaderná a fyzikálně inženýrská, Katedra fyzikální elektroniky

Školitel specialista: MSc. Gabriele Maria Grittani, Ph.D., Extreme Light Infrastructure ERIC, ELI Beamlines Facility

Akademický rok: 2023/2024

Počet stran: 102

Klíčová slova: urychlování elektronů laserem, plynový terč, hydrodynamická simulace, výpočetní tomografie, diagnostika plazmatu

Abstrakt (CZ)

Urychlováním elektronů prostřednictvím metody LWFA (Laser Wakefield Electron Acceleration) lze dosáhnout produkce ultra krátkých a vysoce energetických svazků na velmi krátkých vzdálenostech. Tato disertační práce pojednává o vývoji plynových terčů pro LWFA urychlování. Teoretická část práce pojednává o škálovacích zákonech pro návrh LWFA urychlovače a diskutuje technologické limity plynových terčů používaných v současných experimentech. Pro návrh terčů s požadovaným hustotním profilem plynu se používají numerické řešiče Navier-Stokesových rovnic. Pro specifické případy, kdy plyn dosáhne velmi nízké koncentrace, se pak simulace kontinua nahrazuje metodami molekulární dynamiky. Pro experimentální stanovení plynových profilů terčů se používá vysoce citlivé interferometrické měření a algoritmy 3D tomografické rekonstrukce. Tímto způsobem bylo navrženo několik konstrukčních řešení terčů pro různé mechanismy urychlování.

Druhá část práce popisuje vykonané experimentální aktivity. V rámci vývoje ultrarychlé optické diagnostiky plazmatu s využitím metody CAfCA (Compression after Compressor Approach) byl proveden test na PW laseru J-KAREN-P. Během experimentu bylo dosaženo vylepšení poměru intenzity diagnostického svazku k intenzitě vlastní emise záření a bylo dokázáno, že si nový diagnostický svazek zároveň udrží dostatečnou kvalitu pro diagnostiku plazmatu terčů. Další dva experimenty konané v ELI-Beamlines měly za úkol uvést do provozu dva různě škálované LWFA urychlovače elektronů. V urychlovači ELI-ELBA poháněném PW laserem L3-HAPLS byly vygenerovány elektronové svazky s energií v řádu GeV a opakovací frekvencí 3.3 Hz, což je první krok k vybudování zařízení, které dokáže srážet energetické elektrony s fotony. V urychlovači ALFA poháněném TW laserovým systémem L1-Allegra s opakovací frekvencí 1 kHz byly vygenerovány svazky elektronů s energiemi až 50 MeV, což je v kategorii kHz urychlování světově unikátní. Tento urychlovač umožní rozvíjet nové biomedicínské aplikace.

Abstract (EN)

Laser wakefield electron acceleration (LWFA) is a compact technique for producing ultra-short ultra-relativistic electron beams. This thesis deals with the design and development of gas targets for LWFA. The theory of the LWFA and its scaling laws are reviewed in the first part. It also describes the technological aspects of the targets, such as gas load in the vacuum chamber and manufacturing precision, and limits of up-to-date LWFA experiments. The computational fluid dynamics simulations implementing Navier-Stokes equations are used for the design of the targets. In specific cases, the molecular-based simulation approach is also involved. Advanced interferometric methods and 3D tomographic reconstruction algorithms are used for the experimental characterization of the target prototypes. Various target designs are investigated.

The second part of the thesis describes experimental activities. The ultra-fast optical probe diagnostics implementing Compression after Compressor Approach is investigated. During an experiment with the J-KAREN-P laser, we improved the probe-to-self-emission intensity ratio and we proved that the compressed probe pulse kept the high quality necessary for gas target plasma probing. Two electron acceleration beamlines were recently commissioned in the ELI-Beamlines facility. GeV-class electron acceleration with a 3.3 Hz repetition rate has been demonstrated in ELI-ELBA beamline with L3-HAPLS PW-class laser as a first step towards high-intensity electron-laser collider. Up to 50 MeV electron beams at 1 kHz have been demonstrated in the ALFA accelerator driven by the TW-class high repetition rate system L1-Allegra. Such electron beams have the potential to enable biomedical applications.

Contents

Introduction

Electron accelerators stand as fundamental technologies in modern society, finding daily applications across various fields. They are instrumental in researching the structure of matter, conducting nondestructive testing, generating X-ray radiation, facilitating medical imaging, and even aiding in the radiotherapy of certain tumors. While linear and circular (e.g., synchrotron) electron accelerators have long been established, these conventional accelerators face challenges when aiming to achieve multi-GeV-scale energies. Mainly, their size grows significantly, reaching kilometers, due to limitations in the maximum attainable accelerating gradient, typically around 100 MV/m. This results in complex and expensive construction and maintenance hindering the realization of compact accelerators for applications such as free electron lasers, Thomson scattering X-ray sources, and high-energy electron accelerators for radiotherapy.

Laser-plasma acceleration has emerged as a promising technology that can overcome the conventional accelerators' limitations. Laser Wakefield Electron Acceleration (LWFA)[1] exploits the ponderomotive force of an intense laser pulse to excite a plasma wave within an under-dense plasma. Subsequently, the strong electrostatic field within the plasma wave accelerates electrons to high energies.

Recent years have seen an extensive global effort to explore the potential of LWFAs, resulting in remarkable achievements. These range from the demonstration of the first GeV laser-driven electron beams [2, 3, 4], to the acceleration of multi-GeV electrons via plasma guiding [5, 6], and even the realization of free electron lasing [7]. Motivated by these exceptional results, efforts have focused on translating the electron sources into practical applications. This has led to demonstrations of stable electron beam operation lasting over 24 hours [8], as well as the acceleration of quasi-monoenergetic (QME) electron beams at a 1 kHz repetition rate [9, 10].

To successfully perform LWFA, it is crucial to create a particular plasma density profile in which the acceleration occurs. The profile is created by a gas target device in which the density distribution of the gas needs to be precisely set. Gas targets can be designed utilizing analytical models and computational fluid dynamics (CFD) numerical simulations. The main advantage of the simulations is that they are cost-effective and fast in comparison to experimental measurements. Then, after precise manufacturing, the interferometric methods[11, 12] together with tomographic reconstruction algorithms[13, 14, 15] are typically used to characterize the particle number density in the gas target. After successful development, the target is implemented into the complex accelerator setup. After the experimental campaign, the data obtained from laser-plasma interaction diagnostics are then typically benchmarked with PIC plasma

simulations.

The direct investigation of the laser-plasma interactions in LWFA is especially challenging considering that the plasma wave is micrometer-scale size and its femtosecond-scale temporal evolution must be resolved simultaneously. The interaction region can be recorded by illuminating it with a second laser pulse, typically called a "probe pulse", and imaging the region onto a sensor. To record fine details of the interaction the imaging system used must achieve the requisite spatial resolution and the probe pulse used as illumination must have a pulse duration significantly shorter than that of the driving laser pulse.

The laser wakefield acceleration program at ELI-Beamlines facility benefits from the future availability of four unique high-power laser systems that make possible the investigation of LWFA in a broad range of parameters, ranging from mJ to kJ in pulse energy. The experiments driven by the PW-class laser system L3-HAPLS (Ti:Sapph, 30 J, 30 fs, 10 Hz) are performed at the ELI-ELBA beamline, and aim at the counter-propagation of laser-accelerated GeV electron beams with high-intensity laser pulses. These experiments are designed to study novel regimes of electromagnetic field interaction with matter and quantum vacuum. The LWFA experiments driven by the TW-class high rep-rate laser system L1-Allegra (100 mJ, 15 fs, 1 kHz) are oriented towards applications in the biomedical field, and to the investigation of the interaction of high-power lasers with near-critical density plasmas.

The thesis is composed of six chapters. The first chapter describes the physics behind the LWFA acceleration, presents techniques to inject electrons into the accelerating phase to reach high-quality electron beams and, in the end, gives an overview of scaling laws used to design the LWFA accelerator. The second chapter describes the current technology that is used for building the gas target for electron acceleration and comments on the limits of the gas target technology. Then it reviews the state-of-the-art of the target technology used in recent LWFA experiments. The third chapter describes in detail the methods that are used for advanced target development. It covers both, the numerical simulation tools and experimental density profile measurements. The fourth chapter presents the laser-plasma interaction experiment, where ultra-fast optical probe diagnostics have been implemented and tested. This probing technique can be favorably used in the LWFA experiments. The fifth chapter then introduces six particular gas targets that were developed for laser wakefield electron acceleration. The last chapter presents in detail two LWFA beamlines accommodated in ELI-Beamlines and mentions the results of their recent commissioning experiments. In conclusion, the full gas target development process and the implementation into electron acceleration beamlines are summarized.

Chapter 1

Laser Wakefield Electron Acceleration

The laser wakefield electron acceleration (LWFA) was first proposed by Tajima and Dawson in 1979 [1]. The proposed mechanism is based on ultra-short, high-intensity laser pulses focused in an underdense plasma. There the laser ponderomotive force sets up a charge separation by displacing electrons, resulting in the excitation of a large-amplitude plasma wave (wakefield) propagating behind the laser pulse. The longitudinal electric field in the wakefield can accelerate electrons to relativistic energies over short distances (the scheme of the process is described in Figure 1.1).

In this chapter, first, the physics involved in the laser-plasma interaction is described. Then, an overview of controlled injection techniques are presented. In the last section, the scaling laws for the design of an electron accelerator are presented.

1.1 Lasers, plasma waves and wave breaking

The laser driver

LWFA is driven by ultra-short high-intensity laser pulses. A laser pulse can be described by an electromagnetic field

$$\vec{E}(\vec{x}, t) = \vec{E}_A(\vec{x}, t) \cos(\omega_0 t - \vec{k} \cdot \vec{x} + \phi_0) \tag{1.1}$$

$$\vec{B}(\vec{x}, t) = \vec{B}_A(\vec{x}, t) \cos(\omega_0 t - \vec{k} \cdot \vec{x} + \phi_0), \tag{1.2}$$

where $\vec{E}_A(\vec{x}, t)$ and $\vec{B}_A(\vec{x}, t)$ denote the electric and magnetic amplitudes, ω_0 is the angular frequency, $\vec{k}$ is the wave vector and ϕ_0 is the absolute phase. The angular frequency ω_0 of the field oscillation is related to its wavelength λ_0 via $\omega_0 = 2\pi c/\lambda_0$. In the case of a laser pulse propagating along $z = 0$ with a Gaussian profile (in time and spatial domain) its electric field could be written as

$$\vec{E}_A(\vec{x}, t) = E_0 \cdot e^{-\frac{t^2}{\tau_0^2}} \cdot e^{-\frac{x^2}{w_{x,0}^2}} \cdot e^{-\frac{y^2}{w_{y,0}^2}}, \tag{1.3}$$

where τ_0, $w_{x,0}$ and $w_{y,0}$ are, respectively, $1/e$ of the pulse duration and beam size.
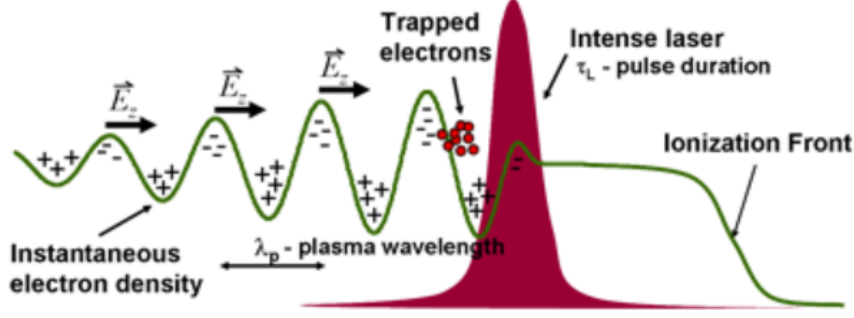
Figure 1.1: Scheme of the interaction of intense laser pulse with the initially neutral gas. Gas is ionized by the front of the laser pulse and the wakefield is set up behind the laser. The plasma wave with strong electric fields then traps electrons and accelerates them to very high energies. The plasma wave is excited most efficiently when the plasma wavelength is comparable to the laser pulse duration. Image taken from [16].

In vacuum the field described by Eqs. 1.1 and 1.2 has to fulfill the Maxwell equations (in the absence of any charge or current) and the electromagnetic wave equation which comes from them. The light pulse can also be described by a vector potential $\vec{A}$ and a scalar potential Φ which are defined as

$$\vec{E} = -\frac{\partial}{\partial t}\vec{A} - \nabla\Phi \tag{1.4}$$

$$\vec{B} = \nabla \times \vec{A}. \tag{1.5}$$

To find a solution for the electromagnetic wave equation, the Eqs. 1.4 and 1.5 are combined with the Lorentz gauge condition

$$\nabla \cdot \vec{A} + \epsilon_0 \frac{\partial}{\partial t}\Phi = 0, \tag{1.6}$$

where ϵ_0 is the permittivity of free space. A solution for the electromagnetic wave is then [17]

$$\vec{A}(\vec{x}, t) = -\vec{A}_A \sin(\omega_0 t - \vec{k} \cdot \vec{x} + \phi_0) \tag{1.7}$$

$$\Phi(\vec{x}, t) = 0, \tag{1.8}$$

where

$$A_A = \frac{1}{\omega_0}E_A = \frac{c}{\omega_0}B_A, \tag{1.9}$$

where c is the speed of light.

The laser intensity I, which plays a crucial role in LWFA, is defined as the modulus of the energy flux density averaged over one oscillation period T

$$I = \epsilon_0 c\langle E^2\rangle_T. \tag{1.10}$$

When the laser pulse interacts with matter the electric and magnetic field of the electromagnetic wave pushes the electrons by the Lorentz force

$$\frac{d\vec{p}_e}{dt} = -e(\vec{E} + \vec{v}_e \times \vec{B}), \tag{1.11}$$

4

where e is the elementary charge, $\vec{p}_e$ is the electron momentum and $\vec{v}_e$ is the electron velocity.

In the case of $v_e \ll c$ the equation could be approximated by $d\vec{p}/dt = -e\vec{E}$. The equation of motion can be expressed via vector potential $\vec{A}$ similarly as in [17]

$$\frac{d\vec{p}_e}{dt} + (\vec{v}_e \cdot \nabla)\vec{p} = e(\frac{d\vec{A}}{dt} - \vec{v}_e \times \nabla \times \vec{A}). \tag{1.12}$$

An important laser parameter is the normalized vector potential (averaged over 1 period)

$$a_0 = \frac{eA}{m_e c} = \frac{\lambda}{2\pi} \frac{eE}{m_e c^2}. \tag{1.13}$$

When $a_0 > 1$, the laser pulse is said to be relativistic.

Laser propagation inside the plasma

When a femtosecond laser pulse is incident on a gas target, the gas is typically partially ionized already by the rising edge of the main pulse. It follows that the main part of the laser interacts directly with the plasma. In the case of LWFA, the plasma could be assumed to be weakly-coupled and quasi-neutral before the laser arrival. The laser interacts mainly with plasma electrons while heavier ions are affected only marginally on the femtosecond time scale. For this reason, in the case of LWFA, the ions are usually considered to form an immobile background.

The Maxwell equations for electromagnetic waves traveling through a plasma are

$$\nabla \times \vec{E} = -\frac{\partial \vec{B}}{\partial t} \tag{1.14}$$

$$c^2 \nabla \times \vec{B} = \frac{\vec{j}}{\epsilon_0} + \frac{\partial \vec{E}}{\partial t}, \tag{1.15}$$

where $\vec{j}$ comes from electron motion:

$$\vec{j} = -n_0 e \vec{v}_e, \tag{1.16}$$

where n_0 is the plasma density.

From the linearized electron equation of motion 1.11 for $v_e \ll c$ and equations Eq. 1.14 and Eq. 1.15 the dispersion relation for electromagnetic waves propagating in plasma could be derived [18]:

$$\omega^2 = \omega_p^2 + c^2 k^2, \tag{1.17}$$

where ω_p is the plasma frequency, defined as

$$\omega_p = \sqrt{\frac{n_e e^2}{m_e \epsilon_0}}. \tag{1.18}$$

From this, it follows that inside the plasma the phase velocity

$$v_\phi = \frac{\omega}{k} = \sqrt{c^2 + \frac{\omega_p^2}{k^2}} \tag{1.19}$$

is greater than the speed of light. However, the group velocity

$$v_g = \frac{d\omega}{dk} = \frac{c^2}{v_\phi} \tag{1.20}$$

is lower than the speed of light.

From Eq. 1.17 it follows that when the plasma density (and thus ω_p) is raised, k will necessarily decrease. Finally, a density will be reached such that $k = 0$. This condition occurs at a critical density

$$n_c = \frac{m\epsilon_0\omega^2}{e^2}. \tag{1.21}$$

For densities greater than n_c, Eq. 1.17 cannot be satisfied for any real k, and the wave cannot pass through the plasma. From Eq. 1.17 k could be evaluated as imaginary [18]:

$$k = i\frac{|\omega_p^2 - \omega^2|^{1/2}}{c}. \tag{1.22}$$

And since the wave has a spatial dependance on $\exp(ikx)$, it will be exponentially attenuated at a skin depth δ:

$$e^{ikx} = e^{-|k|x} = e^{-x/\delta} \tag{1.23}$$

$$\delta = |k|^{-1} = \frac{c}{(\omega_p^2 - \omega^2)^{1/2}}. \tag{1.24}$$

Plasma waves and electron acceleration

A high-intensity laser propagating inside a plasma excites a longitudinal plasma wave. This is due to the nonlinear ponderomotive force, which pushes away electrons from areas with high electric fields. This force can be expressed (in linear limit $a^2 << 1$) as [19]:

$$\vec{F}_p = -m_e c^2 \nabla \frac{|\vec{a}|^2}{2}. \tag{1.25}$$

Plasma waves induced by an ultra-short laser pulse are called laser-induced plasma wakefields.

A plasma wave generated at the frequency ω_p in an initially uniform plasma is described by following equations [19] for the electron density perturbation δn:

$$\frac{\delta n}{n_0} = \frac{c^2}{\omega_p} \int_0^t \sin[\omega_p(t - t')]\nabla^2 \frac{|\vec{a}(\vec{r}, t')|^2}{2} \, dt \tag{1.26}$$

and the electric field of the wave

$$\frac{\vec{E}}{E_0} = -c \int_0^t \sin[\omega_p(t - t')]\nabla^2 \frac{|\vec{a}(\vec{r}, t')|^2}{2} \, dt. \tag{1.27}$$

6

The equations are valid for $E << E_0$, where $E_0 = m_e c \omega_p / e$ is the cold non-relativistic wave breaking field [20].

The maximum amplitude of a non-linear plasma wave can exceed the value E_0. Using the non-linear relativistic, cold fluid equations in one dimension, the maximum amplitude of a periodic plasma wave is expressed as [21]:

$$E_{WB} = \sqrt{2(\gamma_p - 1)} E_0. \tag{1.28}$$

This is called a cold relativistic wave-breaking field. γ_p is the relativistic Lorentz factor associated with the phase velocity of the plasma ($\gamma_p = (1 - v_p^2/c^2)^{-1/2}$). The plasma wave phase velocity v_p is equal to the group velocity of the laser [1]:

$$v_p = v_g^{EM} = c \sqrt{1 - \frac{\omega_p^2}{\omega_0^2}}. \tag{1.29}$$

If the plasma wave electric field amplitude approaches the value E_{WB}, then the Coulomb force is not able to keep electrons inside one period of the wave, and the wave breaks. Part of the electrons, which originally formed the wave, leaves the wave and are accelerated in the direction of the wave [22]. This outflow of the electrons simultaneously decreases the amplitude of the plasma wave.

1.2   LWFA acceleration regimes

The laser wakefield accelerator (LWFA) is a laser-plasma accelerator that is driven directly by the ponderomotive force of a single short ($c\tau \sim \lambda_p$) intense laser pulse. An advantage of using such short laser pulses to drive an accelerating wake is that they are immune to most laser-plasma instabilities. Additionally, these short intense laser pulses can drive wakefields with large amplitudes, that are capable of self-trapping and acceleration of electrons to high energies. In the following, details on a few specific regimes of LWFA are presented.

The wake induced by a short laser pulse is said to be in the **linear regime** if $\delta n/n_0 < 1$, where δn is the change in electron density associated with the wake. Such wakefields are excited by laser drivers with intensities $a_0 < 1$ and $P/P_c \leq 1$, where P_c is is the critical power for relativistic self-focusing in under dense plasma. In the linear regime, the electron density perturbation field and the longitudinal electric field of the wake vary according to sinusoidal function.

A **non-linear regime** is achieved when electron density perturbation of the wake is on the order of or greater than the background plasma density $\delta n/n_0$ and the longitudinal accelerating field of the wake becomes larger than E_0. These wakes are created by using laser drivers with $a_0 \gtrsim 2$. The longitudinal electric field profile of the non-linear wake has a saw-tooth shape - see Figure 1.2. A non-linear wake is said to be in the **1D non-linear regime** if the normalized laser pulse spot is broad, which means fulfilling the criterion $k_p w_0 \gg 1$. However, when $k_p w_0 \approx 1$ and $a_0 > 1$ the **3D non-linear regime** is approached.
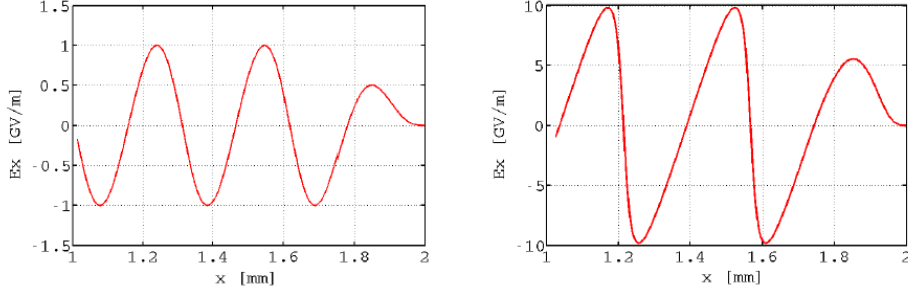
Figure 1.2: Typical shape of the electric field amplitude in a plasma wave in linear $a_0 = 0.5$ (left) and non-linear $a_0 = 2$ (right) regime. [23].

Another two cases can be distinguished in the 3D non-linear regime. The **bubble regime** describes a singular non-linear wake driven by laser pulse with $a_0 \geq 2\omega_0/\omega_p$. The **blowout regime** then describes a periodic non-linear wake driven by a laser pulse with $2 \leq a_0 \leq 2\omega_0/\omega_p$. In both the bubble and blowout regimes, the ponderomotive force of the laser pushes out all the electrons from within the first period of the wake creating an ion bubble into which background plasma electrons are self-injected, trapped, and accelerated.

In the blowout regime, there exists a matched self-guiding condition in which the intensity and spot size of the laser pulse are matched to the plasma density, such that the driven wake helps to avoid the diffraction of the laser pulse. This allows the wake to be sustained over tens of Rayleigh lengths and it can increase the length of the accelerating field of the wake. The matched self-guiding condition is valid when the laser fulfills $a_0 \gtrsim 2$ and $c\tau \sim \lambda_p/2$. When these conditions are met, the matching condition is given by [24]:

$$k_p w_0 \simeq k_p R_b = 2\sqrt{a_0}, \tag{1.30}$$

where R_b is the blowout radius of the spherically shaped wake. Even when the spot size is not precisely matched to the plasma density, the laser evolves within the plasma towards the matched spot size and pulse width via relativistic self-focusing and longitudinal pulse compression. This is called as **self-guided regime**.

1.3   Electron injection schemes

The development of the LWFA accelerators suffers from the shot-to-shot instability of the acceleration and low control over the electron beam features. These problems can be traced back to the injection of the electrons in the plasma wake driven by the laser pulse. Electron trapping is generally achieved by the wave breaking of the plasma wake (self-injection), a process that is by its nature uncontrollable and leads generally to poor-quality electron beams. Controlled injection techniques, such as injection by two colliding laser pulses [25], ionization injection [26], or density down ramp injection [27], have been developed to overcome these drawbacks. These methods offer improved electron beam parameters, but they typically require more complex setups.

The production of electron beams with low energy spread requires high control of the electron injection in the appropriate phase of the wakefield. Since the typical length of the wakefield plasma wave is on the order of $2\pi c/\omega_p \approx 10 - 100\ \mu m$, the length of the injection region has to be shorter than $2 - 20\ \mu m$ [22].

Electron self-injection

The simplest way how to inject the electrons into the right phase is the self-modulated injection, in which a single laser pulse results in self-trapping and generation of a sub-picosecond electron bunch, however, with a large energy spread. Typically the self-trapped bunch has a high charge (up to nC), with an energy distribution characterized by a Boltzmann distribution with a few MeV temperature (for 100 TW-class laser). One possible mechanism for self-trapping is via the generation of large-amplitude plasma wakefields, approaching the wave-breaking field. Since the phase velocity of the wakefield is very close to the speed of light, it is difficult to trap background plasma electrons, which are undergoing the fluid oscillation that sustains the wakefield. The wake will trap background electrons when the boundary of the wake overlaps the plasma electron orbits [19].

Electron injection by colliding laser pulses

This configuration uses one laser pulse to drive the wakefield and a second low-intensity counter-propagating pulse that generates a beat wave with the driver pulse. A good advantage of colliding pulse injection is that it provides extensive control over several electron beam parameters. By changing the delay between the two pulses the final electron energy can be varied as the injection point is shifted longitudinally and thus the effective acceleration distance changes. The strength of the injection pulse and relative polarization determines the phase-space volume of the injected particles and, thus, the bunch charge and energy spread [25]. The main drawback of this technique is the experimental complexity, due to the time synchronization and spatial overlapping of the two laser pulses inside the plasma.

Ionization injection

Injection of background plasma electrons could also be reached by laser-induced ionization. Injection of electrons is achieved by ionizing deeply bound electrons from a high atomic number (Z) gas at a proper phase inside the laser-driven wakefield, allowing them to be trapped in the right phase.

One way to realize it is by using two orthogonally directed laser pulses and a gas with high Z (eg. neon) [28]. A first laser pulse ionizes the gas to its mid-charge states to form a plasma and excites a large amplitude plasma wave. A second laser pulse with higher intensity and lower duration is then injected transversely, which further ionizes the medium to high-charge states producing another unbound electrons, which could be trapped in the plasma wave and accelerated to high energies.

A second approach uses a single laser pulse and a gas mixture (low Z gas with a small fraction of high Z gas) [26]. The rising edge of the laser ionizes the low Z gas and
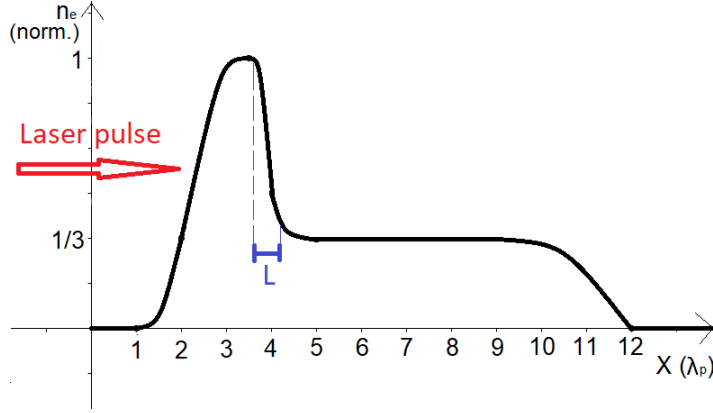
Figure 1.3: Plasma density profile suitable for density down-ramp electron injection. L is the length of the injection part of the profile, which should be lower than λ_p.

then the peak of the laser pulse ionizes the electrons from the high-charge states of the high Z gas. However, using a single mixed gas results in continuous injection over the laser-plasma interaction region, and this results in a large beam energy spread.

This technique could be improved by using a two-stage gas target to control the injection process [29]. In the first section, the electrons are injected by ionization injection in a high Z gas. The electrons then propagate in the second section, which is a field with a low Z gas, thus preventing the injection of additional electrons. This method produces electron bunches with lower energy spread.

Density down-ramp injection

In this case, the electron injection into the wakefield takes place in an electron density transition from high to low density. The injected bunch is then further accelerated in a low-density plasma. If the density transition is longer than the plasma wavelength, plasma electrons get trapped, because the local phase velocity of the plasma wave in the down ramp is slowed down until it equals the fluid velocity of the plasma electrons [22].

Injection via a sharp plasma density drop

A more sophisticated injection scheme is based on a sharp density drop between two adjacent regions of different densities (see Figure 1.3). The laser intensity and the plasma density have to be tuned to have a highly non-linear interaction without wave breaking in both regions. This allows for the generation of a stable but highly non-harmonic plasma wave, which, in turn, provides large accelerating gradients. During the downward density transition, the plasma wavelength λ_p increases steeply from its high-density value to the low-density one. This sudden increase in plasma wavelength causes the rephasing of a fraction of the plasma electrons into the accelerating phase of the plasma wave [30]. It follows that during the steep density transition, the plasma wave is fully loaded at once. Since the length of the transition has to be on the order of the plasma wavelength, this scheme requires complex gas target engineering.

10

Injection facilitated by nanoparticles

A novel injection scheme was proposed [31, 32] and a recent experiment demonstrated generation of up to 10 GeV electron beams [33]. The new electron acceleration scheme uses a nanoparticle to trigger the injection of electrons in the acceleration phase of a plasma wake. A nanoparticle is ionized by the edge of a laser pulse to create a strong electric field that attracts electrons from the plasma. The attracted electrons can gain additional momentum in the electric field of an ionized nanoparticle and are injected into the bubble. The theoretical studies predict that the characteristics of accelerated beams depend on the number of nanoparticles, nanoparticle composition, size, and position when the nanoparticle is injected into the bubble. The composition or size of the nanoparticle controls the number of electrons injected in the wake, and thus the charge of the accelerated bunch. The number of nanoparticles controls the number of electron bunches injected into the wake; thus controlling the bunch length, structure, and total charge. Injecting electrons at earlier or later times leads to accurate control of the electron beam energy by increasing the acceleration length and ensuring that injection can happen when the strength of the accelerating field of the wake is highest. Consequently, nanoparticle-assisted laser wakefield acceleration (NA LWFA) is a versatile scheme due to its high degree of control over the wakefield acceleration process.

The nanoparticle insertion method for LWFA looks similar to the cluster target [34], where nano-scaled solids are mixed with a background gas. However, the acceleration mechanism is entirely different. In the case of nanoparticles, the dominant mechanism for acceleration is direct acceleration. While in the case of clusters, the ionization injection takes place. Furthermore, a high gas pressure is required to form the clusters, thus the cluster method is not suitable for a low-density plasma. Since the nanoparticle insertion method is independent of the background density, it does not have any constraint on the gas density.

1.4 Theoretical demands on the gas targets (Scaling laws)

The successful design of an electron accelerator is mainly based on three components: laser driver, focusing optics, and target. The target is a device that creates an appropriate plasma density profile for the laser-plasma interaction. Since the injection and acceleration happen inside the target, the target design is crucial for reaching the desired accelerated electron beam parameters while employing the full potential of the laser driver. In this section, a theoretical framework for the design of the required plasma density profile, which should be created by a target, is given. The following formulas are derived from analytical calculations and/or Particle-In-Cell simulations.

Blowout regime

Lets assume we know the laser parameters λ_0 wavelength, P power, τ pulse duration and w_0 focal spot. The laser strength parameter a_0 is estimated as [19]

$$a_0 \approx 8.54 \cdot 10^{-10} \cdot \lambda[\mu m] \cdot \sqrt{I_0[W/cm^2]}, \tag{1.31}$$

where $I_0 = \frac{P}{\pi w_0^2}$ is the laser peak intensity in the focus.

First parameter, the plasma density in the target n_{pe} is derived from the matching condition 1.30 as

$$\omega_p = \frac{2c\sqrt{a_0}}{w_0} \tag{1.32}$$

$$n_{pe} = \frac{\omega_p^2 m_e \epsilon_0}{e^2}, \tag{1.33}$$

where ω_p is plasma electron frequency and we assume that $k_p = \omega_p/c$. This can be evaluated as:

$$n_{pe}[1/cm^3] \approx 1.13 \cdot 10^{20} \cdot \frac{a_0}{(w_0[\mu m])^2}. \tag{1.34}$$

The second parameter of the target is the length of the plasma density profile. The necessary target length is set by laser pump depletion and dephasing of the electrons [24]. The laser pulse etches back due to local pump depletion. The laser is depleted after a distance

$$L_{depletion} \approx \frac{\omega_0^2}{\omega_p^2} c\tau, \tag{1.35}$$

where $\omega_0 = 2\pi c/\lambda_0$ is angular frequency of the laser and c is the speed of light. The distance that the trapped electrons travel until they outran (dephase) the wave is

$$L_{dephasing} \approx \frac{2}{3}\frac{\omega_0^2}{\omega_p^2} w_0. \tag{1.36}$$

The desired acceleration length is the dephasing length, so the condition

$$L_{depletion} > L_{dephasing} => c\tau > \frac{2}{3}w_0 \tag{1.37}$$

is imposed. If the pulse is too short and the condition 1.37 is not met, the length of the target is set as $L_{depletion}$. In this case, the dephasing is not reached and the electron beam may have significant energy spread. If the condition 1.37 is met, the target length is set as slightly longer than the $L_{dephasing}$. The injected electrons need to slightly pass the dephasing point so that the energy spread is minimal. In this case, it should be kept in mind that the length of the pulse should not be too large because the laser field could interact with the trapped electrons and degrade the beam quality.

The electron energy gain depends on the average accelerating field of the beam-loaded wake E_{LW} and the acceleration length L_{acc} as

$$\Delta E = qE_{LW}L_{acc} \approx \frac{2}{3}mc^2\frac{\omega_0^2}{\omega_p^2}a_0, \tag{1.38}$$

Laser driver	L1 - Allegra	L3 - HAPLS
Wavelength [nm]	840	810
Pulse energy [J]	0.1	30
Pulse duration [fs]	15	30
Power [TW]	6.7	1000
Repetition rate [Hz]	1000	10
Focal spot (FWHM) [μm]	5	20.5
a_0 [1]	2.1	6
Target plasma density [$1/cm^3$]	$1.0 \cdot 10^{19}$	$1.8 \cdot 10^{18}$
Plasma wavelength [μm]	10.7	26
Depletion length [mm]	0.75	9.5
Dephasing length [mm]	0.55	14.6
Electron energy gain [MeV]	140	2600

Table 1.1: Top part: Design parameters of the two lasers dedicated to be used as laser drivers for electron acceleration at ELI-Beamlines. Bottom part: Evaluated scaling laws for LWFA in blow-out regime for the parameters of the above-mentioned lasers.

where the approximate evaluation applies for $L_{acc} = L_{dephasing}$. It can be also rewritten as

$$\Delta E[GeV] \approx 1.7 \left(\frac{P[TW]}{100} \right)^{1/3} \left(\frac{10^{18}}{n_{pe}[cm^{-3}]} \right)^{2/3} \left(\frac{0.8}{\lambda_0} \right)^{4/3}. \qquad (1.39)$$

The dependence of the electron beam energy is much stronger on the plasma density than on the power of the laser driver. However, when the plasma density is lowered for the fixed power, ensuring self-guided propagation of the leading edge of the laser is more challenging.

The scaling laws are evaluated for the parameters of two ELI-Beamlines lasers (L1-Allegra and L3-HAPLS) dedicated to be used as drivers for LWFA (see Table 1.1).

Sharp density drop injection

The most crucial parameter in the design of the density drop injection target is the density transition length δ_t, which has to be shorter than the plasma wavelength λ_p. The plasma wavelength can be calculated as

$$\lambda_p[\mu m] \approx 3.3 \cdot 10^{10} \cdot \frac{1}{\sqrt{n_{pe}[cm^{-3}]}}. \qquad (1.40)$$

Since the plasma wavelength in laser-plasma accelerators is usually of the order of μm, such short perturbation is achievable only by setting up a shock wave in the gas flow. From the kinetic theory[35] evolves that the shock thickness is of the order of molecular mean free path of the gas and it scales with the Mach number of the flow as

$$\delta_t = \frac{1}{2} \frac{\lambda_{MFP}}{M}, \qquad (1.41)$$

where λ_{MFP} is the molecular mean free path of given gas and M is Mach number of the gas flow. The molecular mean free path can be calculated as

$$\lambda_{MFP} = \frac{k_B T}{\sqrt{2}\pi d^2 p},$$

(1.42)

where k_B is the Boltzmann constant ($k_B = \approx 1.38 \cdot 10^{-23}$ J/K), T is the temperature of the gas, p is the pressure of the gas and d is the hard-shell diameter the gas molecules (usually around $3 \cdot 10^{-10}$ m). The values of M, T, and p in the supersonic nozzle flows can be well predicted by hydrodynamic simulations of the neutral gas flow - see Section 3.1.1.

Chapter 2

Technological aspects and limits of gas targets

Gas target plays an important role in laser-matter interaction experiments. It can provide gas with density widely ranging from 10^{16} to 10^{21} cm^{-3} and has the characteristics of adjustable gas density range and controllable gas length.

2.1 Gas target technology

Various technologies are used to produce the sub-critical plasma density profile required for stable and controlled laser electron acceleration. A gas target is a device that creates inside a vacuum chamber environment a structured gas density profile that is reachable by propagating a laser beam.

Formerly, to create a sub-critical plasma, exploding thin foils were used. The foils exploded after being irradiated by a laser pulse. The expanding plasma density profile has a parabolic shape. The main drawback of this solution was that the density profile shape was not easily tunable. Currently, the use of gas-based targets is preferred, because the density can be easily adjusted by changing the backing pressures. Nowadays, the widely used targets are gas nozzles exhausting into the vacuum. They can either be subsonic or supersonic. Other gas targets, that could be used for LWFA, are gas cells and discharge capillaries. These devices are based on trapping gas in closed volume.

Subsonic nozzles

A subsonic nozzle has a convergent or cylindrical inner body shape (see Figure 2.1(a)). The gas inside the nozzle propagates at subsonic speed (Mach number $Ma = u/\sqrt{\gamma \cdot R \cdot T} < 1$, where u, γ, R and T stands for absolute velocity, heat capacity ratio, specific gas constant and temperature respectively). The gas reaches $Ma = 1$ at the exit of the nozzle and then it propagates at supersonic speed inside the vacuum chamber.

Subsonic nozzles produce a parabolic density profile near the exhaust. Maximum density rapidly decreases with the distance from the exhaust [36]. For this reason, during LWFA experiments, it is necessary to focus the laser pulse very close to the
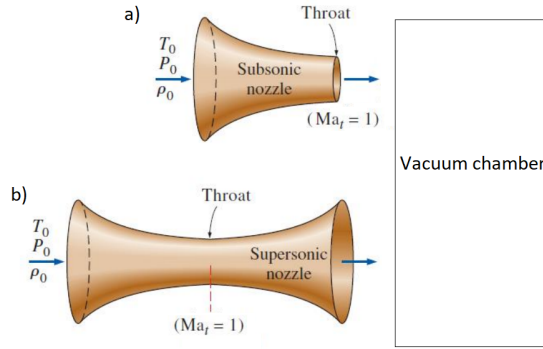
Figure 2.1: Shapes of (a) subsonic and (b) supersonic nozzles exiting into the vacuum chamber. The values T_0, P_0 and ρ_0 refer to the temperature, pressure, and density of the gas entering the nozzle inlet. Ma denotes the Mach number.
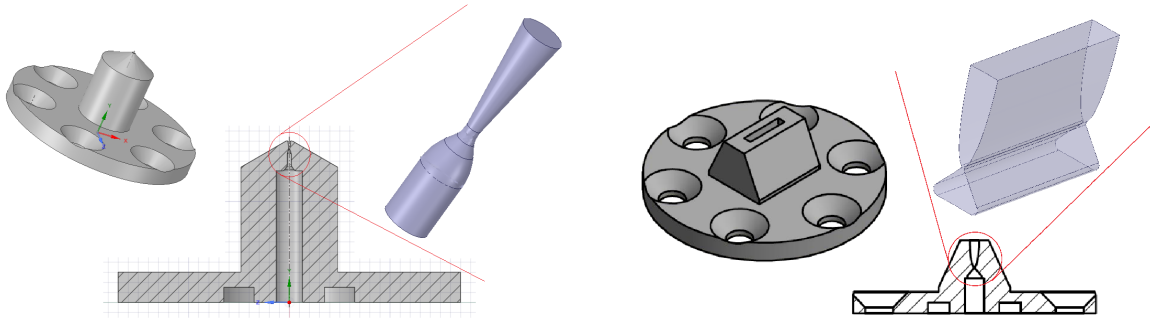

Figure 2.2: Models of axisymmetric (left) and slit (right) supersonic nozzles used for laser-plasma electron acceleration experiments.

exhaust. Subsonic gas nozzles can reach peak densities high enough to be used for LWFA driven by mJ laser [37].

Supersonic nozzles

Supersonic nozzles have a de Laval convergent-divergent body shape (see Figure 2.1(b)). The gas flow through the nozzle reaches supersonic velocity ($Ma > 1$) already inside the nozzle in the divergent part. Then shock waves, which occur in the nozzle, keep the gas jet compact for a long distance behind the nozzle exhaust. The supersonic nozzle can be designed in a way that the density profile is flat-top with steep gradients on the sides. Another important feature of the supersonic nozzles is that the density profile remains almost constant for a long distance above the exhaust (typically up to a few mm). This makes it easier to focus the high-intensity laser on the required density profile while keeping the laser focus far from the nozzle edge. The supersonic nozzles can be designed in various shapes and sizes. Axisymmetric and slit nozzle shapes are depicted in Figure 2.2.
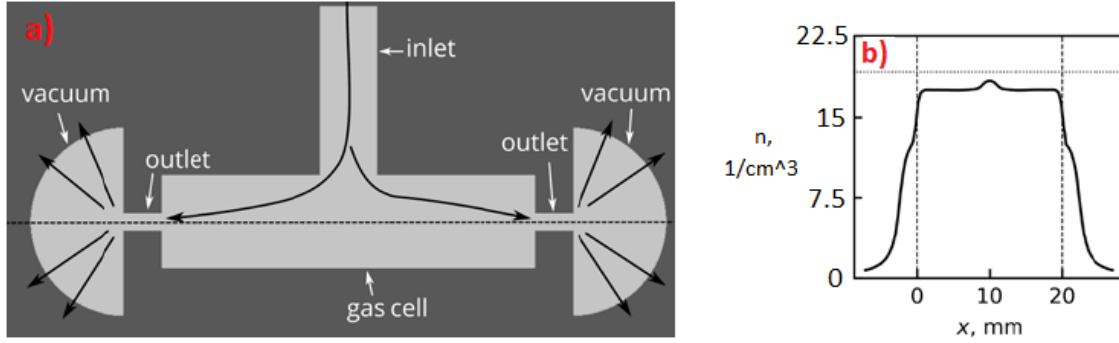
Figure 2.3: (a) 2D scheme of a gas cell. The gas cell body is axisymmetric (the axis is the dashed line). The arrows indicate the gas flow propagation inside the cell. The gas exhausts into the vacuum chamber. The laser enters and exits the gas cell by the two outlets. (b) Gas density profile of a single cell with a length of 20 mm, the diameter of the body of 5 mm, an inlet diameter of 3 mm, and an inlet pressure of 0.08 bar. The diameter of the outlets is 1 mm. Image taken from [38], adjusted.
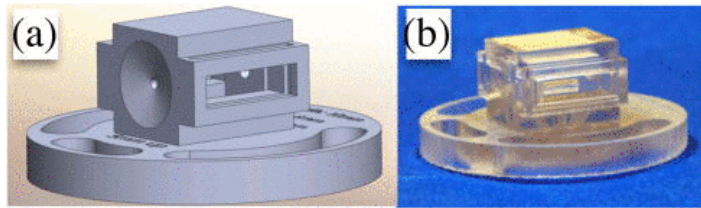

Figure 2.4: 3D printed gas cell used for laser plasma experiments [40]. (a) CAD model, (b) photography.

Gas cells

Gas cell consist of a closed volume filled with gas through an inlet. The gas exits the cell through two small outlets on its sides through which also the laser pulse can enter and exit the cell [38, 39]. Some of the gas inevitably leaks into the vacuum outside the cell through these outlets. Gas density is almost uniform inside the cell and decreases with a low gradient on the sides of the cell (see Figure 2.3).

The most important parameter of the gas cells is the ratio of the total cross-section of the outlets to the cross-section of the inlet. If this ratio is smaller than 1, the density profile is mostly uniform with just a small peak in correspondence of the inlet.

Discharge capillaries

Discharge capillaries consist of closed volumes filled by gas which is ionized by an electrical discharge before the laser pulse arrival. The discharge is generated by inducing a potential difference between the two ends of the capillary. The gas breaks down to form a plasma channel, which acts as a waveguide for the laser [41].

Discharge capillaries have different important features. The plasma channel is composed of fully ionized gas (usually hydrogen), thus the laser does not suffer from
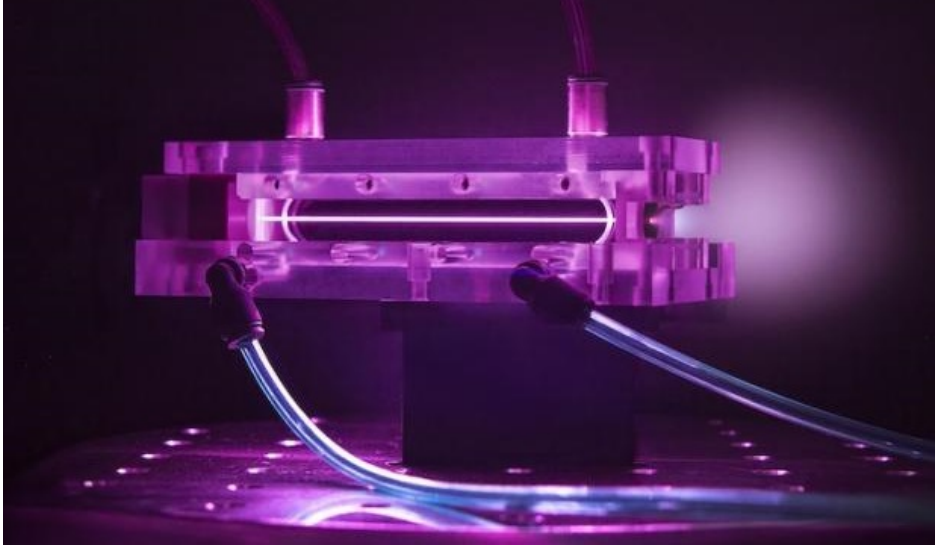
Figure 2.5: Photo of discharge capillary developed in Lawrence Berkeley National Laboratory and used for 8 GeV laser-plasma electron acceleration [5].

ionization-induced defocusing, or temporal and spectral distortion [42]. Discharge capillaries are scalable to lengths of hundreds of millimeters, limited only by the length over which the electrical breakdown can be achieved. Thereby they are opening a path to compact accelerators beyond the multi-GeV level for high-energy physics applications [43, 44, 5].

Gas jet tapering to create a steep down-ramp in the density profile

The density profile suitable for sharp-density drop injection can be achieved by various techniques. The first technique is the placement of a blade along the gas jet exhausting from a supersonic nozzle. The blade covers part of the gas flow and induces shock front in the supersonic flow - an easily controlled peak in the density profile. By changing the position of the blade over the gas flow, the parameters of the density peak can be tuned.

Another technique to create the down-ramp is to combine two nozzles [45], which generate a double-plateau density profile. In the overlapping region, close to the nozzle exhausts, the two gas jets do not interfere. By controlling the backing pressure of the two nozzles, the densities of the two plateaus can easily be optimized during experiments.

To obtain a density down-ramp also two gas cells connected by a tube can be used. In this case, it is also easy to control the densities in each cell independently. For this solution, the density gradient between the two stages is less steep than in the above-mentioned solutions.
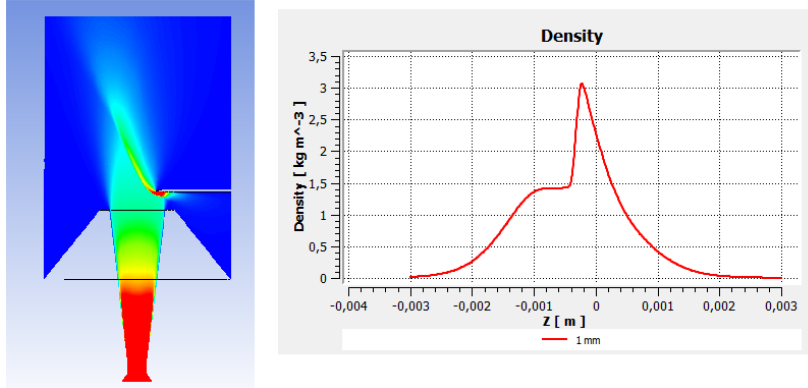
Figure 2.6: Axisymmetric supersonic nozzle gas jet tapered by a blade (left) and a gas density profile 1 mm above the blade (right).

2.2 Gas load into vacuum chamber

Laser wakefield acceleration is a well-established technology to produce up to multi-GeV electron beams in laboratories with a footprint smaller than 100x100 m^2. To get efficiently to the multi-GeV level and beyond, the PW-class lasers are used. This calls for different technological challenges that need to be investigated. As discussed in Section 1.4, the first parameter driving the PW acceleration is the gas target length. The desired length of the targets rapidly grows with the laser driver's power. The theory predicts that for > 10 GeV electron acceleration it will be necessary to implement > 1 meter-long targets. The trend of elongation of targets is evident from the review of performed laser-plasma electron acceleration experiments - see Figure 2.7.

Gas load into the vacuum chamber is one of the most important issues of the gas targets for experiments with laser power exceeding 1 PW. Therefore hydrodynamic simulations were performed to study the gas load of targets with different technology. The ultimate profile created by the targets was set to be 20 mm long with constant plasma density 6*10^{18}. The used gas in the targets is helium. All the targets are fulfilling the requirement that the axis of laser propagation is 0.5 mm far from the closest mass of the target.

A gas cell, subsonic slit nozzle, and three different supersonic slit nozzles were investigated to compare their density profile shapes and a volume of a gas exhausting from the target into the vacuum. The backing pressures were set at each target independently to receive equivalent plasma density in the targets. The resulting density profiles are depicted in Figure 2.8 and the calculated gas loads are stated in Table 2.1. It can be seen that all the slit nozzles have an almost equivalent gas load, while the gas load of the gas cell is more than 20 times smaller. It is not possible to pump out such high gas loads as $> 5 \; l/s$ even with powerful vacuum pumps and the high vacuum would not be sustainable while operating the nozzles in continuous flow. Only gas cells and pulsed nozzles are suitable to be used as a targets for GeV electron acceleration. The pulsed operation of targets deteriorates the shot-to-shot stability of the accelerator and prohibits the high repetition rate operation of the accelerator.
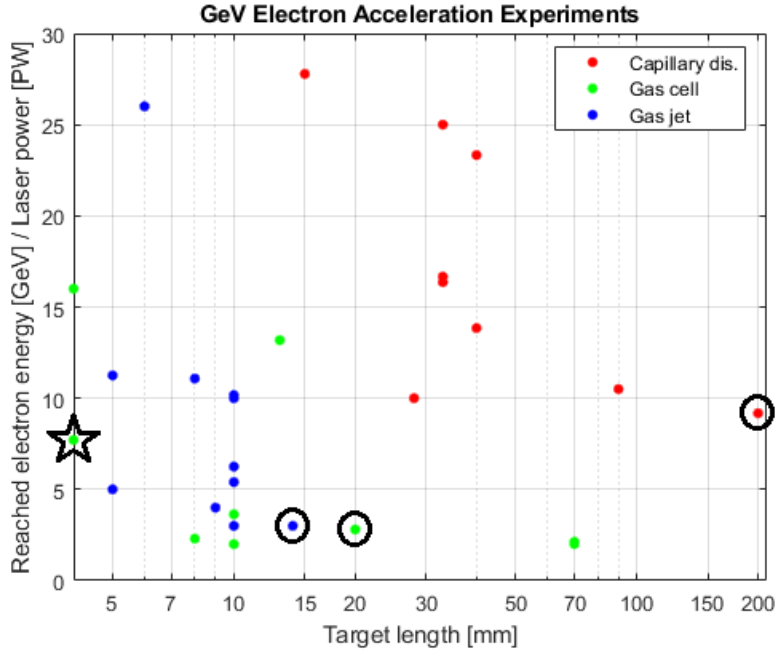
Figure 2.7: Review of experiments published during years 2004-2020 in which the peak electron energy exceeded 0.35 GeV. The plot shows the length and type of the gas target used in the experiment and the ratio of the reached electron energy in GeV units to the Laser power in PW units. Experiment with the highest electron energy for each category of targets marked by circles. The most stable experiment is marked by a star.

Geometry	Throat cross-section [mm²]	Backing pressure [bar]	Gas load [l/s]
longitudinal de Laval 1:6	4.00	5	9.52
transversal de Laval 1:6	4.08	5	9.74
fully de Laval 1:36	0.68	30	10.19
subsonic nozzle	24	0.83	8.96
gas cell	1.57	0.50	0.29

Table 2.1: Gas load values of five different targets producing equivalent target profile. The values are calculated by performing hydrodynamic simulations.

2.3 State-of-the-art of the gas target technology in LWFA experiments

In this section, the gas targets from the latest state-of-the-art LWFA experiments are presented.

The highest electron energy achieved

A. J. Gonsales et. al.[5] demonstrated the production of electron beams with quasi monoenergetic peaks up to 7.8 GeV with a charge of 5 pC and 6 GeV peaks with up to 62 pC charge. They achieved it using 31 J, 35 fs, 1Hz BELLA Ti:sapphire-based
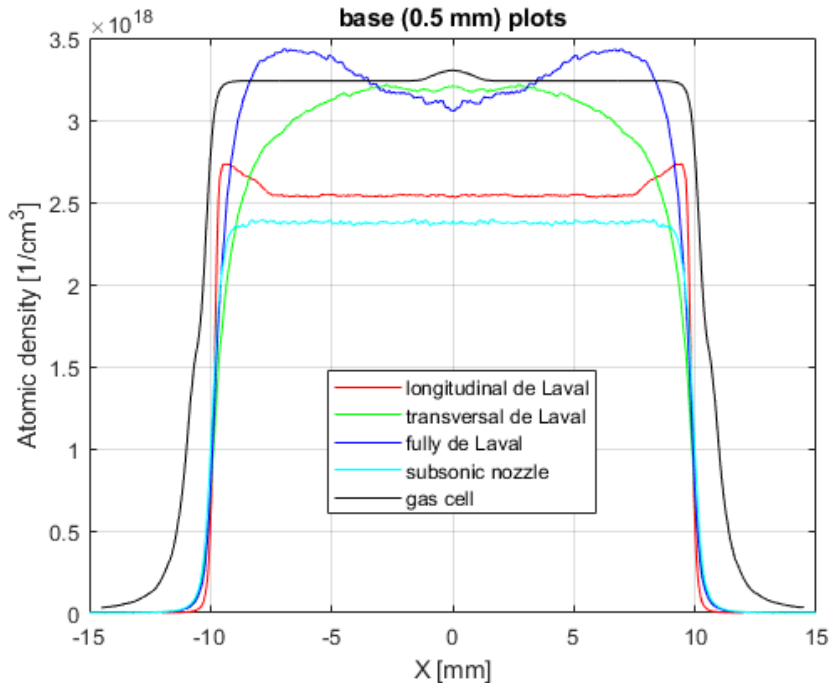
Figure 2.8: Target neutral gas density profiles produced by five different target technologies. The density profiles are calculated by performing 3D hydrodynamic simulations.

laser with 850 TW peak power. As a target, they used 800 μm diameter 200 mm long capillary discharge with current amplitude 450 A and rinse time 400 ns. The channel depth of the capillary discharge waveguide was increased using matched laser pulses of nanosecond length to locally heat the plasma along the capillary axis via the inverse bremsstrahlung mechanism. This structure extended the acceleration length to 20 cm at low electron density ($n_e \approx 3.0 \times 10^{17}$ cm^{-3}) and enabled to production of electron beams at such high energy. The scheme of the accelerator layout is presented in Figure 2.9.

C. Aniculaesei et. al.[33] present the production of electron beams with maximum energy 10 ± 1.86 GeV and 340 pC charge. They achieved it using The Texas Petawatt Laser which delivers 130 ± 10 J, 135 ± 10 fs pulses on target. In this case the 100 mm long gas cell[32] with 3-mm-diameter pinholes on sides filled with helium gas ($n_e \approx 6.0 \pm 0.5 \times 10^{17}$ cm^{-3}) was used. Nanoparticle-assisted electron injection was implemented by ablation of an aluminum plate situated on the bottom of the gas cell by an auxiliary laser pulse (130 mJ, 10 ns duration, 500 μs before the main pulse). The nanoparticles mixed with the helium gas filled the gas cell uniformly. The simplified setup of the experiment and the design of the gas cell are presented in Figure 2.10.

The most stable LWFA accelerator

The up-to-date most stable laser wakefield electron accelerator was built by Maier et. al.[8]. They were able to perform the first stable 24-hour operation of a laser-plasma
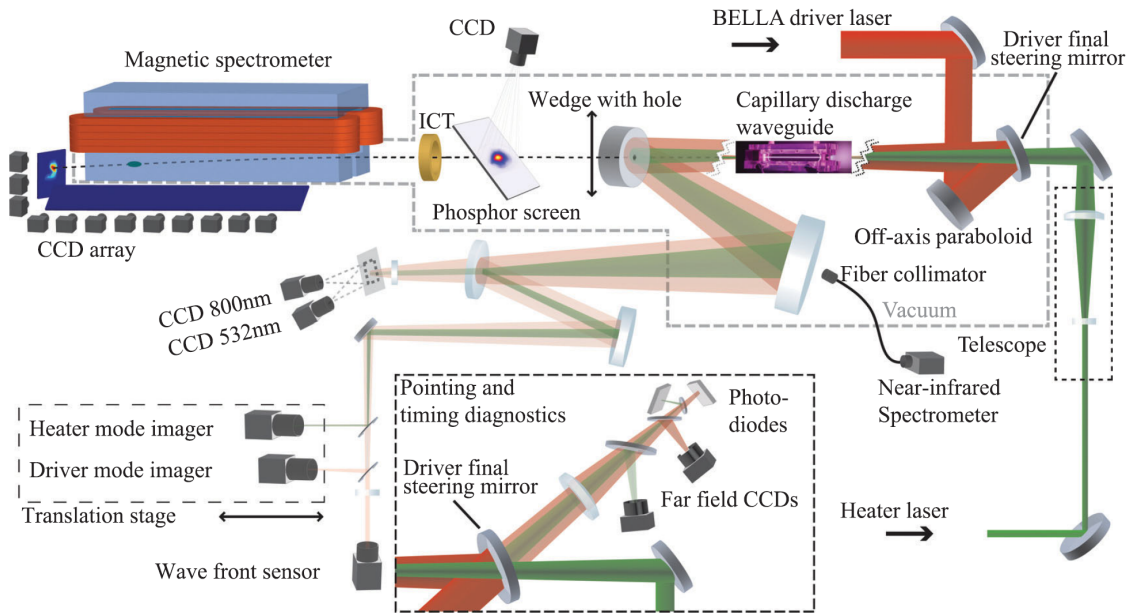
Figure 2.9: Schematic layout of the BELLA laser-plasma accelerator, including the heater laser system for enhancing the capillary discharge waveguide [5].
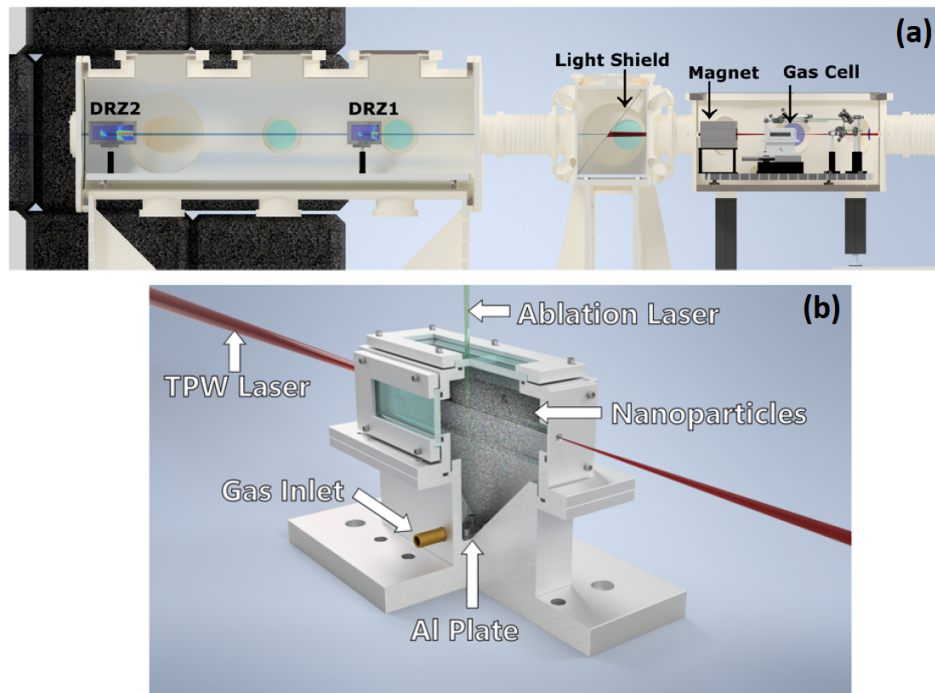

Figure 2.10: (a) Simplified scheme of the 10 GeV nanoparticle-assisted laser wakefield accelerator setup. DRZ1 and DRZ2 are scintillating screens for electron energy detection. (b) Model of the used gas cell target system[33].
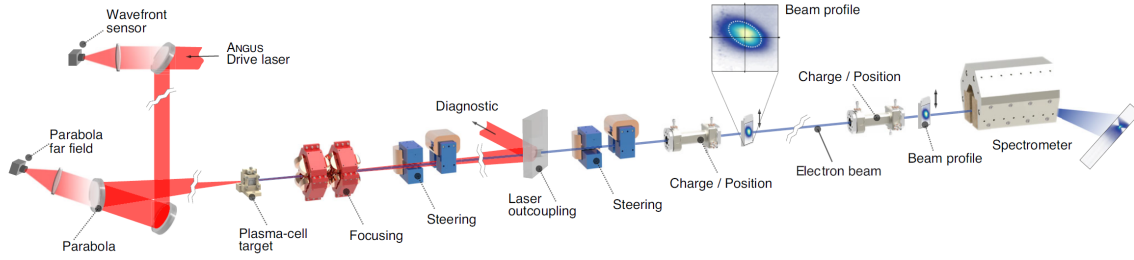
Figure 2.11: The experimental setup of stable laser wakefield accelerator producing 368 MeV electron beams[8].

accelerator with over 100,000 consecutive electron beam shots. The electron beams had, on average, a peak energy of 368 MeV ($\pm$ 2.4 % rms), a charge of 25 pC ($\pm$ 11 % rms), and an FWHM energy spread of 54 MeV ($\pm$ 15 MeV rms). The plasma accelerator is driven by ANGUS laser, a Ti:Sapphire-based system providing 2 J ($\pm$ 1.8 % rms) pulse energy on target at 42 fs FWHM pulse length to deliver 48 TW peak power at 1 Hz repetition rate. The accelerator setup is depicted in Figure 2.11.

The setup implements a gas cell target machined from sapphire crystal. A square (500 μm side length) channel is continuously filled with hydrogen from two independently mass-flow controlled inlets to support a 4-mm plasma density plateau of 2.7×10^{18} cm^{-3} electron density. The pressure, measured directly at the inlets, is 56 mbar. The first inlet was doped with nitrogen (up to 3% concentration) to inject electrons from ionization injection. An implemented differential pumping stage removes the gas load from the target chamber. The target supported more than 200,000 shots before replacement.

Acceleration at kHz repetition rate

F. Salehi et. al.[10] demonstrated laser wakefield acceleration of quasi monoenergetic electron bunches up to 15 MeV at 1 kHz repetition rate with 2.5 pC charge per bunch. The acceleration was driven by a 5 fs, 2.7mJ laser pulse generated by guiding and self-phase modulation of a 35 fs FWHM, 6mJ Ti:Sapphire laser pulse in a 2.5-meter long hollow core fiber filled with helium gas and chirped mirror compressor. See the experimental setup in Figure 2.12. The focused laser beam is used to drive electron acceleration from a near-critical-density hydrogen cryogenically-cooled gas jet target[46]. The jet producing a near-Gaussian gas density profile is created by a Mach 2.9 supersonic nozzle with 100 μm throat diameter.
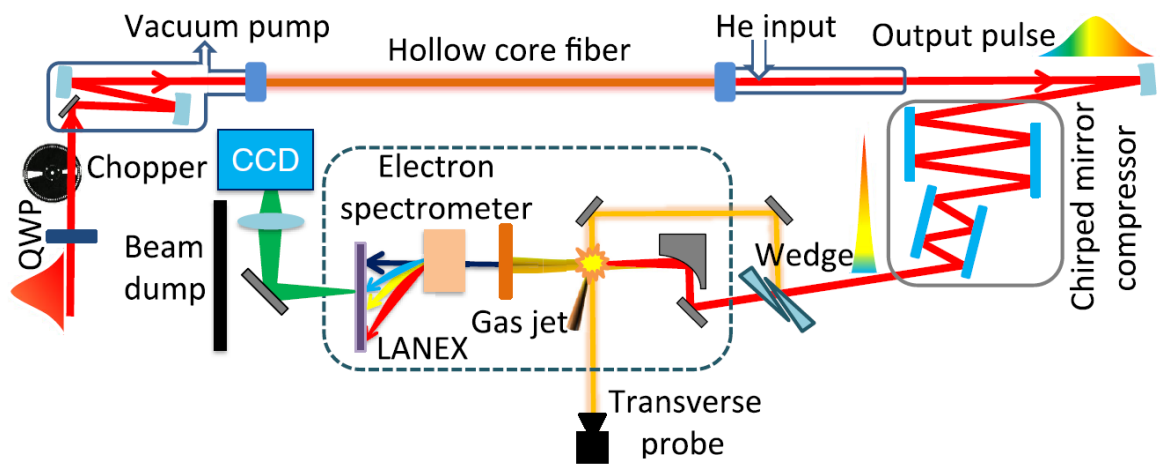
Figure 2.12: Experimental setup of the 15 MeV electron beams at kHz repetition rate. Laser pulses with a few-cycle duration, generated through a hollow core fiber and a chirped mirror compressor, are used to drive electron acceleration from a near-critical-density hydrogen jet target[10](adjusted).

Chapter 3

Methods for development of the gas targets

The quality and stability of LWFA output strongly depend on the density profile of the gas target, where the acceleration takes place [22, 47]. For this reason, the design and characterization of gas targets play a crucial role towards the realization of a stable high-quality laser wakefield accelerator. Gas targets can be designed using analytical models and numerical simulations [48, 49, 50]. Then, to benchmark the simulations and to experimentally characterize the real gas flow in the target, interferometric methods [51, 15] with post-processing by tomographic reconstruction [52, 53, 52] are typically used.

3.1 Computer simulation tools

Most of the targets used for LWFA in a self-guided regime consist of a subsonic or supersonic gas nozzle, gas cell, or combination of them. The geometry of such targets consists of a pressurized gas inlet, the shape of the target body in which the gas propagates, and gas outlet in the form of a large vacuum chamber surrounding the target. Based on the rarefaction of the flow, the gas flow dynamics in the target should be modeled by either the statistical mechanics or the continuum mechanics formulation. This is determined by the so-called Knudsen number Kn. Kn is a dimensionless number defined as the ratio of the molecular mean free path length λ_{MFP} to a representative length scale L

$$Kn = \frac{\lambda_{MFP}}{L}. \tag{3.1}$$

When the Knudsen number is small ($Kn < 0.01$), non-equilibrium effects are insignificant and the standard Navier-Stokes (N-S) equations can accurately predict the gas flow behavior. As Kn increases ($0.01 < Kn < 0.1$), regions of non-equilibrium begin to appear near surfaces as the molecule-surface interaction frequency is reduced - the most recognizable effect of this is velocity slip and temperature jump. The N-S equations can still be used effectively, but the slip and jump boundary conditions need to be implemented. However, once the Kn increases into the transition continuum ($0.1 < Kn < 10$) and free-molecular regimes ($Kn > 10$), the N-S equations cannot
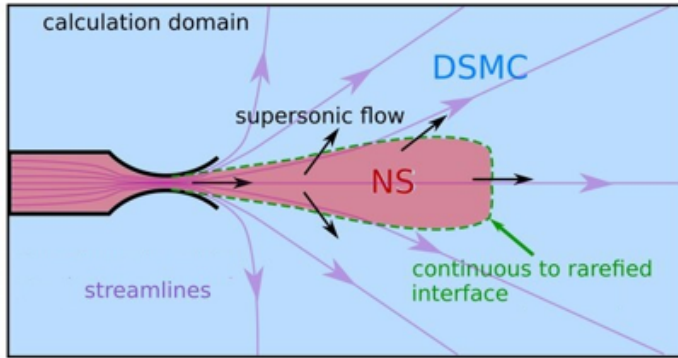
Figure 3.1: Illustration of the supersonic nozzle (black) exhausting into the vacuum chamber. When modeling such phenomena with hydrodynamic simulation, two calculation domains have to be distinguished. The first domain (marked by red color) consisting of the inlet, the inner part of the nozzle, and the region close to the nozzle outlet, fulfills the condition $Kn < 0.01$ and can be modeled by Navier-Stokes (NS) equations. The second domain (marked by blue color) is the rest of the vacuum chamber further from the nozzle exhaust. In this case, the continuum approach can not be used since $Kn > 0.01$ and the Direct Simulation Monte Carlo (DSMC) method has to be implemented. The position of the interface between the two domains is specific to given conditions.

predict the gas behavior. For these purposes, the Direct Simulation Monte Carlo (DSMC) method can be used.

3.1.1 Computational Fluid Dynamics (CFD)

The CFD approach, which solves Navier-Stokes equations, is sufficient for 2D and 3D steady-state simulations of gas flow through gas targets including a small part of the vacuum chamber close to the target exhaust - see Figure 3.1. Time-dependent simulation of propagation of the gas pulse initiated by a high-speed valve through the target geometry initialized with a high vacuum pressure is only partially feasible (with slip corrections and a very small time step). The accuracy is in this case very low and the convergence of the calculation is problematic. It is better to verify such calculations with a rarefied gas dynamics approach.

We use the following numerical setup for the steady-state target density profile calculation. The Navier-Stokes equations together with the equation of conservation of energy and the turbulence modeling partial differential equations are discretized with the Finite Volume Method. The two-equation eddy-viscosity turbulence model k-ω SST is used, as already described in the literature for similar cases [45]. This model combines k-ω and k-ϵ turbulence models such that the former is used near the boundary layer and the latter in the free shear flow. Hence the model is very robust. After discretization, the system of linear equations is solved iteratively by the Gauss-Seidel method.

The boundary and initial conditions are implemented as:

- The gas enters the simulation domain through the **inlet**, where a gas pressure and temperature are prescribed. A gas flow is not set at the inlet. The flow arises within the computation following the gas pressure difference in the inlet and outlet.

- The velocity of the gas at the **walls** is set to be zero and the walls are prescribed as adiabatic.

- The **outlet** boundary introduces the vacuum chamber conditions. At this boundary, the initial pressure is set to be the vacuum pressure however it is not fixed and it can vary during the calculation.

- All the values in the simulation domain are **initialized** with the values at the inlet (zero velocity, backing pressure).

Because the high vacuum cannot be well described with the equation of continuity, a higher pressure is used to model the vacuum part of the geometry. Even though in experiments the pressure in the vacuum chamber is around 10^{-6} $mbar$, the value 1 Pa is a sufficient approximation of the vacuum in the steady-state target simulations as demonstrated in [45].

Two codes are used for the CFD simulations. First is *Fluent* which is a part of the ANSYS commercial software package with the graphical user interface. The second is *OpenFOAM* which is freeware and is controlled by a text user interface.

ANSYS Fluent contains, except for the equation solver, the whole user interface for pre-processing and post-processing including SpaceClaim for the geometry setup, ANSYS Meshing for the mesh control, Fluent Setup for setting a boundary and initial conditions and numerical models, and finally CFD-Post for displaying and extracting the resulting data (see Figure 3.2).
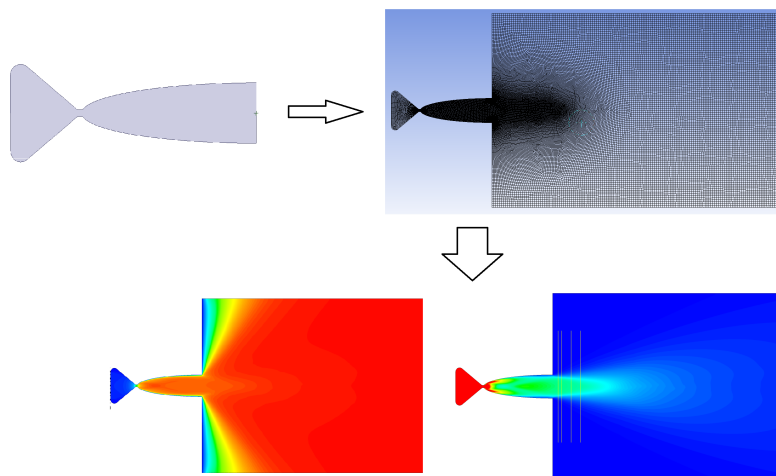

Figure 3.2: The process of setting up a CFD simulation. First, a geometry is designed. Then a mesh and boundary conditions are stated. Then the flow fields are calculated on the mesh grid. At the end, the post-processing calculations are performed.
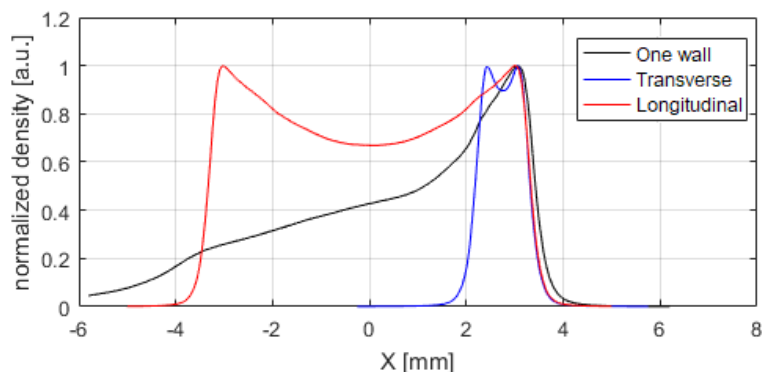
Figure 3.3: Comparison of the three normalized density profiles produced by the rectangular supersonic nozzle with removable walls. The density profiles are extracted at 0.5 mm above the nozzle, and the simulated gas is nitrogen. In LWFA experiments the laser propagates from the right to the left.

All the results presented in the study have been obtained by performing 2D-axisymmetric and 3D steady-state simulations, depending on the gas target geometry.

Characterization of supersonic and subsonic nozzles used as targets for LWFA experiments

Two different types of gas targets were characterized [54]. First, a supersonic rectangular de Laval nozzle designed and manufactured by Smartshell Co., Ltd., already successfully used in LWFA experiments [55], was studied. The nozzle has a 6.8 mm x 1.26 mm exit and removable side walls allowing to production of 3 different density profiles - see Fig. 3.3. The nozzle is designed to be used with high-power lasers ($\leq 10\ TW$) owing to the longer laser propagation.

To gain more flexibility in the experimental environment, density profiles obtained by placing a sharp obstacle (blade) along the supersonic gas path were studied. This study was performed along the transverse profile of the rectangular nozzle. The blade was positioned 3 mm above the nozzle and was 0.5 mm thick. The density profile is strongly affected by the longitudinal position of the blade. The peak-to-plateau density ratio versus the distance of the blade from the central line of the nozzle is plotted in Fig. 3.4.

Then a cylindrical subsonic nozzle - cylindrical capillary with 300 μm diameter, built in-house, was investigated in different schemes as a gas target to be used for LWFA driven by a few-mJ, kHz laser driver. The results indicate that, compared to the supersonic nozzles, the density of the gas jet from the subsonic nozzle rapidly decreases with the distance from the nozzle exhaust. The gas exits the subsonic nozzle with a larger opening angle than in the case of a supersonic nozzle. For this reason, in LWFA experiments, it is crucial to focus the laser as close as possible to the capillary exit.

To obtain a sharper density gradient, as in the previous case, a blade can be positioned along the gas path. Doubling of the gas density and much sharper gradients
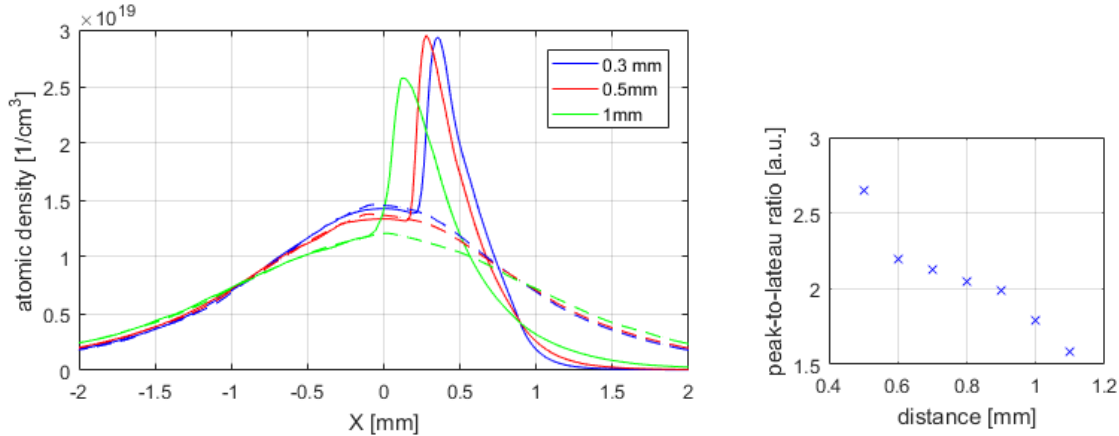
Figure 3.4: Left: Transverse density profiles with (solid line) and without (dashed line) tapering by a blade. The blade is placed 0.9 mm from the central line of the nozzle. The profiles are plotted at heights of 0.3 mm, 0.5 mm, and 1.0 mm above the blade. The gas used is helium at 30 bar backing pressure. Right: Peak-to-plateau ratio of the density peak induced by the blade vs. distance of the blade from the center of the nozzle.

were observed at this configuration. Illustrative results are shown in Fig. 3.5.

3.1.2 Direct Simulation Monte Carlo (DSMC)

The Direct Simulation Monte Carlo method is a particle-based numerical scheme for solving the non-linear Boltzmann equation [56, 57, 58]. Rather than exactly calculating successive collisions, as in Molecular Dynamics methods, the DSMC method generates collisions stochastically with scattering rates and post-collision velocity distributions determined from the kinetic theory of a dilute gas. While DSMC simulations are not correct at the length scale of an atomic diameter, they are accurate at scales smaller than a mean free path.

In DSMC simulation, the state of the system is given by the positions and velocities of particles, $\{\vec{r_i}, \vec{v_i}\}$. First, the particles are moved as if they did not interact, that is, their positions are updated to $\vec{r_i} + \vec{v_i}\Delta t$. Any particles that reach a boundary are processed according to the appropriate boundary condition. Second, after all particles have been moved, a given number of them are randomly selected for collisions. This splitting of the evolution between streaming and collisions is only accurate when the time step, Δt, is a fraction of the mean collision time for a particle.

Typically each particle in the simulation represents thousands of molecules in the physical system. In this sense, the DSMC method solves the Boltzmann equation using a representative random sample drawn from the actual velocity distribution. This rescaling allows us to model many systems of interest using only $10^4 - 10^6$ particles. However, if the number of particles in the simulation is too small, fewer than about 20 particles per cubic mean free path, the DSMC method is not accurate.

Collisions: To evaluate the collisions in the gas, the particles are sorted into cells
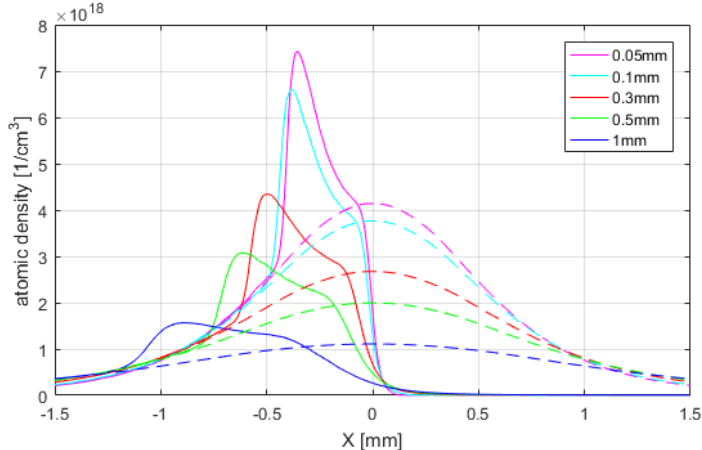
Figure 3.5: Capillary density profiles with (solid line) and without (dashed line) the blade at different heights above the blade. The blade is placed at a position of 0.05 mm from the center of the capillary and 0.5 mm above the capillary exhaust. The blade is 0.5 mm thick. The gas used is argon at 30 bar. Density profiles at 5 different heights above the blade (0.05 mm, 0.1 mm, 0.3 mm, 0.5 mm, and 1 mm) are plotted.

whose volumes are typically a fraction of a cubic mean free path. This spatial "coarse-graining" allows two particles to collide by simply being located within the same cell. At each time step, particles within a cell are randomly selected as collision partners. From kinetic theory, the collision probability for hard spheres is linearly proportional to their relative velocity. Conservation of momentum and energy provide four of the six equations needed to determine the post-collision velocities. The remaining two conditions are selected at random with the assumption that the direction of the post-collision relative velocity is uniformly distributed in the unit sphere.

Boundaries: DSMC simulations employ various types of boundaries (e.g., specular surfaces, thermal walls, fluxing reservoirs). When a particle strikes a specular surface its component of velocity normal to the surface is reversed. When a particle strikes a perfect thermal wall, all three components of velocity are reset according to the biased Maxwellian distribution. Finally, boundaries can act as fluxing reservoirs, that is, as infinite, equilibrium thermal baths at fixed temperature and density. At each time step, particles from the reservoirs flux into the system while particles already in the system can flux out. A flow velocity may be assigned to a reservoir to model inflow or outflow boundaries.

Statistics: Since DSMC is a stochastic method, most physical quantities of interest are computed as time averages. The values of mass density $\rho(\vec{r}, t)$, momentum density $\vec{p}(\vec{r}, t)$ and energy density $e(\vec{r}, t)$ are periodically measured as

$$\rho(\vec{r}, t) = \frac{1}{V_C} \sum_{i}^{Cell \ at \ \vec{r}} m \tag{3.2}$$

$$\vec{p}(\vec{r}, t) = \frac{1}{V_C} \sum_{i}^{Cell \ at \ \vec{r}} m\vec{v_i} \tag{3.3}$$

$$e(\vec{r}, t) = \frac{1}{V_C} \sum_{i}^{Cell \ at \ \vec{r}} \frac{1}{2} m |\vec{v}_i|^2, \tag{3.4}$$

where the sum is over particles in the statistics cell located at $\vec{r}$. The fluid velocity is computed as $\vec{u}(\vec{r}, t) = \vec{p}(\vec{r}, t)/\rho(\vec{r}, t)$. Temperature is computed from the equipartition theorem as

$$T(\vec{r}, t) = \frac{2m}{3k} \left(\frac{e(\vec{r}, t)}{\rho(\vec{r}, t)} - \frac{1}{2} |\vec{u}(\vec{r}, t)|^2 \right). \tag{3.5}$$

The local pressure $P(\vec{r}, t)$ is evaluated from the ideal gas low.

The DSMC simulation tool can be favorably used in the development of LWFA targets. It can be used for the simulation of gas flow through micro nozzles with dimensions $< 100 \ \mu m$. Another application is in time-dependent simulations of gas jet formation in a vacuum chamber. Last but not least, DSMC can capture the effect of species separation of light+heavy gas mixture in the jets produced by supersonic nozzle [59]. This is important for ionization injection where the mixtures of light and heavy gasses are used.

Two simulations are presented below. The first is benchmarking simulation. 2D simulation of supersonic nozzle with throat diameter $10 \ \mu m$ and exhaust diameter $30 \ \mu m$ exhausting into high vacuum was provided. The backing gas on the inlet is pure helium at 0.5 bar. Since the modeled instance is between the continuum and transition continuum regimes, both CFD and DSMC simulations were performed. The results agreed well. See the plot of axial neutral gas density in Figure 3.6.

The second simulation was performed to study the gas flow through the supersonic slit micro-nozzle and the effect of enrichment [60] of heavy gas in light carrier gas. The inner dimensions of the nozzle are $100 \ \mu m$ slit length, $30 \ \mu m$ exhaust width, and $10 \ \mu m$ throat width. The simulation was performed in 3D. The gas on the inlet is a mixture of Helium with 0.1 % of Xenon at a pressure of 0.5 bar.

The results of the second simulation are depicted in Figure 3.7, where the density map of helium and concentration of the heavy gas fraction are plotted in the plane perpendicular to the slit direction. A strong effect of concentration of the heavier gas in the central part is evident.

High-Performance Computing

The complex simulations (all kinds above mentioned) were performed either on Eclipse or Sunrise clusters in ELI-Beamlines. Eclipse is an 84-node cluster equipped with a shared central storage (1 Petabyte) and an Infiniband QDR interconnection network rated at 40 Gbps (gigabits per second). Each node contains 16 cores (Intel Xeon E5-2630v3 @ 2.4GHz) and 128 GB of available RAM DDR4 memory. Sunrise is a 324-node cluster equipped with a shared central storage (1 Petabyte) and an Infiniband HDR interconnection network. Each node contains 24 cores (Intel Xeon, class Cascade Lake) and 128 GB of available RAM DDR4 memory. Figure 3.8 plots the scheme of the Eclipse/Sunrise computational cluster architecture.
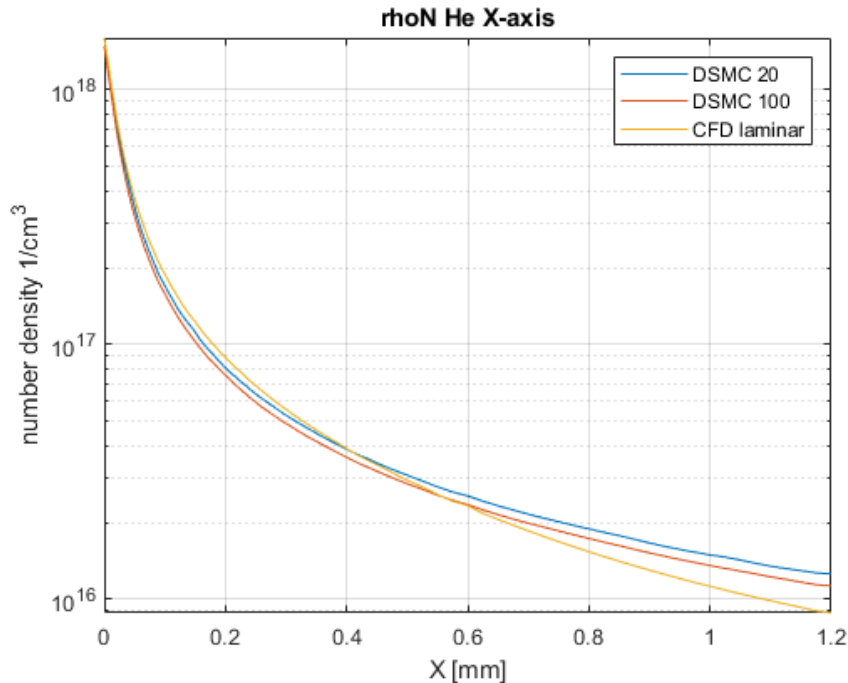
Figure 3.6: Atomic density of a neutral gas leaving 30 μm nozzle. The density is plotted on the axis of the nozzle. The X coordinate denotes the distance from the nozzle exit. The simulation tools used for the calculation are DSMC with approximately 20 macro-particles per computational cell (blue line), DSMC with approximately 100 macro-particles per computational cell (red line), and CFD for laminar flow (orange line).

3.2 Experimental characterization of the gas targets

The most popular method for assessing the density distribution of gas targets experimentally is interferometry. Lately, the research on interferometric techniques for neutral gas jet density characterization focuses on the improvement of interferometric sensitivity. Another trend is the use of tomography for the three-dimensional reconstruction of tailored gas density distributions. With advances in high-power laser technology, the characterization of LWFA targets becomes increasingly challenging, as either their density decreases (in the case of PW electron acceleration) or their dimensions are reduced (in the case of kHz repetition rate acceleration). Both trends decrease the phase shift of the probe beam, often reaching the sensitivity limits of the characterization method.

3.2.1 Interferometry

Optical interferometry is a family of probing techniques that utilize the interference between optical waves imprinted in the phase of the probing beam for precise
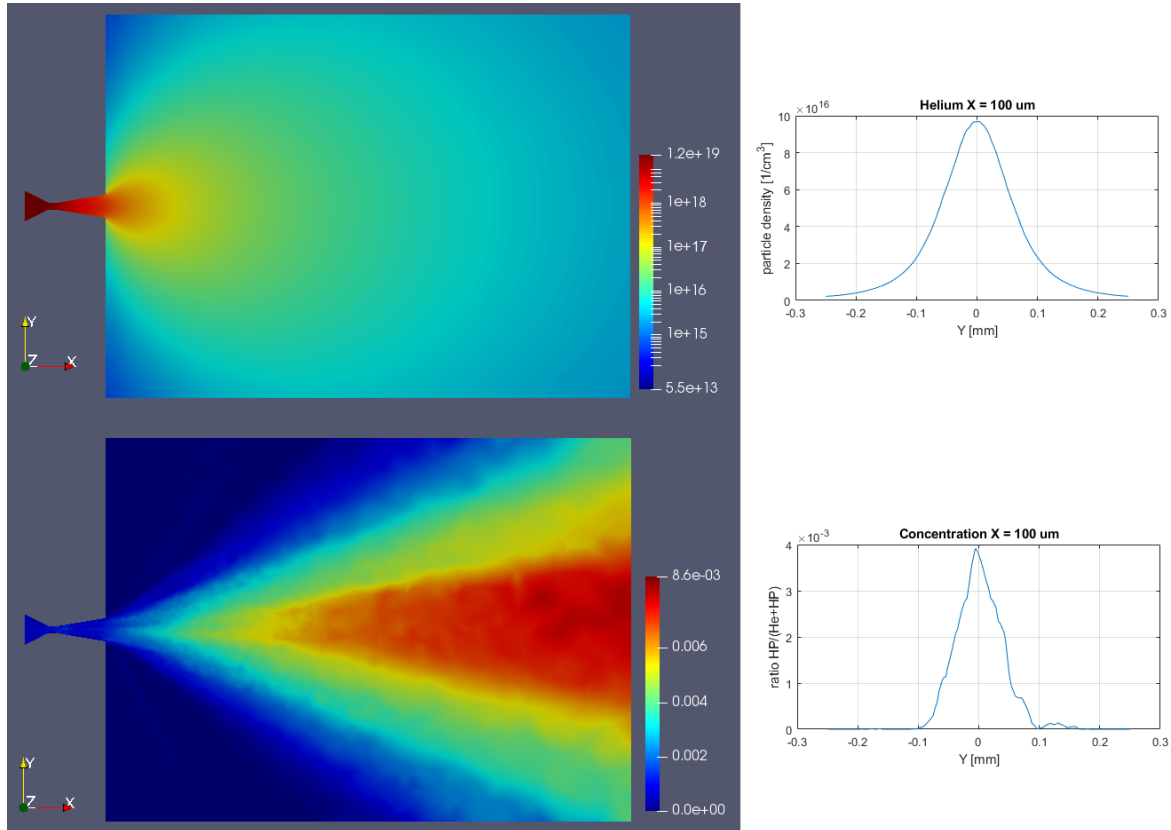
Figure 3.7: Results of DSMC simulation of slit micro nozzle fed by a mixture of 99.9 % helium and 0.1 % Xenon. Top: Atomic density map of helium gas in the plane perpendicular to the slit direction. Bottom: Concentration of xenon in the mixture. Right: Helium density and xenon concentration profiles 100 μm above the nozzle exhaust.
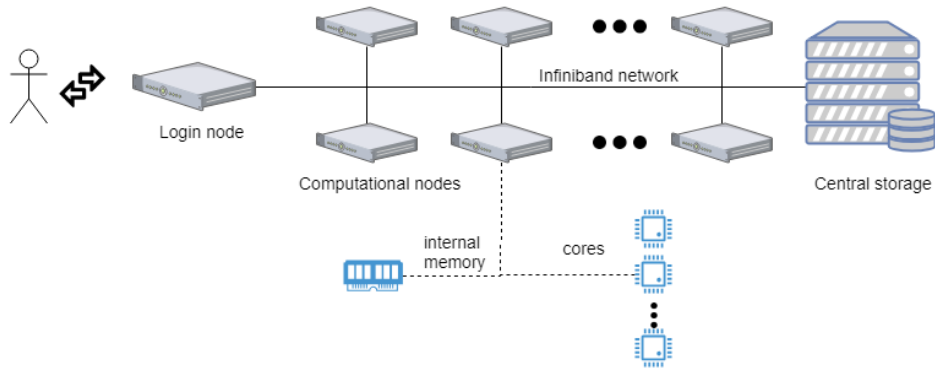
Figure 3.8: Diagram of the cluster architecture (Eclipse or Sunrise in ELI Beamlines). It shows an X-node cluster equipped with shared central storage and an Infiniband interconnection network. Each node contains computational cores and an internal memory. A user accesses the cluster via a Login node.

measurement of small distances, observation of refractive index variations, visualization of surface irregularities, determination of wavelengths, and many other characterization

methods. Science and industry foster an ever-growing demand for high-precision measurements. This is the driving force for improving the capabilities of existing optical probing methods and for the development of new interferometer designs.

For the characterization of the targets presented later, two types of interferometer are used: a basic Mach-Zehnder interferometer and a newly proposed [61] 4-pass interferometer with relay imaging arms.

Mach-Zehnder interferometer and interferogram evaluation

The Mach-Zehnder interferometer dominates in its simplicity of control and adjustments. The experimental setup is displayed schematically and a real photo is attached in Figure 3.9. The laser diode 405 nm continuous beam reaches the beam splitter, which divides it into two equal parts. Then one beam continues through the vacuum chamber with a gas target, which is mounted on a manually controlled rotational stage, and the other beam travels beside the nozzle (in air). Both beams are merged on a second beam splitter, and the resulting interferogram is captured on a CCD camera. The examples of the resulting interferograms are depicted in Figure 3.10.
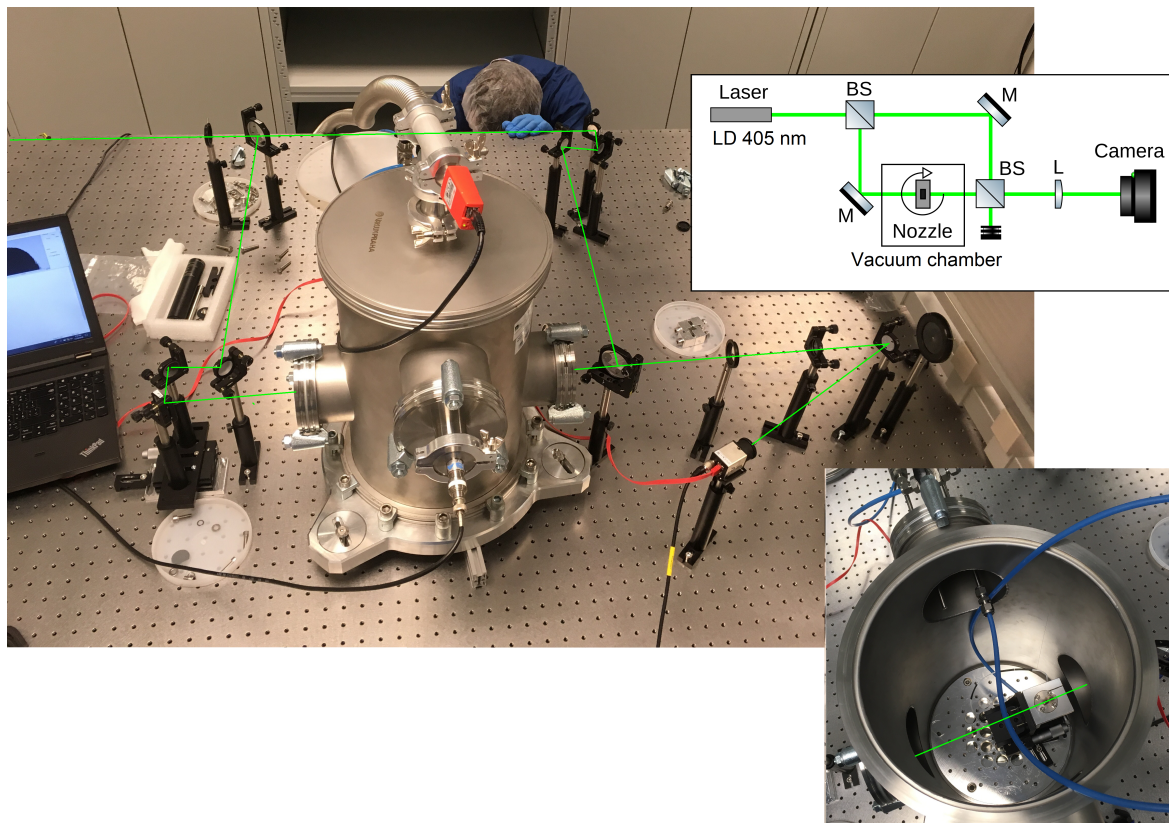

Figure 3.9: Photo of the Mach-Zehnder interferometer setup with sketched beam path and its diagram. The setup consists of a laser, two beam splitters (BS), mirrors (M), a lens (L), a camera, and a vacuum chamber with a nozzle. In the lower right corner, there is a top look inside the vacuum chamber.
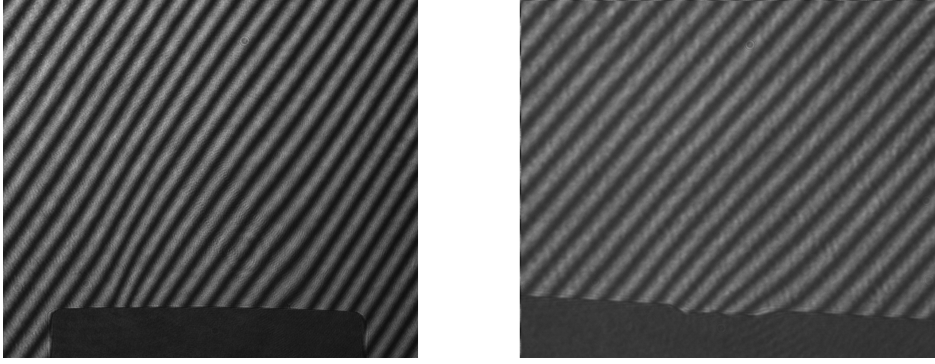
Figure 3.10: Example of the two interferograms obtained from Mach-Zehnder interferometer for the de Laval axisymmetric nozzle (left) and for the cylindrical nozzle tapered by blade (right).

It takes several steps to reconstruct the density profile of a gas target from one or more interferograms. All the steps are explained below.
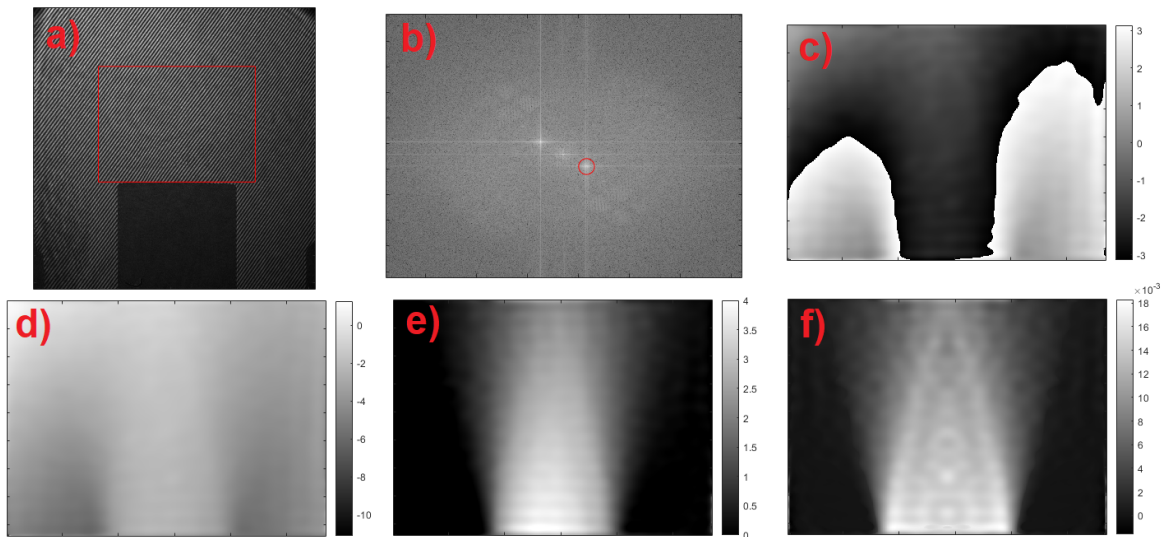
Figure 3.11: The process of an interferogram evaluation: (a) trimming of the interferogram, (b) filtering in the Fourier domain, (c) inverse Fourier transform, (d) unwrapping, (e) substituting the reference and (f) tomographic reconstruction. The processed interferogram comes from the measurement of the axisymmetric de Laval nozzle with Argon at 15 bar backing pressure.

1. **Loading and trimming:** The interferograms capturing the gas flow density profile and their references (interferograms capturing a background without the gas flow - They will be used later for suppressing the influence of the background on the density profile. They are processed in the same way as the main interferograms.) are loaded into matrices. Then the matrices are trimmed in a way that just a desired area remains (Figure 3.11a).

2. **Calculation of dimensions:** The size of a pixel d_{pixel} in the real space needs to be calculated. This can be done a priori in the experimental setup by using reference marks, or a posteriori by using the shadowgraph of the nozzle in the images.

3. **Enhancement of the second maximum in the Fourier domain:** The 2D Fourier transform is provided using the Fast Fourier Transform algorithm. Then the four quadrants of the resulting matrix are flipped to keep the zero frequency in the center of the matrix. If the absolute value (amplitude) of the transformed image is displayed, then there are 3 (or more) local maximums significantly visible. The direction in which the maximums lie is perpendicular to the direction of the fringes in the original image. The first maximum, which is in the center of the transformed profile, is not important for phase shift evaluation. The information about the phase shift is carried in the second maximum (due to the symmetry, there are two of them and they carry the same information).

   To evaluate the phase shift the second maximum has to be enhanced by a band-pass filter (Figure 3.11b). The band has the shape of a circle with a center in the second maximum (one of the two) and with a radius 1/3 of the distance between the first and the second maximum. Then, the second maximum is shifted into the center of the domain (instead of the first maximum) and the inverse Fourier transform is provided. The phase shift is obtained by calculating the phase angle from the obtained values.

4. **Unwrapping:** However, the resulting phase shift profile has limited values by interval $(-\pi; \pi]$ as the sin and cos functions are periodic with 2π. There are 2π jump discontinuities (Figure 3.11c), where the actual phase shift is cumulative. To obtain the real phase shift the resulting phase needs to be "unwrapped". This means that the occurred discontinuities are linked by adding an offset (Figure 3.11d). The unwrapping is done in both directions in the figure to ensure that no phase shift jumps are present.

5. **Phase shift range adjustment:** The reference profiles are substituted from the profiles carrying the information about the nozzle density profile (Figure 3.11e). This reduces background noise and effects caused by imperfect optical setup. Furthermore, the resulting profile is adjusted for positive values starting from zero. The area of the lower left and right corners is assumed to be a vacuum. So the value in this area is substituted from the rest of the profile to adjust the profile. Then, if any negative values occur, they are set to zero.

6. **Tomographic reconstruction:** The transformation from the projections to the 3D density profile is done by tomographic reconstruction algorithms (Figure 3.11f). In the case of the axisymmetric nozzles it is held by Abel inversion and in the case of more complex targets without cylindrical symmetry the advanced 3D tomographic reconstruction algorithms are used (see the Section 3.2.2).

7. **Density evaluation:** The final evaluation of the density comes from the following three equations.

36

First, the optical path length difference l_{OPLD} is computed

$$l_{OPLD} = \Delta\phi\frac{\lambda}{2\pi}, \tag{3.6}$$

where $\Delta\phi$ is the reconstructed phase shift and λ is the wavelength of the laser, which was used in the setup. Then the refractive index n is evaluated

$$n - 1 = \frac{l_{OPLD}}{d_{pixel}}, \tag{3.7}$$

where d_{pixel} is the dimension of space that covers one pixel. Last, the atomic density ρ is computed

$$\rho = \frac{n-1}{n_0 - 1}\rho_0, \tag{3.8}$$

where the n_0 is the refractive index of the gas exhausting from the target at standard conditions (temperature 273 K, pressure 10^5 Pa) and for the wavelength of the used laser. The ρ_0 denotes the atomic density (number of atoms of the given gas per cm^3) of the used gas at standard conditions.

Multi-pass interferometry with relay-imaging arms

The new concept of an interferometer is developed at ELI-Beamlines [61]. It consists of a multi-pass probing setup coupled to a shearing Wollaston interferometer. The unique feature of this setup is the capability to work with a different number of passes through the object (one, two, or four), using passive optical elements only, while preserving the spatial resolution. These capabilities are achieved by employing relay-imaging object arms and, in the case of four-pass probing, polarization switching of the probe beam. The increased number of passes allows more phase shifts to be accumulated, thus enabling phase sensitivity increase, while the high spatial resolution of the optical setup allows for precise tomographic measurements of complex phase objects.

The four-pass configuration employs polarization switching with two relay-imaging arms to facilitate four passes through the gas jet target (see Figure 3.12). In this configuration, the beam travels through the beam splitter and a polarizing beam splitter and illuminates the gas jet. The relay-imaging arm is used to enable a second pass and a quarter-wave plate is inserted in the collimated beam with a fast axis oriented under an angle of 45 deg concerning the incoming polarization to perform switching of the linear polarization (from horizontal to vertical). Because of the changed polarization, the beam is subsequently reflected by the polarizing beam splitter to the second relay-imaging arm of the setup and probes the jet for the third time before it enters the first relay-imaging arm again. This arm ensures the fourth interaction of the probe with the jet and switches the polarization back to horizontal. The horizontally polarized beam is then transmitted through the polarizing beam splitter and afterward, it is reflected by the non-polarizing beam splitter towards the phase measurement system.

In this configuration, the first and the fourth pass of the probe through the gas jet are performed with horizontally polarized light while the second and third
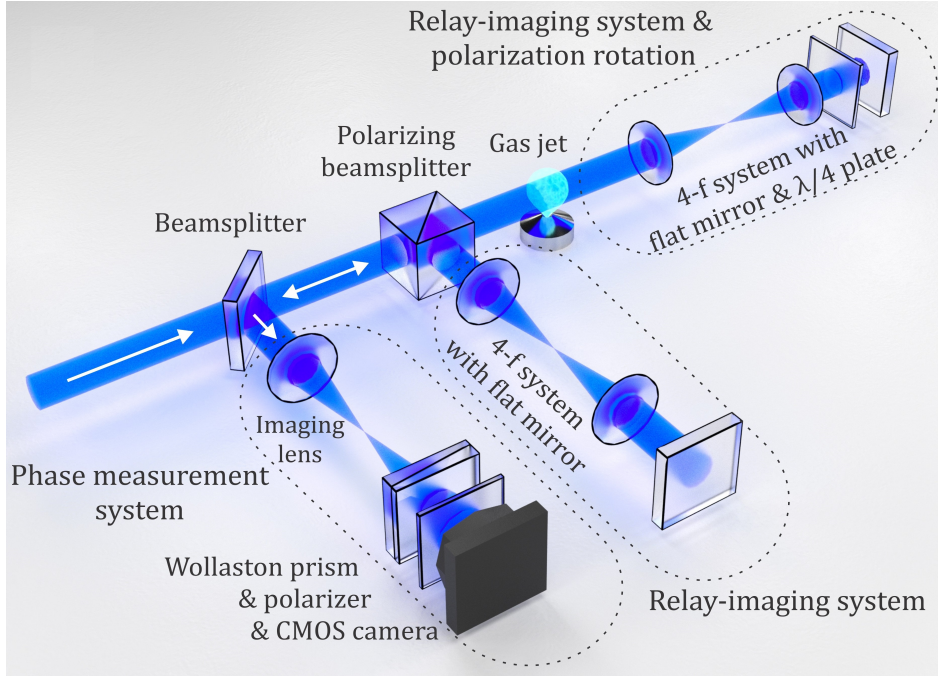
Figure 3.12: Schematic four-pass setup for interferometric gas target characterization. The first reflections of the beam on the beam splitters and their beam blocks are not shown. [61]

passes are with vertical polarization. This would be significant if the probed object was anisotropic, but it should not affect the characterization of gas jets, as those are considered optically isotropic and each of the passes contributes to the phase distortion of the probe equally. Moreover, the four-pass configuration can be easily switched to the double-pass one by rotating the quarter-wave plate by 45 degrees. This disables the polarization switching and eliminates the second relay-imaging arm.

3.2.2 Tomography algorithms

The measurement of structured density profiles by interferometry requires scanning the measured object from different angles and then computing the 3D profile by tomographic reconstruction starting from projections that carry only 2D information. Nowadays, different algorithms are used to characterize gas targets [62, 63, 52, 13, 53] and to our best knowledge no detailed comparison of their performances has been done. There is no clear indication about which of them is the most suited for a given specific density profile. This is the main motivation for the work [64], where different analytical and iterative reconstruction algorithms for LWFA gas targets are compared.

Algorithms for the 3D tomography

There are two main approaches to 3D tomography. The analytical methods solve the problem by utilizing the Fourier slice theorem [65], which relates the Radon transform and the Fourier transform. The investigated techniques are the Direct Fourier

Method (DFM) [66] and Filtered Back Projection (FBP) [67]. The iterative methods, instead, solve the problem in the real space by assigning to each pixel a weight factor depending on the contribution to projection rays. The resulting set of equations is then solved by an iterative technique called the Kaczmarz algorithm [68]. The methods investigated in the work are the Algebraic Reconstruction Technique (ART) [69], the Simultaneous Iterative Reconstruction Technique (SIRT) [70], the Multiplicative Algebraic Reconstruction Technique (MART) [71], and the Simultaneous Multiplicative Algebraic Reconstruction Technique (SMART) [72].

Both real and artificially created simplified density profiles have been used to test the algorithms, to get a deeper understanding of the specific features of each algorithm. The artificial test profiles have been chosen to isolate the main features that are typically present in LWFA gas targets, such as density down-ramps, sharp gradients, constant plateaus, and density drops surrounded by higher density. The realistic density profiles used for the algorithm testing are obtained by CFD simulations of gas targets successfully used in LWFA experiments. They refer to different types of typical LWFA gas targets such as subsonic nozzle tapered by a blade, and slit nozzle with open and closed side gas flow exits.

All the algorithms have been tested for different numbers of projections ranging from 2 to 36. The first projection is always in the direction of the X-axis and the others are shifted clockwise by multiples of the angle $180°/n_{proj}$, where n_{proj} is the appropriate number of projections. In the case of algebraic methods, the iterative process was initialized with a constant function $\forall j : f_j = 1$. This corresponds to a flat density profile in the whole reconstruction domain, but in principle, more accurate guesses could be used for density profile initialization. In practice, an expected mean value ρ of the density inside the jet can be used for the initialization ($\forall j : f_j = \rho$) or even better estimates.

Each tomographic reconstruction algorithm has been tested on all the test density profiles, and its performances have been analyzed in terms of the quality of the obtained reconstruction, its dependence on the number of projections, and computational time. The best-performing algorithms were found to be ART in the case of a low number of projections (<10) and FBP in the case of a high number of projections (>30). A more detailed analysis of the above-mentioned algorithms can be found in [64].

Newly proposed FARM algorithm

During the testing of the different analytic and algebraic algorithms, the new algorithm FARM (Filtered Algebraic Reconstruction Method) has been developed, which is a tomographic reconstruction algorithm tailored for LWFA gas target density profile reconstructions. FARM combines analytic and algebraic methods, and performs a filtering of the oscillations in the profile after the reconstruction. The new algorithm FARM is compared with the most performing algebraic and iterative algorithms [64].

The algorithm consists of three steps (see Figure 3.13). In the first step, FARM performs FBP reconstruction, then, it uses the resulting profile to initialize an ART reconstruction. In this way, FARM reduces the number of iterations needed for convergence and can improve the reconstruction of plateaus and drops in the profile. These

features make FARM an attractive method to be used in cases where the number of projections is limited to less than 30. After the convergence of the ART reconstruction, FARM applies non-linear filtering to remove the oscillations coming from the algebraic reconstruction algorithm.
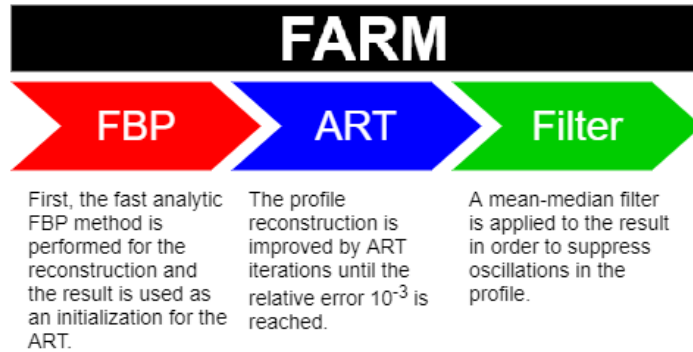

Figure 3.13: Diagram of the three steps of the new FARM algorithm.

To validate FARM, there has been provided a reconstruction test on the realistic density profiles obtained by CFD simulations of gas targets successfully used for LWFA. The performance of the algorithm was evaluated by mean and maximum errors of the reconstructed profiles, which describe, respectively, the reconstruction of the profile shape and sensitivity to artifacts occurring in the profile. In each test profile, FARM is outperforming ART. The only algorithm that gets better reconstructions than FARM is FBP, but only in the case of at least 30 projections. Moreover, FARM is about 30% faster in convergence than ART.

The algorithms have been tested also on real experimental data from the interferometric measurement of a rapid-expansion 6.8 mm long de Laval slit nozzle designed and manufactured by Smartshell Co., Ltd. with a sharp razor blade mounted transversely to the nozzle slit. The measurement setup consisted of a Mach-Zehnder interferometer with a laser diode (405 nm). After the phase unwrapping the size of the interferogram covered an area of 651×330 px, where each pixel corresponded to 13.2×13.2 μm^2 in the real space. The interferometric images were acquired from 36 different angles (from $0°$ to $175°$ on a $5°$ step basis).

The best reconstructions have been obtained with FARM (6 projections) and FBP (36 projections). The reconstructed 2D profiles by FARM and FBP for a different number of projections are shown in Figure 3.14. From the reconstruction, it turns out that the FBP algorithm suffers from artifacts even with a medium number of projections (6-18), while in the case of FARM, the artifacts are suppressed and it is possible to achieve a nice reconstruction already with 6 projections.

The ART algorithm produced also high-quality results but suffered from oscillations and needed two times more iterations (120) than FARM (54). The other algorithms produced unrealistic profiles (MART) or required a large number of iterations (SIRT(200), SMART(more than 1000)).
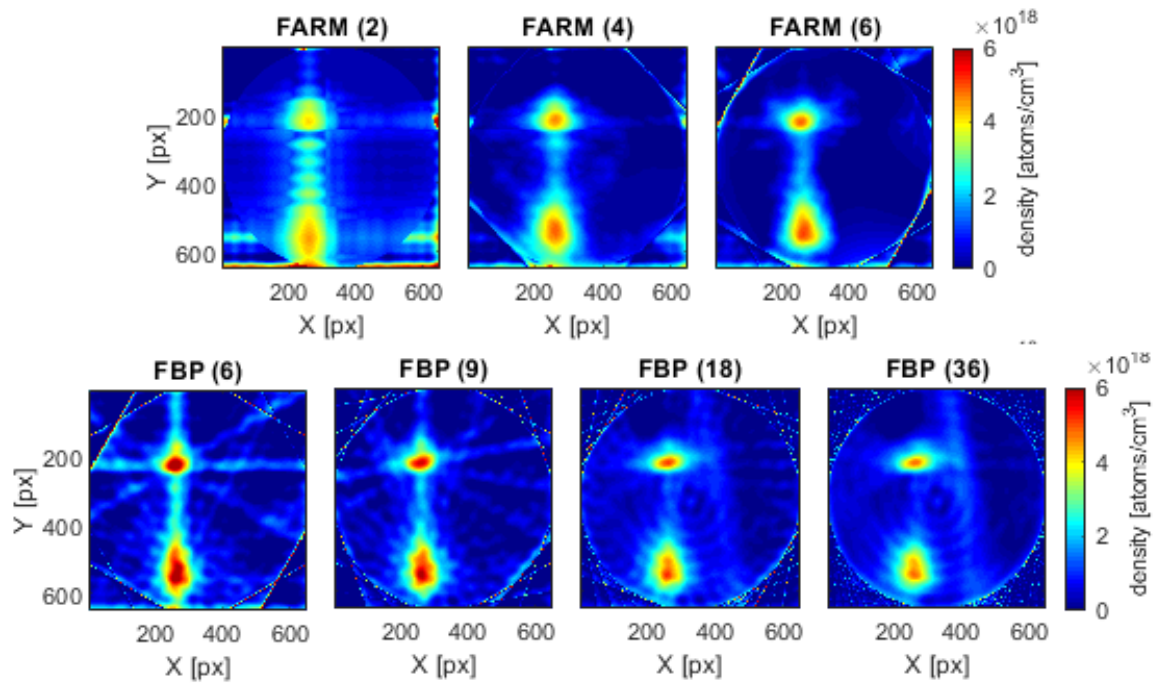
Figure 3.14: 2D density profiles reconstructed from measurement data by FARM and FBP algorithms for different numbers of projections (in brackets). The reconstruction refers to the plane 1 mm above the blade.

Chapter 4

Ultra-fast optical probe diagnostics in laser-plasma experiments

In laser-plasma experiments, a fraction of the driving laser pulse is typically used as an ultra-fast probe of the interaction process. This is advantageous due to the minimization of jitter between the two pulses. Successful implementation of this technique enables the observation of wake waves in a plasma behind the laser driver [73, 74, 75], injection dynamics [76, 77] and magnetic field structures [78] in electron acceleration process [79]. Besides LWFA, significantly interesting is also the optical probing of electron density singularities of a relativistic plasma capable of reflecting light via the double Doppler effect in the relativistic flying mirror mechanism [80, 81] or emitting bright coherent soft-X-ray radiation in the course of Burst Intensification by Singularity Emitting Radiation (BISER) [82, 83]. However, images of sharply localized relativistic singularities obtained by means of ultra-short probe pulses with duration τ are blurred to sizes $\sim c\tau$ due to the motion blur; here c is the speed of light. For 30-50 fs probe pulse duration, typical for high-power femtosecond lasers, this blurring reduces the spatial resolution to $\sim 10 - 15$ μm, which is often insufficient. The blurring effect can be reduced by compressing the probe pulse after the pick-off from the main pulse (post-compression) [84], which is a complicated technical task, taking into consideration that the femtosecond synchronization level should be retained.

4.1 Compression after Compressor Approach

Post-compression of the probe pulse is performed in two distinct steps: spectral broadening induced by time-dependent self-phase modulation (SPM) driven by the optical Kerr-effect [85, 86] followed by chirp compensation with the use of a set of chirped mirrors [87, 88, 89]. Two methods can be used for compression of the probe pulses: spectrum broadening achieved either in a gas-filled hollow fiber [90, 91] or in solid nonlinear medium (e.g. thin glass, crystal or plastic plates). The method implementing the solid nonlinear medium for SPM is called Compression after Compressor Approach (CafCA) [92, 93, 94]. Gases have very small nonlinearity coefficients, thus requiring intensely focused pulses propagating through long (tens of cm or even meters) fibers
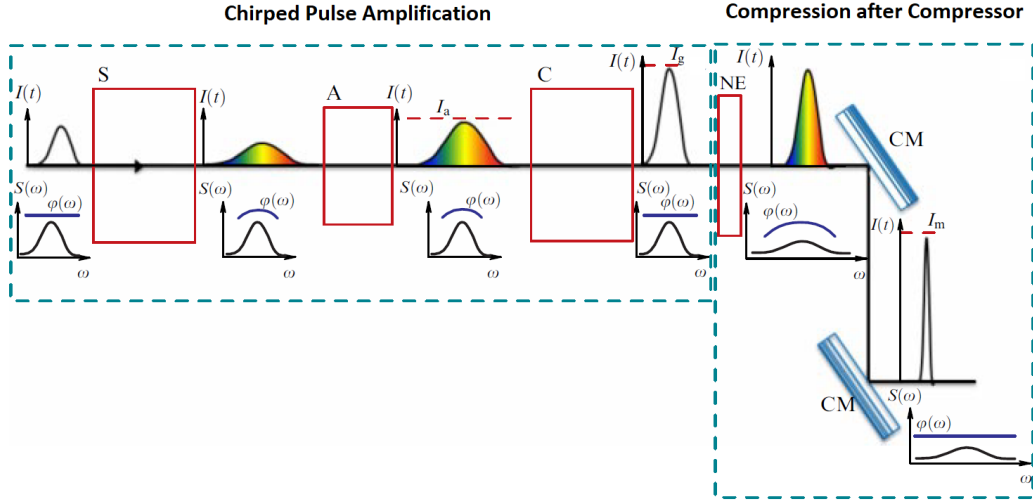
Figure 4.1: Chirped Pulse Amplification and Compression after Compressor Approach concepts. S-stretcher, A-laser amplifier, C-compressor, NE-nonlinear element, CM-chirped mirror, I_a, I_g and I_m are the breakdown thresholds of amplifiers, diffraction gratings, and chirped mirrors. Image taken from [93], adjusted.

to achieve significant SPM-induced spectral broadening. On the other hand, solid non-linear media of CafCA have much higher nonlinearities, thus operating at much lower intensities and with thin (millimeter-scale) plates. In both cases, the broad-bandwidth pulse after the SPM is compressed by negative-dispersion mirrors to durations several times shorter than the original laser pulse - see Figure 4.1.

4.2 Post-compressed probe beam setup challenges

Up to now most of the post-compressed probe experiments were performed using SPM in gas-filled hollow fibers, e.g. [76, 95]. However, this usually requires bringing the probe out of the main vacuum beamline, using a few-meter-long compression beamline including a gas-filled hollow fiber and long-focal-length lens or mirror, and bringing the compressed probe back into the interaction vacuum chamber [96]. In contrast, CafCA uses a shorter beamline and can be implemented in-vacuum, which significantly simplifies the setup and reduces the main-to-probe pulse jitter. Because of its compactness, the alignment is time effective and the whole CafCA setup can be built on an insertable stage, therefore the post-compression can be switched on/off online during an experiment. On the other hand, the following challenges arise during the high-power laser plasma experiments:

Reaching sufficient probe beam peak intensity for efficient SPM in thin plates: To minimize the temporal jitter between the main pulse and the probe, the latter has to be taken from the former either by wavefront splitting, or by the leakage of one reflective component, or by taking the edge of the main pulse with a pick-off mirror. These processes lead to probe beams with peak intensity significantly lower

than the main laser pulse so that SPM in thin plates becomes inefficient and cannot provide significant spectrum broadening. This can be overcome by focusing the probe pulse or its down-collimation before SPM, however, this is not a trivial task, taking into account the fact that the setup should be compact and the temporal and spatial beam qualities should be preserved to a high degree. Alternatively, the SPM can be increased by increasing the nonlinear medium thickness, but this induces greater material dispersion which is also positive and thus requires a larger number of bounces from negative dispersion mirrors, which complicates the in-vacuum setup.

Shot-to-shot peak intensity variations leading to compressed probe duration fluctuations: The near-field peak intensity distribution of high-power laser systems exhibits some variations, especially at the beam edges which are often used for probe pick-off mirror locations. Such variations will directly translate into the SPM variation and therefore to the compressed probe duration fluctuations.

Compressed probe duration dependence on the main pulse energy: It is typical for high-power laser experiments to scan the main pulse energy to study the dependences of various processes of interest on the laser power or intensity. The probe pulse, split from the main one near the interaction point, will have its peak intensity proportional to the main pulse energy. Thus, the SPM will be affected, and therefore the compressed probe duration as well.

Potential degradation of the probe pulse near-field pattern: SPM is a non-linear process and for large b-integrals can cause filamentation. Even not reaching this extreme case, the wavefront quality, and therefore after propagation of the near-field pattern, can be degraded. Further, the probe beam focusing or down-collimation discussed above can influence the near-field quality as well. These processes can affect the quality of the optical shadowgrams, interferometry, and Schlieren images.

Typically short experimental beam times of high-power user facilities: Policies of high-power laser facilities vary, but it is typical to grant from 1 to 6 weeks for a single experimental proposal. During this time, the team should build and optimize the entire setup (not only the probe line). This issue can be overcome by preparing the compressed probe line in advance as a part of the facility work, but this option is not always available.

Since we were not intentionally changing the pulse duration, and it was almost constant in all laser modes we used, we can assume that the beam fluence and pulse peak intensity are strongly correlated. I will be using both of these quantities in the following text.

4.3   Experiment with J-KAREN-P laser

The work [97] is aimed at shortening probe pulses using the CafCA approach [93] based on nonlinear spectrum broadening in optical plates followed by post-compression

of the pulse by chirped mirrors, and testing how the above issues affect real experiments. The setup for probing relativistic underdense plasma (1 mm diameter conical gas jet with electron density from $\sim 2 \times 10^{19}$ to $> 10^{20}$ cm^{-3} characteristic for BISER experiments) in the shadow and Schlieren modes has been used.

The experiment was carried out with the J-KAREN-P laser system [98, 99] at Kansai Institute for Photon Science in Japan as part of a standard 4-week beam time with an additional 4 weeks for setup. The experimental setup is shown in Figure 4.2. The probe beam was extracted by inserting a flat elliptical 45° incidence 1" pick-off mirror off to the side of the main laser beam ($\sim$11 inch diameter). The measured probe beam fluence was $\sim 1 - 10$ mJ/cm^2 (depending on the main pulse energy), and the time duration of the driver laser was 50 fs measured by Self-Referenced Spectral Interferometry [100] with a commercial Wizzler device (Wizzler I in Figure 4.2). To achieve efficient spectral broadening, the probe beam was down-collimated 10.7 times by an f = 750 mm achromatic doublet lens and an f = 70 mm singlet lens. Transmissive optics have been used to keep the original probe line path, which was necessary due to the limited delay stage range (a reflective down-collimation option would elongate delay beyond the available range, which would require complete rebuilding of the probe line). The configuration was an experimental trade-off between increasing the fluence of the probe pulse, and keeping its pointing stability to a level sufficient to maintain the spatial alignment with the main (driver) laser, which becomes increasingly sensitive as the down-collimation ratio increases. Nevertheless, the singlet lens was mounted on a three-axis motorized stage to adjust its position to a few μm levels to fine-tune its alignment. Without this motorization, the alignment shift of the probe beam due to target chamber pumping led to a complete loss of the probe image. A significant additional benefit from the down-collimation was increased probe pulse fluence which helped to see the probe despite the very bright plasma self-emission – it is necessary to note that in contrast to electron acceleration, the BISER experiments require relatively high plasma density of typically a few times 10^{19} cm^{-3} up to $> 10^{20} cm^{-3}$ and relatively high intensity ($> 10^{20}$ W/cm^2 after self-focusing) and high probe magnification, which make the plasma self-emission one of the most important experimental challenges.

The compactness of the CafCA setup allowed building the entire post-compressor on an insertable breadboard moved by a 300 mm in-vacuum translation stage, which allowed using the compressed or the original probe pulses, whereas the relatively small delay difference was compensated by a 300 mm delay line stage. When ultra-short broadband laser pulses propagate through transmissive optics, three main effects have to be taken into account: first, each wavelength propagates at a different speed inside the media, resulting in an increased group delay dispersion (GDD) of the laser pulse; second, owing to the difference between the phase and group velocity, the pulse front may be delayed with respect to the phase front [101, 102]; third, the transmissive optical element can be affected as the laser fluence approaches the damage threshold.

The GDD can be estimated by knowing the material-specific group velocity dispersion (GVD), the lens thickness, and the laser wavelength. The pulse front delay can be expressed by the following equation [102]:
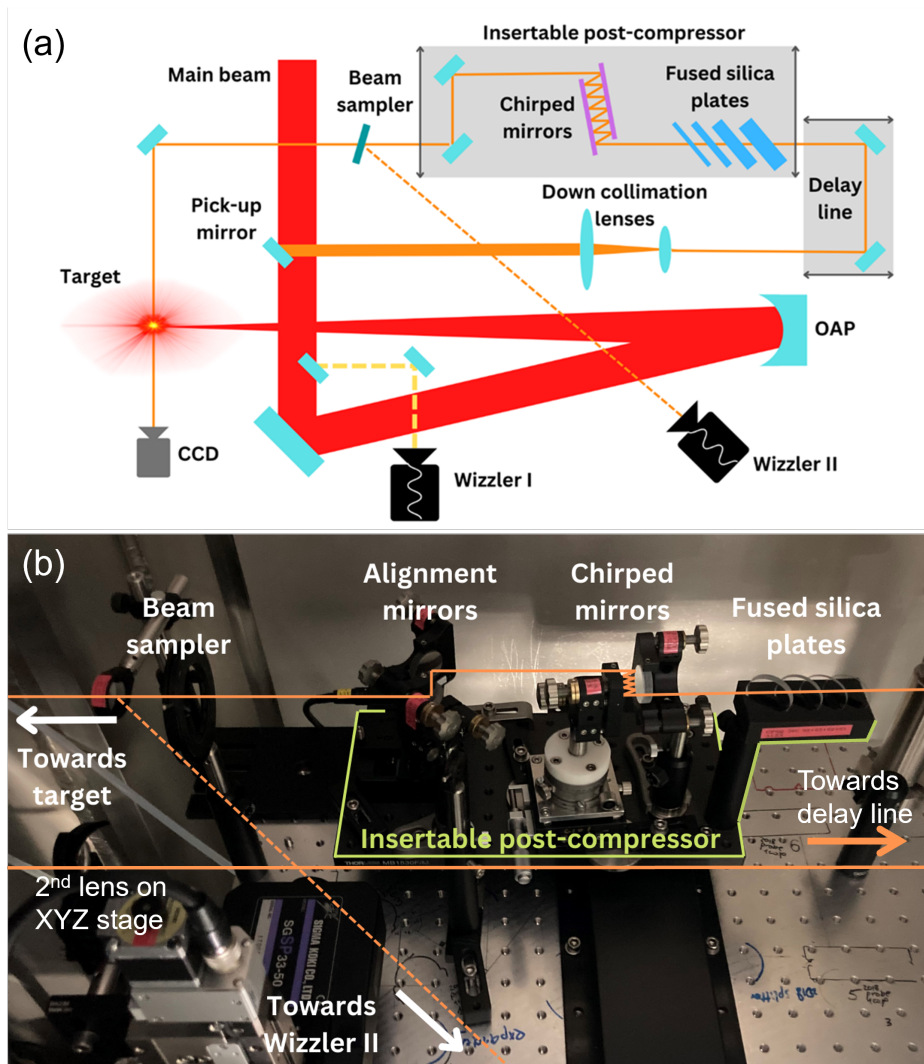
Figure 4.2: (a) Scheme of the compressed probe setup and (b) labeled image of the post-compressor station.

$$PTD = \frac{r^2}{2cf(n-1)} \left(-\lambda \frac{dn}{d\lambda} \right) \tag{4.1}$$

where r is the probe beam radius, λ is the laser wavelength, n is the refractive index of the lens material, and f is the focal length of the lens. It can be expressed also in typical experimental units as follows:

$$PTD\,[fs] \simeq 1.7 \times 10^3 \times \frac{r\,[mm]^2}{f\,[mm]} \times \frac{\lambda\,[\mu m]}{(n-1)} \times \left(-\frac{dn}{d\lambda}\,[\mu m^{-1}] \right) \tag{4.2}$$

The GDD can be compensated by negative-dispersion mirrors, while the PTD compensation is non-trivial.

By considering these three effects, the first lens of the down collimating system was chosen to be a 6.7 mm thick achromatic doublet, and the second lens was chosen as a 3.4 mm thick singlet lens. The first lens, being achromatic, did not add pulse front delay, but at the same time added 738 fs^2 GDD to the probe pulse. The second lens added a negligible 0.7 fs pulse front delay and 149 fs^2 GDD. The down-collimated probe beam spatial profile measured after the down-collimation before the fused silica plates are plotted in Figure 4.32(d). The spatial profile was measured by using a low-power alignment beam and insertable CMOS camera.

After propagating through the two lenses, the laser pulse achieved a fluence of $\sim 100-1000\ mJ/cm^2$ (depending on the pulse energy), which was sufficient to drive the nonlinear processes required to achieve spectral broadening within a few mm of fused silica (FS) [94]. After propagating through a sequence of 1, 2, 3, and 5 mm thick, plane-parallel FS plates set at Brewster's angle, the laser pulse was compressed by broad-band dispersive mirrors (chirped mirrors) with a nominal GDD of -40 fs^2 and incidence angle of 5°. (model PC5 from Ultrafast Innovations). This post-compressed pulse was used for the plasma probing, while its small fraction was split with an ultrafast beam sampler and sent to the second Wizzler device (Wizzler II in Figure 4.2) for simultaneous pulse shape measurement. An identical beam sampler was used in transmission in front of Wizzler II for the compensation of the main beam sampler effect on the probe. The Wizzler II results were post-processed to subtract the dispersion of the 2 mm thick CaF2 window and air.

4.4 Results

Figure 4.3(a,b,c) shows measurements in the Power Amplifier (PA) mode at 10 Hz carried out before the main experiment. The main pulse had the Full Width at Half Maximum (FWHM) duration $\tau_{FWHM} = 48.6\pm0.8$ fs (transform limit $\tau_{TL} = 48.0$ fs) and effective width $\tau_{Eff} = 52.0 \pm 1.6$ fs, while the compressed probe had $\tau_{FWHM} = 36 \pm 3$ fs ($\tau_{TL} = 31$ fs) and $\tau_{Eff} = 42 \pm 3$ fs. Here the effective width is the area under the normalized power curve: $\tau_{Eff} = \int p(t)\,dt$, where $p(t) = P(t)/P_{max}$ [98].

Figure 4.4 shows measurements of the main and compressed probe pulses during the experiment in several laser modes, i.e. Power Amplifier (PA) with $\sim$ 15 TW on target, Booster Amplifiers 1 and 2 (BA1 and BA2) with up to 100 TW. The main
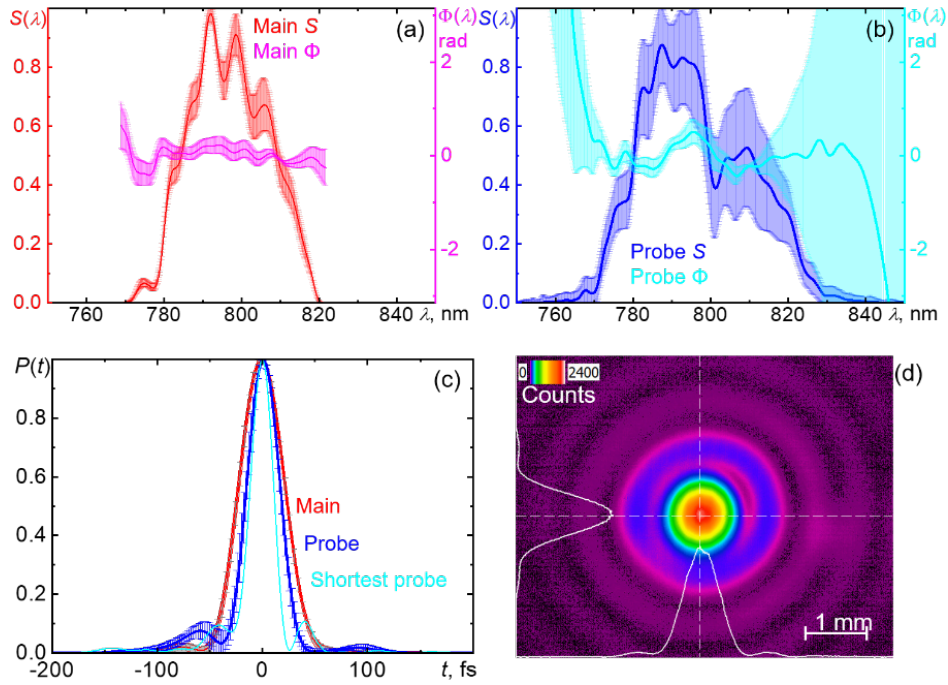
Figure 4.3: Main and probe pulses before the experiment. (a, b, c) Power Amplifier (PA) mode, $\sim$ 1000-shot average for the main and probe pulses, the error bars are standard deviations of shot-to-shot variations. (a) Red is the main pulse spectra, magenta is the main pulse spectral phase. (b) Blue is the probe pulse spectra, cyan is the probe pulse spectral phase. (c) Red and blue, are the main and probe pulse shapes, and cyan: is the shortest probe pulse. (d) Down-collimated probe beam spatial profile was measured before the fused silica plates by using a low-power alignment beam.

pulse duration remained nearly the same in all the laser modes. On the other hand, the probe's SPM gradually increased with the laser energy, while the negative dispersion provided by the chirped mirrors remained constant. In this configuration, the probe pulse compression was achieved in the majority of the laser shots. On the other hand, the stability of the compressed probe pulse duration was not as high as the initial pulse. We attribute this to the pulse-to-pulse fluence variation at the edge of the main beam, where the pick-off mirror was placed. In the setup (14 reflections from the chirped mirrors), the optimum compression and the highest stability were achieved in the BA1x2 mode, but the minimum probe duration was $\sim 18 - 20$ fs in all laser modes with the main pulse energy larger than 1 J. In the PA and BA1x3 modes, the average probe duration was somewhat larger. At higher energies (BA2x1, BA2x2 modes), the compressed probe had an even larger average duration and lower stability. The compressed probe was longer than its transform limit due to the remaining chirp and higher-order phase terms, especially in the higher-energy modes. In the optimum BA1x2 mode, we obtained $\tau_{FWHM} = 24 \pm 5$ fs (without outliers, $\tau_{FWHM} = 23 \pm 2$ fs) with the transform limit $\tau_{TL} = 22 \pm 6$ fs, and $\tau_{Eff} = 38 \pm 6$ fs. The histogram in Figure 4.5(a) shows that the most frequent probe duration was 23 fs with a few outliers up to 40 fs. Nevertheless, the shortest probe pulses were compressed down to $\tau_{FWHM} = 18$ fs and $\tau_{Eff} = 30$ fs, Figure 4.5(b). For this pulse shape with relatively few low-intensity satellite pulses, the main parameter determining resolution is the Full Width at Half Maximum [84, 94]; thus, the temporal blur with this probe pulse was reduced ~ 2.6 times compared to the original best 46 fs probe duration.

Furthermore, an analysis of the influence of probe energy fluctuation was performed, Figure 4.6. As the probe energy was not measured on-shot, the measured main pulse on-shot near-field profile was used to estimate probe energy within a 1" aperture near the actual probe. Figure 4.6(a) shows the fluctuation of probe energy estimated in this way, compared to the same fluctuation for the 1" aperture at the main beam center. The relative probe energy fluctuation reached up to the value of 0.38 at the highest energies. The dependence of the probe duration (FWHM) on the estimated probe energy is displayed in Figures 4.6(b) and 4.6(c). There was a strong correlation observed at low pulse energies, where the compression was nearly perfect (compared with the ideal compression estimated using [93, 94], open circles). At higher energies, there was a complex dependence due to the interplay of probe energy fluctuation and imperfect compression.

Figure 4.7 shows representative images of the relativistic plasma obtained with the original (a) and down-collimated compressed probe in the shadow (b) and Schlieren (c, d) modes. Each image captures a different shot with similar laser and target parameters. In all images, a time-integrated self-emission can be observed, accumulated during the entire camera exposure time. On the other hand, the ultra-short snapshots of the plasma channel were acquired by the femtosecond probe pulse. In contrast to the original probe (a), where the probe-produced image was barely visible on top of the bright self-emission, the down-collimated compressed probe was clearly visible, although the self-emission was still present.

Further, the images demonstrate that despite the down-collimation and nonlinear process (SPM), the probe near the field profile was sufficiently uniform to produce
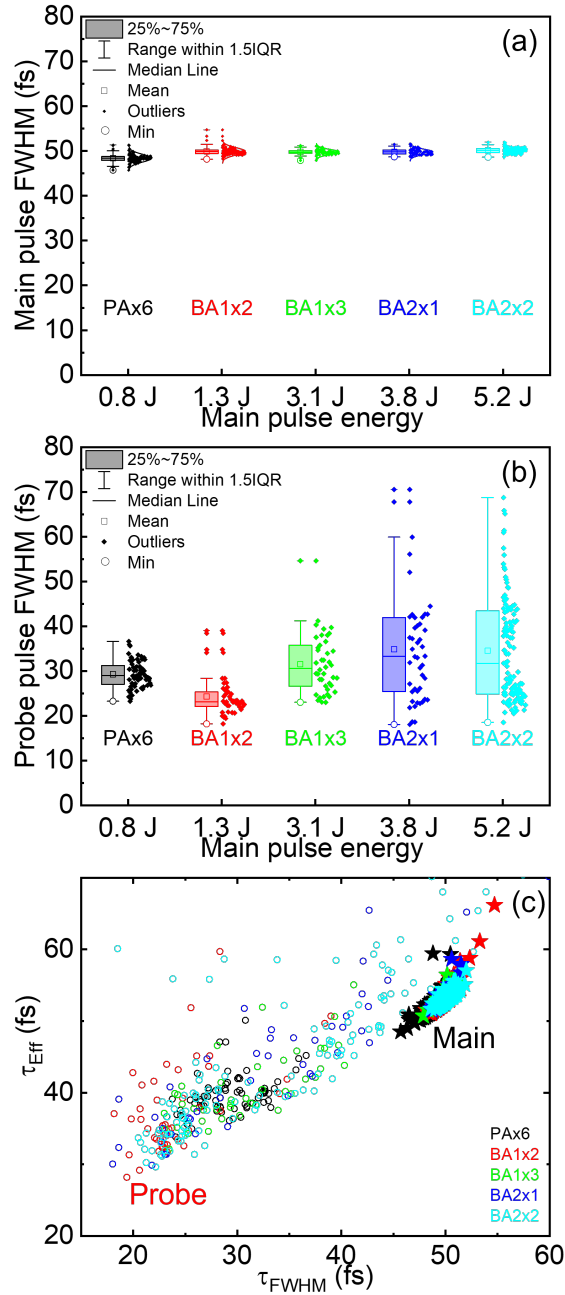
Figure 4.4: On-shot main and probe pulse measurements during one experimental day in several laser modes. The box-and-whisker plots of the main pulse (a) and probe pulse (b) FWHM durations vs. laser mode and main pulse energy. The colored bars represent the 25%-75% ranges, the error bars are the 1.5 interquartile ranges, the horizontal lines are the medians, while the squares, dots, and circles are the means, outliers, and minima, respectively. The dots on the right from the boxes and whiskers are the individual shots forming the corresponding histograms. (c) The main (stars) and probe (rings) pulse on the [FWHM, effective pulse width] plane; each point is an individual shot. Color encodes the laser mode.
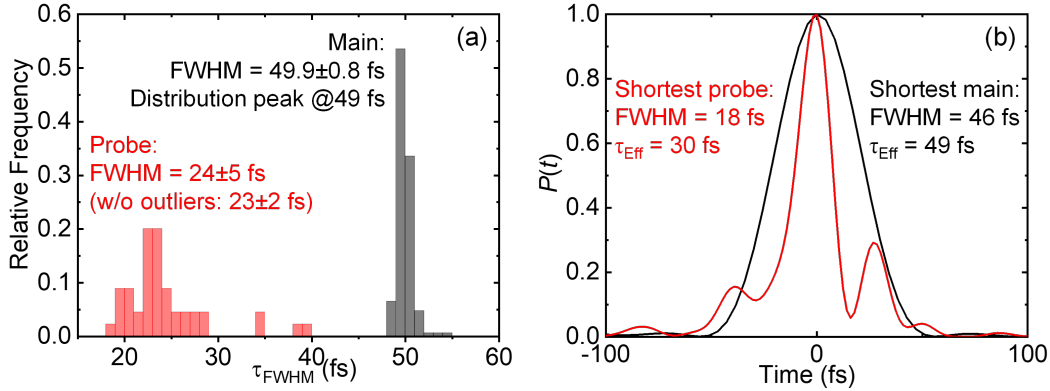
Figure 4.5: Stability of the probe pulse compression and the shortest measured pulses. (a) FWHM histograms for the BA1x2 mode. (b) Shortest main and probe pulses.

high-quality images. In particular, we got rather uniformly illuminated images in the shadow mode. Further, the Schlieren data show that, in case of early probe delay, such as in Figure 4.7(d), there was no signal before (on the right of) the main channel front. This indicates that the probe wavefront quality was sufficiently high. If there were distortions, we would have seen them as an intensity pattern on the plasma-free Schlieren image. The spatial resolution estimated from the smallest self-emission spots was $1.4 \times 1.7~\mu m$.

Using the compressed probe with various plasma density and main pulse energy conditions, we started to see fine fringes with periods from 7 down to $\sim 4~\mu m$, with the fringe periods approximately the same as the expected plasma wavelength. The fringe visibility tended to decrease at shorter periods, indicating that we indeed saw these fringes at the limit of the probe duration (we note that the fringe visibility does not turn to zero abruptly, it decreases when the fringe period becomes short compared to the probe length). A representative example is shown in Figure 4.7(e). These fringes were not observed during many days with the 50 fs probe. Scanning the probe delay with peak plasma density of $\sim 9 \times 10^{21}~cm^{-3}$, we found the velocity of the fringes, $0.87 \times c$. This velocity corresponded to the group velocity of the red-shifted main pulse. These properties correspond to the wakewave, although it needs to be noted that in the regime of relatively high density ($2 \times 10^{19}~cm^{-3}$ up to $10^{20}~cm^{-3}$) and high intensity ($> 10^{20}~W/cm^2$ after self-focusing) there are other singularities as well.

A comparison of our results on the (pulse duration, pulse energy) plane with other works taken from the Review [86] is shown in Figure 4.8.

4.5 Discussion and conclusion of the experiment

The optimum probe pulse compression depends on the laser energy, total nonlinear plate thickness, and number of reflections of the chirped mirrors. In our case in the lowest-energy PA mode the probe phase exhibited some negative chirp, Figure 4.3(a), and the optimum was in the BA1x2 mode, Figure 4.4(b). To shift the optimum to higher-energy modes, preferably, the number of reflections should be increased, or at
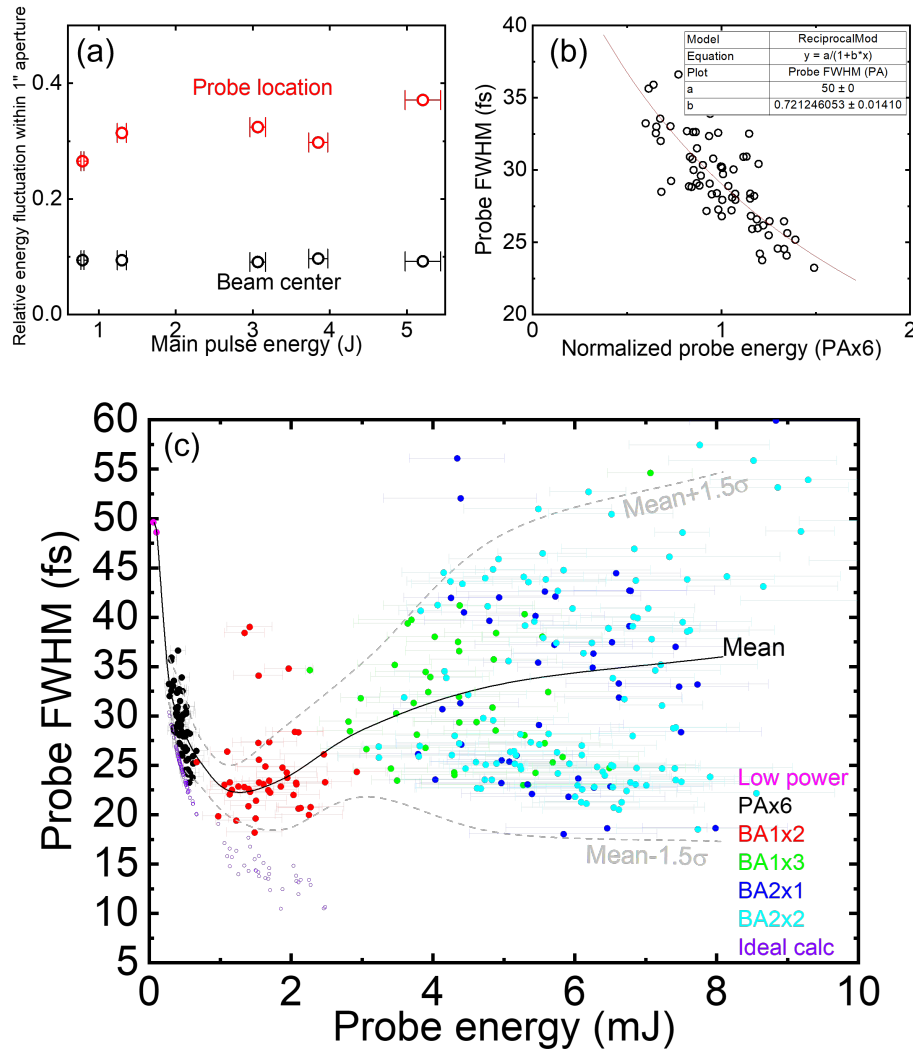
Figure 4.6: Analysis of the dependence of probe pulse duration on the probe and main pulse energy. (a) Relative energy fluctuation (standard deviation divided by mean) in 1" apertures near the edge of the main beam (approximately probe location, red) and at the center of the main beam (black) in different laser modes. (b) Probe pulse duration dependence on the estimated probe energy in the PAx6 laser mode. (c) Probe pulse duration dependence on the estimated probe energy for all studied laser modes (solid circles), and estimated [93, 94] probe duration assuming ideal compression (open circles).
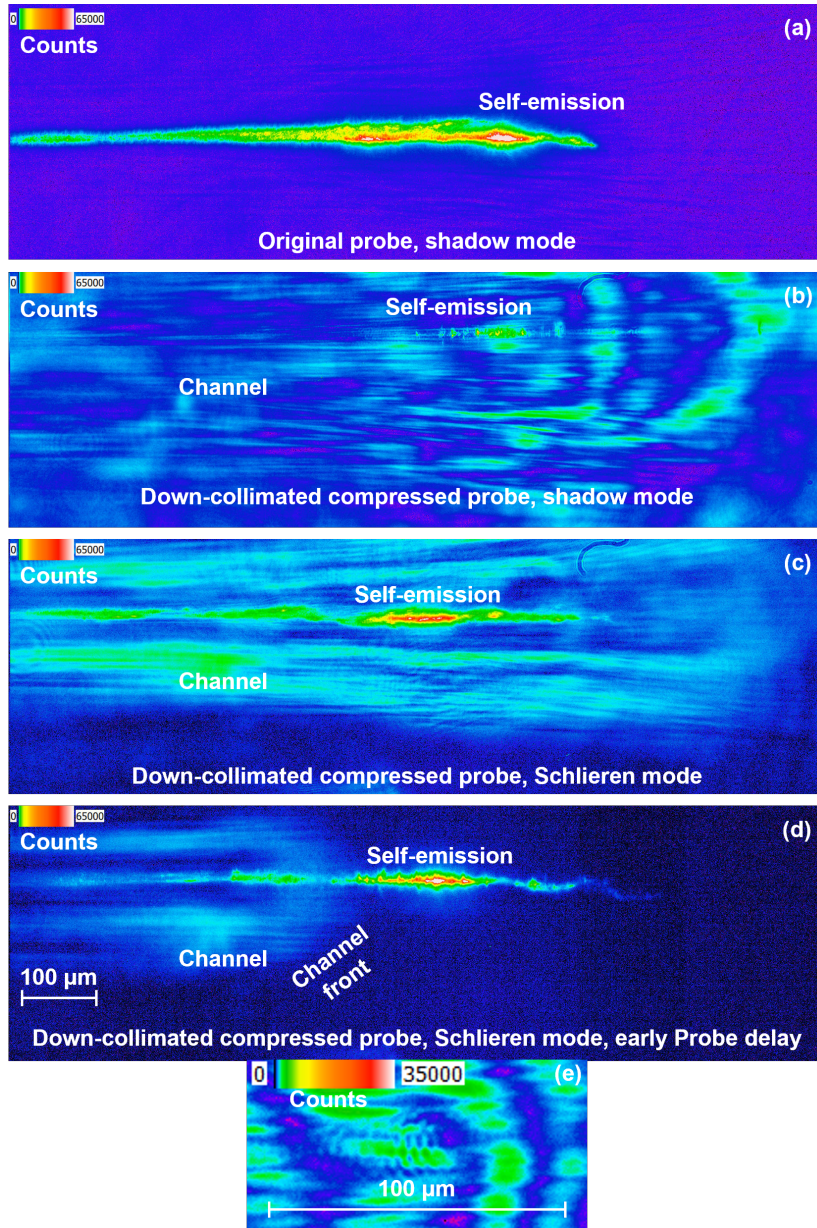
Figure 4.7: (a-d) Representative examples of images produced by the original and down-collimated compressed probe, magnification $M = 10.2$, frame size 1920×600 pix $= 1.1 \times 0.34$ mm. The scale bar shown in (d) is common for (a-d). (a) Original probe, the shadow mode. (b) Down-collimated compressed probe, the shadow mode. (c) Down-collimated compressed probe, the Schlieren mode. (d) Down-collimated compressed probe, the Schlieren mode at an early probe delay. (e) A representative example of fine fringes observed by the compressed probe; note the difference in scale compared to (a-d).
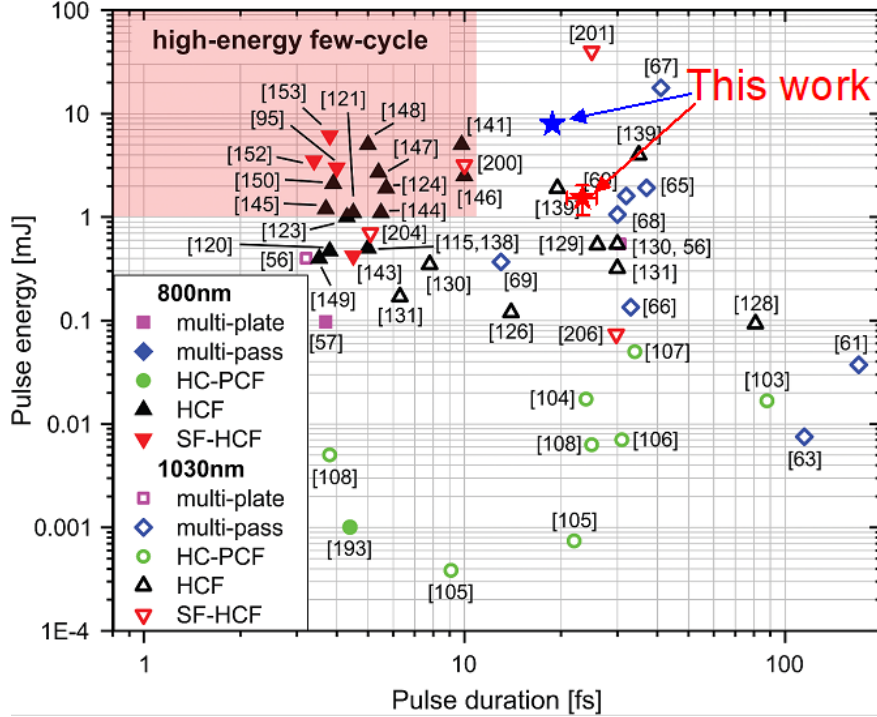
Figure 4.8: Comparison with other works. The average BA1x2 data and best BA2x1 data are shown with the red and blue stars, respectively. The figure with other data is reprinted with permission from [86].

least the number of fused silica plates reduced. These operations were not motorized in the setup and therefore could not be performed within one experimental day, requiring the target chamber venting and opening.

Returning to the potential problems formulated in the Subsection 4.2, the performed experiments demonstrated the following:

Reaching sufficient probe beam peak intensity for efficient SPM in thin plates: The initial probe peak intensity is indeed too low for efficient SPM. The peak intensity can be increased by probe down-collimation, which is also advantageous as it greatly increases the probe-to-self-emission intensity ratio, Figure 4.7.

Shot-to-shot peak intensity variations leading to compressed probe duration fluctuations: The probe duration fluctuates significantly shot-to-shot, Figures 4.4, 4.5. Nevertheless, a similar problem would happen in a fiber-based setup. A possible solution could be the pick-off mirror not at the very beam edge or a mirror with a hole near the beam center for probe pulse extraction.

Compressed probe duration dependence on the main pulse energy: The probe is compressed even when the main pulse energy is changed more than 5 times, which is a practical limit considering optics damage. The minimum probe duration is ~ 18 fs in almost all laser modes. However, the average compression factor depends

on the energy, Figure 4.4. With a single setup, the energy can be changed by a factor of ~ 1.5 on either side from the optimum; for a larger energy variation, an in-vacuum motorized probe attenuator would be desirable. At the optimum energy, the compressed probe duration fluctuations are larger than the main pulse; in our case, the compressed probe duration fluctuated by $\sim 9\%$ with some occasional outliers, while the main pulse duration was stable within $\sim 2\%$, Figure 4.5(a).

Potential degradation of the probe pulse near-field pattern: The down-collimated compressed probe pulse keeps its high quality.

Typically short experimental beam times of high-power user facilities: It is possible to implement the CafCA probe pulse post-compression during a few-week experimental campaign. However, it would be advantageous to implement it as a part of the experimental facility, which would allow its better optimization: in our case, based on the FWHM values of the transform-limited pulses that would give an additional compression by a factor of up to $1.5 - 2$. Also, that would allow additional motorization, e.g. independent insertion of fused silica plates.

In conclusion, we demonstrated a compact in-vacuum setup for down-collimation of a low peak intensity probe laser pulse and compression of its duration using the CafCA approach in the optimum regime from ~ 50 fs down to 24 ± 5 fs (mean $\pm$ standard deviation FWHM value), 23 ± 2 fs (most frequent FWHM value $\pm$ standard deviation without outliers), and 18 fs (the shortest FWHM value), while keeping the pulse synchronized in space and time with the driving laser pulse. Compression to the shortest pulses reduced the motion blur from ~ 15 μm down to $c \times 18$ fs ≈ 5.4 μm, which already allows to study of density micro-structures in relativistic plasma experiments. We characterized the shot-to-shot fluctuations and measured the dependence of the compressed probe pulse parameters on the laser energy while keeping the probe compression setup unchanged; in non-optimum regimes, such as higher-than-optimum pulse energies, larger duration fluctuations were observed. It has been proved that the down-compression allowed efficient SPM and increased the probe-to-self-emission brightness ratio, while not leading to probe image quality degradation.

Chapter 5

Designed targets for LWFA experiments

Many new LWFA accelerators are currently being built and innovated. Therefore there is a high demand for the production of precisely manufactured advanced gas targets. These targets have to be manufactured from a material that can resist extreme conditions such as high vacuum, EMP radiation, high temperature produced in the plasma interaction, and incidence of scattered intense laser beam light. At the same time, the manufacturing technology should be properly chosen to achieve extremely high precision in shapes ($< \pm 5 \ \mu m$) and low surface roughness ($Ra < 1.5 \ \mu m$, Ra is profile average roughness defined in ISO 4287:1997 standard). Last but not least parameter is the cost of the target production, so the laboratories can be equipped with multiple of them. It is common to change the target multiple times during the experimental campaign due to the decay of the targets after many thousands of shots or due to accidental damage by getting hit by the laser beam.

5.1   Micro-nozzles for kHz acceleration

An electron accelerator driven by L1-Allegra kHz repetition rate laser is under development in ELI-Beamlines. The designed L1 laser parameters are specified in the
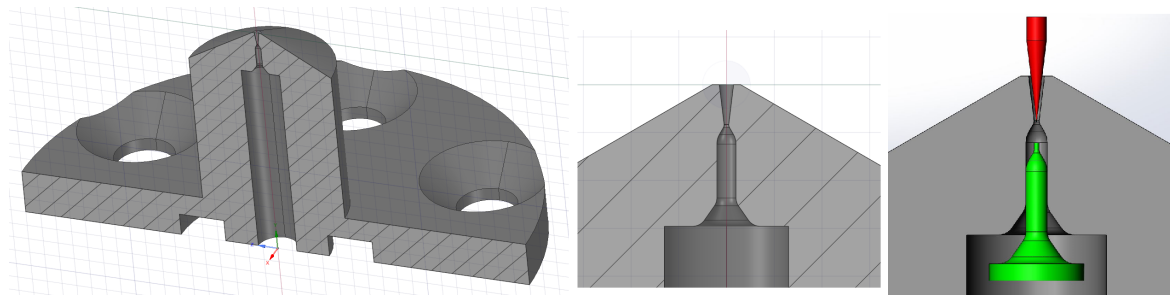

Figure 5.1: Diagram of 300 μm micro-nozzle for kHz LWFA accelerator. Left: 3D model of the nozzle. Centre: Detail on the shape. Right: Scheme of the EDM electrodes used to mill the shape of the nozzle.

Table 1.1. The accelerator should provide an electron beam with kHz repetition rate and energy in the range of 10-100 MeV.

Since the dephasing and depletion lengths are of the order of hundreds of μm special micro-nozzles with flat-top profiles had to be designed and manufactured. The design and characterization have been performed by steady CFD simulations and interferometric measurements with the 4-pass interferometer setup. The nozzles have a flange for connection with SmartShell and Parker high-speed valves. The nozzles were manufactured in 3 sizes of nozzle exhaust: 300, 450, and 600 μm. See the design of 300 μm nozzle in Figure 5.1.
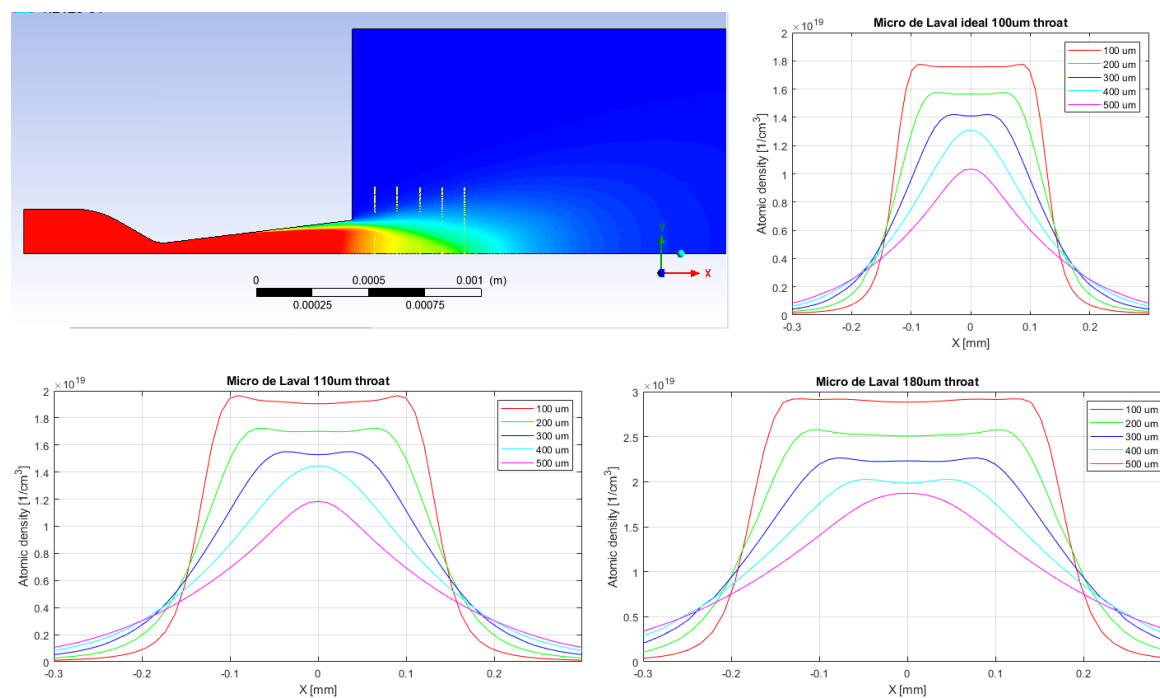

Figure 5.2: Numeric simulation of gas flow in three nozzles - one is the ideal shaped nozzle and two which were manufactured incorrectly. The backing gas is nitrogen at 10 bar. Top left: Density map of the ideal nozzle with 100 μm throat. The yellow lines mark the lines in which the density profiles are plotted. Top right: Density profiles of the ideal nozzle in lines with different heights above the nozzle. Lower left: Nozzle manufactured with 110 μm throat. Lower right: Nozzle manufactured with 180 μm throat.

To ensure the smoothness and flatness of the density profile, the micro nozzles have to be manufactured with high precision. Therefore an Electric Discharge Machining (EDM) method was implemented in the manufacturing process to precisely cut the nozzle shape. EDM is a metal fabrication process whereby a desired shape is obtained by using electrical discharges. Material is removed from the workpiece by a series of rapidly recurring current discharges between two electrodes, separated by a dielectric liquid and subject to an electric voltage. Two electrodes with the negative shape had to be manufactured to be used for milling the micro-nozzle shape (see Figure 5.1).

The most challenging part of the EDM machining of the micro-nozzles is the precise positioning of the 2 electrodes. If one of the electrodes is inserted deeper than it should be, the nozzle throat cross-section increases, and the nozzle throat-to-exhaust ratio changes. A simulation study has been performed to see how the manufacturing inaccuracy affects the flatness of the density profile. The 300 μm nozzle with nitrogen and 10 bar backing pressure has been simulated using the steady CFD method. The results are depicted in Figure 5.2. It can be seen that the manufacturing imprecision caused by the wrong positioning of the electrodes does not affect the flatness of the density profile, however, it changes its height.

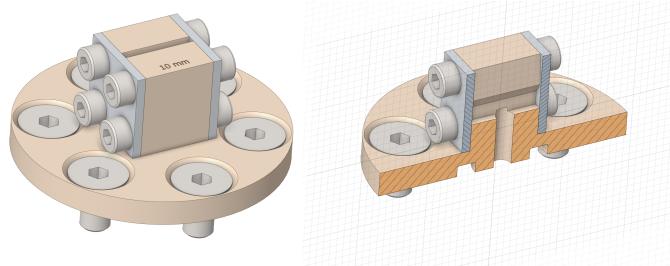## 5.2 Slit nozzles for PW laser experiments

Figure 5.3: Design - (left) overview and (right) cut of 10 mm slit supersonic nozzle without reservoir.

Laser wakefield electron acceleration experiments driven by PW-class lasers require gas targets with lengths 10-1000 mm depending on the intensity of the laser in focus, laser beam guiding technique, and injection scheme. In order to create a gas target that allows an easy alignment and free space for laser plasma diagnostics, various slit supersonic nozzles were designed. All these nozzles are designed to be manufactured by wire-EDM technology from stainless steel.

Depending on the design, we can divide the slit nozzles into 3 kinds:

1. **Fast nozzles without reservoir (length 4-12 mm)**: Nozzle designed for the very short opening time of the gas valve (< 4 ms), which reduces gas load into the vacuum chamber while performing high repetition rate operation. The drawback of the absence of the reservoir is that the nozzle creates two density peaks (up to 30 % increase of the density) near the side walls. These peaks can be lowered by side wall tapering. See the design and density profile of the 10 mm slit nozzle without reservoir in Figures 5.3 and 5.4.

2. **Mid-length nozzles with reservoir and one gas supply valve (length 12-50 mm)**: Nozzles are designed for longer acceleration lengths (> 12 mm) while implementing only one gas valve. A gas reservoir with a barrier in the center deflects the inlet gas flow and avoids density drop in the gas target flat-top density profile. See the design and density profile of the 30 mm slit nozzle with reservoir in Figures 5.5 and 5.6.
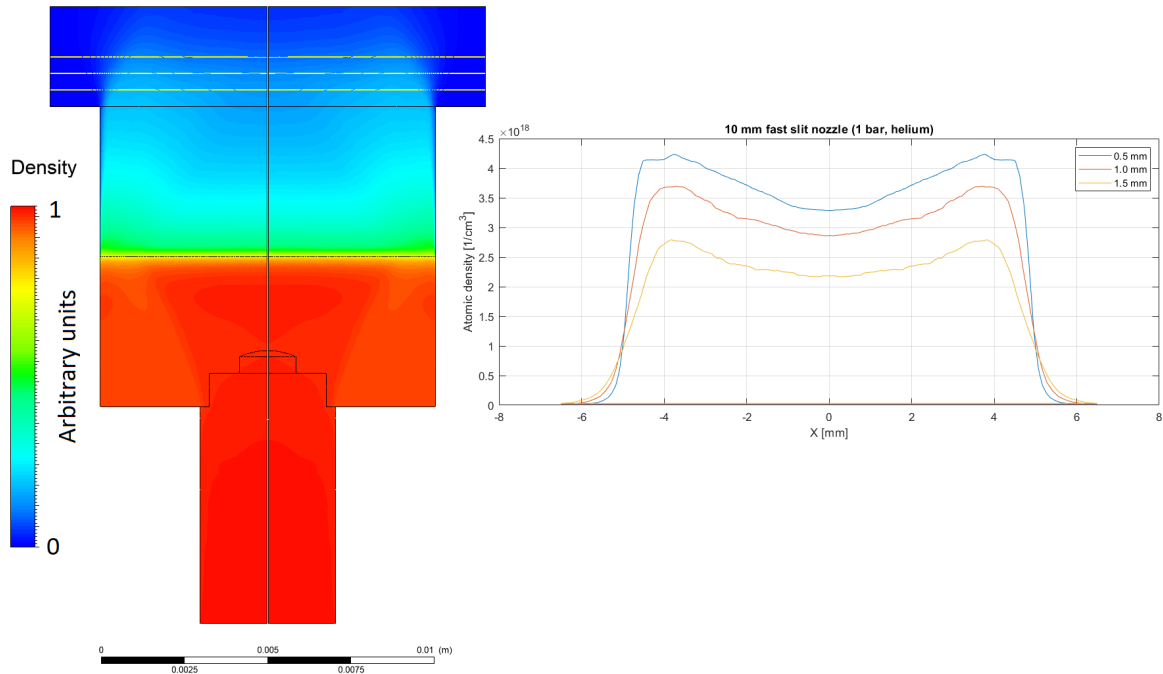
Figure 5.4: Characterization of the density profile of the 10 mm slit nozzle without reservoir by hydrodynamic simulation. (left) 2D density map of the cross-section of the nozzle in arbitrary units. (right) density profile plots in the laser axis direction at different heights above the nozzle. The results are obtained for the SmartShell gas valve, helium gas at 1 bar backing pressure.

Figure 5.5: Design - (left) overview and (right) cut of 30 mm slit supersonic nozzle with reservoir.

3. **Long nozzles with multiple valves (lengt > 50 mm)**: Nozzles are designed for very long acceleration lengths. In such targets, the implementation of multiple gas valves is required. Gas reservoir suppresses variations in the density profile initiated by interacting gas flow from multiple valves. See the design and density profile of the 200 mm slit nozzle fed by three Parker valves in Figures 5.7 and 5.8.

The choice of the design is not strictly determined only by the length, but also by

Figure 5.6: Characterization of the density profile of the 30 mm slit nozzle with reservoir by hydrodynamic simulation. (left) 2D density map of the cross-section of the nozzle in arbitrary units. (right) density profile plots in the laser axis direction at different heights above the nozzle. The results are obtained for the SmartShell gas valve, helium gas at 1 bar backing pressure.
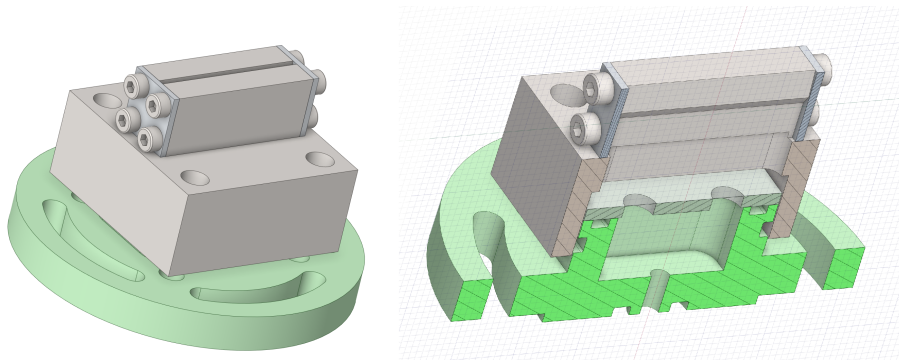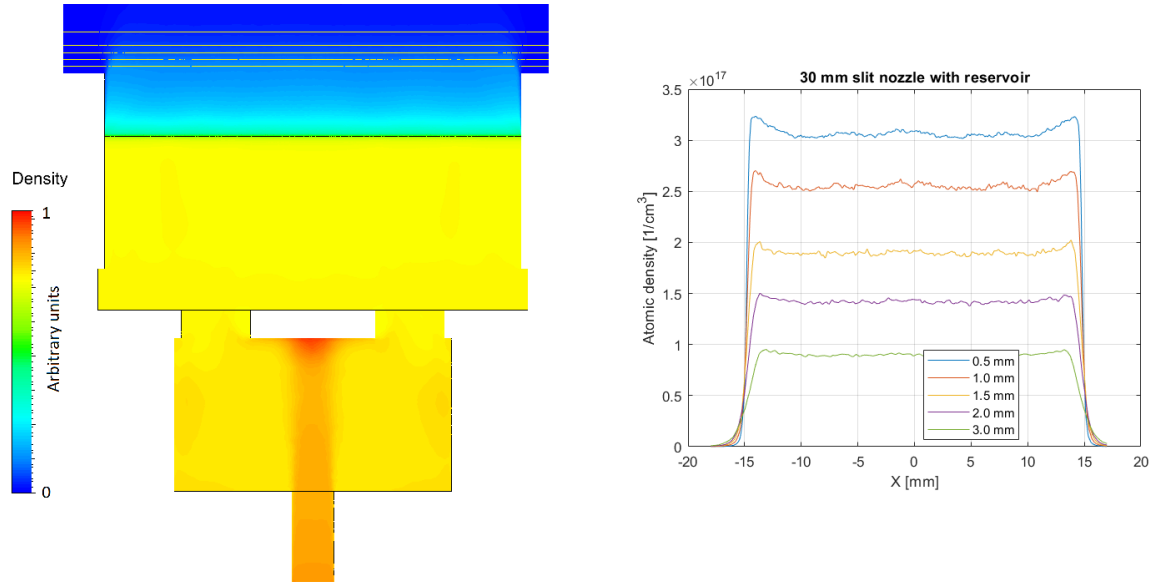

Figure 5.7: Design - (left) overview and (right) cut of 200 mm slit supersonic nozzle with reservoir and connection to multiple gas valves.

other requirements specific to each experiment. Therefore the unique design of the slit nozzle has to be done for a specific experimental setup.

5.3 Slit nozzle with injector section

This specific target was originally designed for laboratory astrophysics experiments with 10 PW-class lasers. However, it can also be favorably used for density drop injection or ionization injection in LWFA experiments. The target design (see Figure 5.9) is implementing two supersonic nozzles separated by a 0.5 mm wall, where the
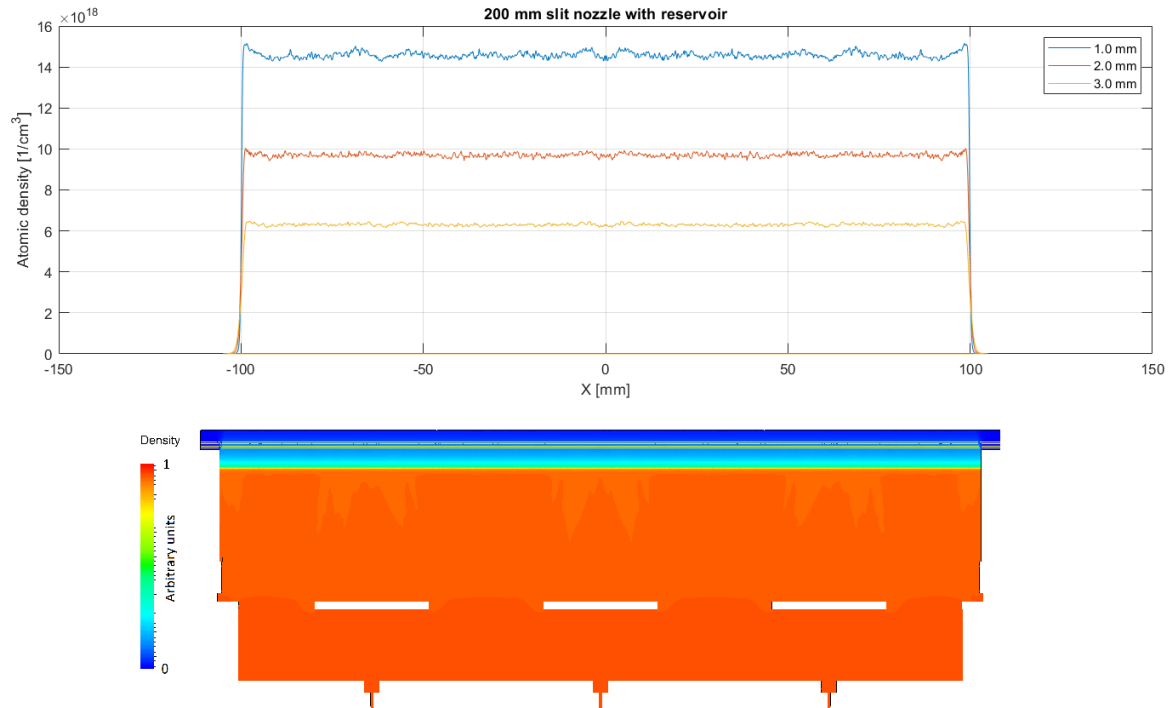
Figure 5.8: Characterization of the density profile of the 200 mm slit nozzle with reservoir and 3 gas valves by hydrodynamic simulation. (bottom) 2D density map of the cross-section of the nozzle in arbitrary units. (top) density profile plots in the laser axis direction at different heights above the nozzle. The results are obtained for the Parker gas valve, helium gas at 5 bar backing pressure.
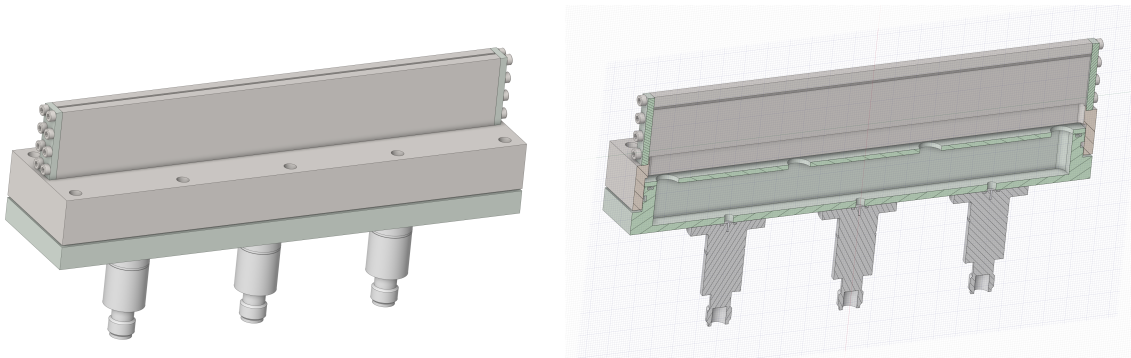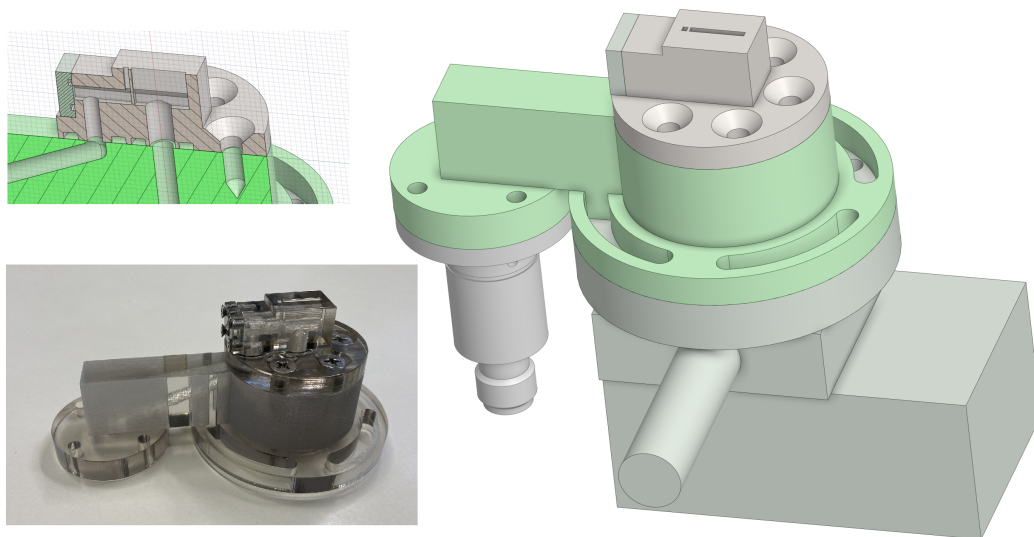

Figure 5.9: Design of the slit nozzle with injector section (right) with SmartShell and Parker valves, its top part cross-section (top left), and photography of the device printed on precision resin 3D printer (bottom left).
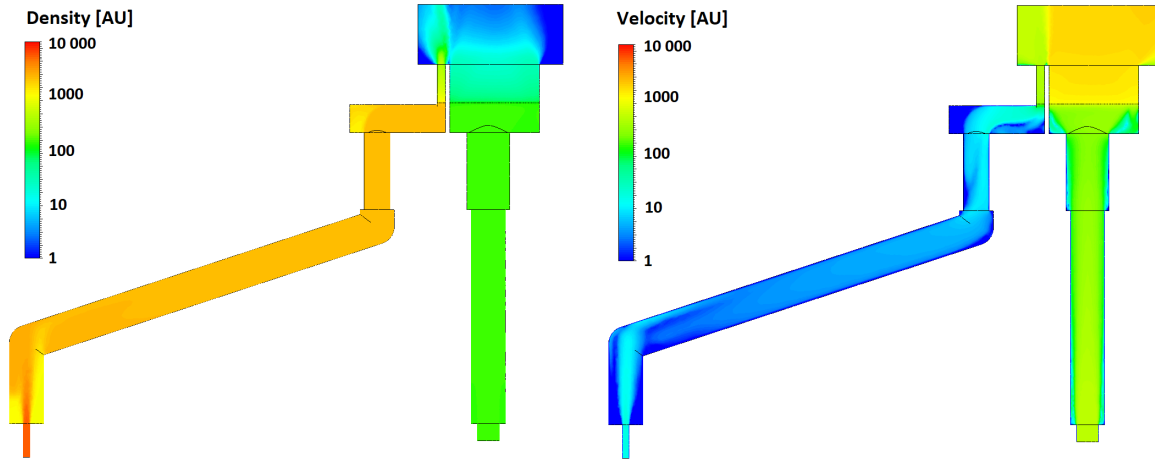
Figure 5.10: Illustration of gas flow through the slit nozzle with injector section from CFD simulation. The device has two inlets, where each inlet can be connected to a different gas. (left) Gas density in arbitrary units [AU] and logarithmic scale. (right) Gas velocity in arbitrary units [AU] and logarithmic scale.
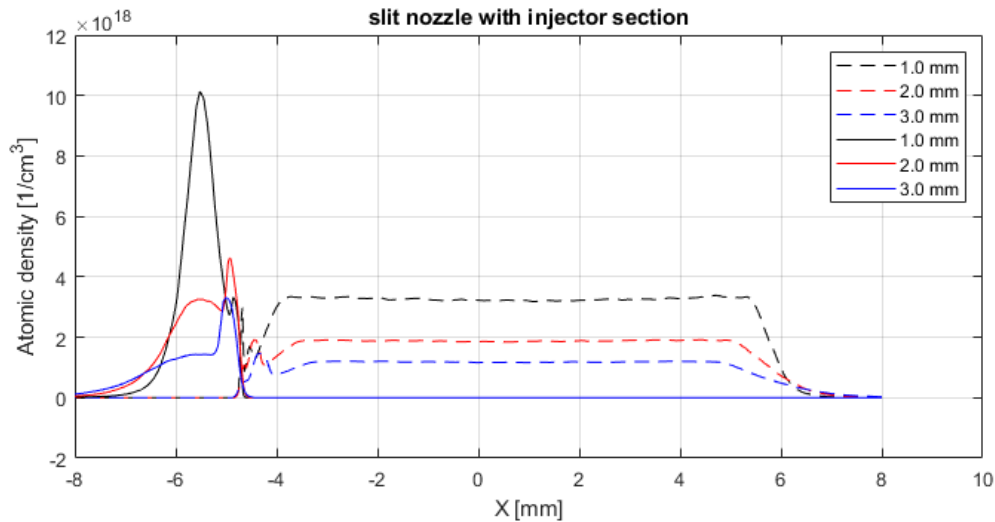
Figure 5.11: Density profile of 10.5 mm slit nozzle with 1 mm injector section at different heights above the nozzle (1.0, 2.0 and 3.0 mm). The solid line represents gas flowing from the injector section and the dashed line is the gas coming from the slit nozzle. In this case, the xenon at 3 bar for the injector inlet and helium at 1 bar for the slit nozzle inlet were used to optimize the target for laboratory astrophysics experiments.

short one (1 mm) serves as injector and the long one (scalable 3-12 mm) serves as an accelerator. The target is designed to allow space for various plasma diagnostics.

The target is fed from 2 separate high-speed gas valves to drive the gas flow conditions in each section separately. The distribution of the gas density and absolute velocity inside the target body can be seen in Figure 5.10. The density profile of the

target has a peak in the beginning, then it is followed by a shock down-ramp and continues with plateau density (see Figure 5.11). The peak-to-plateau ratio can be adjusted online during the experiment by remotely driving the inlet densities of the gas valves and by changing the distance of the nozzle from the laser axis.

5.4   Dual-stage target for reduced gas load

Implementation of the LWFA accelerator for standard everyday research, industry, or medical use comes with the following demands on the accelerator:

- High-quality electron beam parameters - compactness, monoenergecity

- Robustness and stability

- Easy scalability

- Reducing material and manufacturing costs

- Ease-of-use

We believe that the best way to achieve this is to implement a self-guided regime with a localized injection scheme as sharp density transition or ionization injection.

The target for stable high repetition rate electron acceleration should be in a continuous flow regime. However, this together with the increasing peak power of the lasers brings high gas loads into the vacuum chamber. Two target technologies are available for density drop injection. First, supersonic nozzles with induced shock waves can be used. However, with a high-power laser, the nozzle has to be elongated, which brings an extremely high gas load and it is more challenging to maintain the flatness of the density profile. Another option is the connection of two gas cells, which reduces the gas load. Nevertheless, the density transition between the two gas cells is not sharp enough to produce the desired density drop.

Therefore a new solution that combines a supersonic nozzle with a gas cell in one solid body device is proposed. The design of the target is presented in Figures 5.12 and 5.13. This combination allows the creation of the steep density drop in the profile and variable length flat part of the profile while keeping a low gas load into the vacuum chamber.

During the design process, the hydrodynamic simulations were performed to find the best inner shape of the target to produce a smooth density profile without a drop between the two stages and with short gradients at the inlet and outlet of the target. Simulation results for the final design are shown in Figure 5.14.

The newly proposed target brings the following advantages:

- Low gas load into vacuum chamber even for very long plateau part of the profile

- Versatility - a different gas can be used for each stage

- Scalability - easiness of driving the density in each stage by adjusting the backing pressures
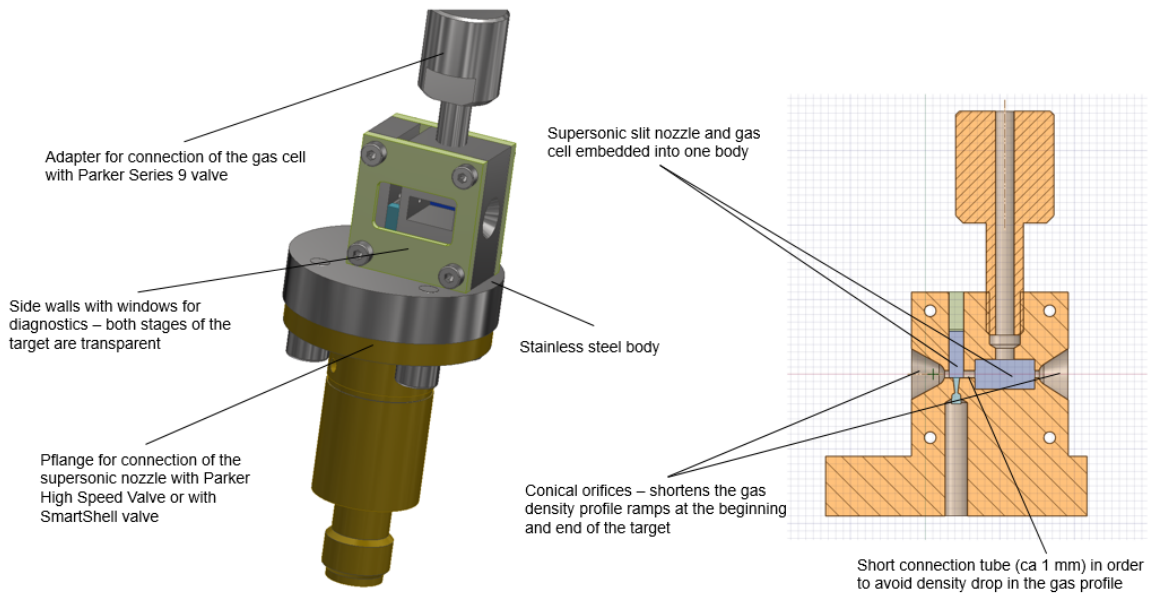
Figure 5.12: Dual-Stage target design. Left: 3D CAD model. Right: Cross section.
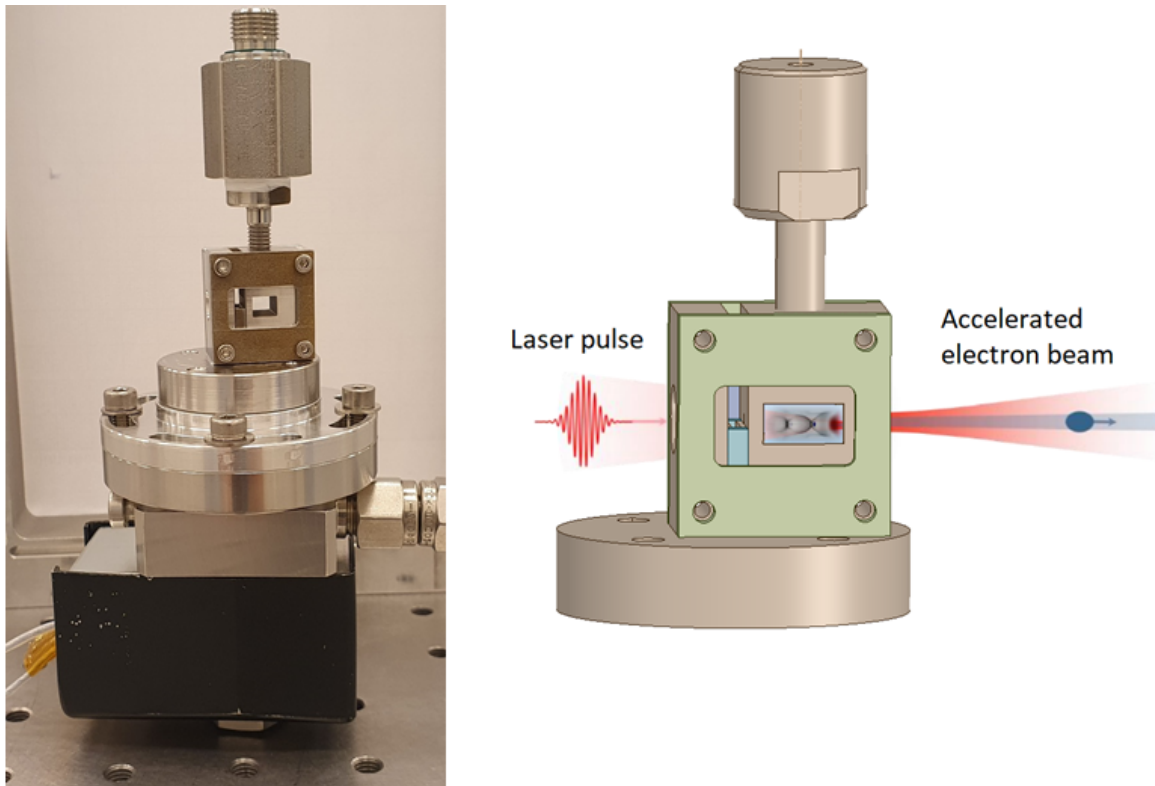
Figure 5.13: Dual-Stage target design. Left: Photo of a first manufactured prototype. Right: Acceleration scheme.

- Possibility to use the same target for ionization injection (mixture of light and heavy gas in the nozzle stage)
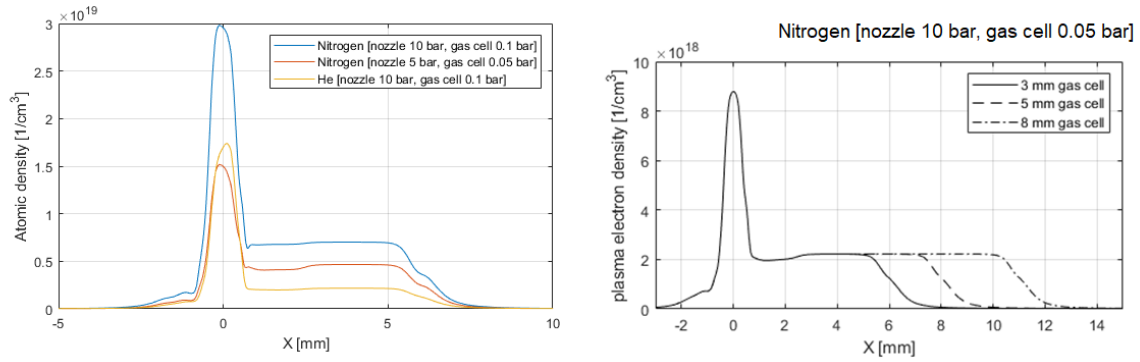
Figure 5.14: Density profiles of the neutral gas calculated by hydrodynamic simulations. Left: Density profiles for 3 mm long gas cell stage for different gasses and pressures. Right: Density profiles for different lengths of the gas cell stage.

- Large windows for diagnostics of the neutral gas or plasma inside both stages of the target

- Robust body of the target, no mowing parts

- Cheap manufacturing costs - in case of damage it can be easily replaced

- The design comes with adapters for widely used valves in the community (Parker, SmartShell)

Chapter 6

LWFA experiments at ELI Beamlines

ELI Beamlines Facility is a leading laser research centre and part of The Extreme Light Infrastructure ERIC, pan-European research Infrastructure hosting the world's most intense lasers. ELI provides unique tools of support for scientific excellence in Europe. ELI Beamlines has developed and operates four leading-edge high-power femtosecond laser systems reaching unprecedented intensities. ELI Beamlines offers to its users unique femtosecond sources of X-rays and accelerated particles. These beamlines enable pioneering research not only in physics and material science but also in life science, laboratory astrophysics, and chemistry with strong application potential.

Currently, several of the main laser beamlines are operational and are being expanded and upgraded to reach their full performance and maximum availability. Other laser beamlines are in commissioning and new cutting-edge laser sources are in the design and development phase.

6.1   Allegra Laser for Acceleration (ALFA)

ALFA (Allegra Laser For Acceleration) is the first laser-plasma electron accelerator of its kind, being based on the unique capabilities of the high average power, and high repetition rate (1 kHz) L1-Allegra laser[103]. ALFA enables to carry out of laser-matter interaction experiments at relativistic intensity and, in addition, delivers ultra-short electron beams (few fs) at a tuneable frequency (up to 1 kHz) and with tuneable energy (< 50 MeV).

The beamline is open to scientific user community. The optical setup available at ALFA enables users to carry out research in the field of laser-matter interaction at relativistic intensities ($\sim 5 \times 10^{18}~W/cm^2$) and very high repetition rate (1 kHz). Such unique capability has already been demonstrated at ALFA for the optimization of kHz laser wakefield plasma acceleration to deliver ultra-relativistic (< 50 MeV), ultra-short (few fs) electron beams intrinsically synchronized with additional laser pulses. These unique features call for applications in the fields of very high energy (VHEE) radiotherapy and dosimetry, x-ray generation by Thomson scattering and betatron
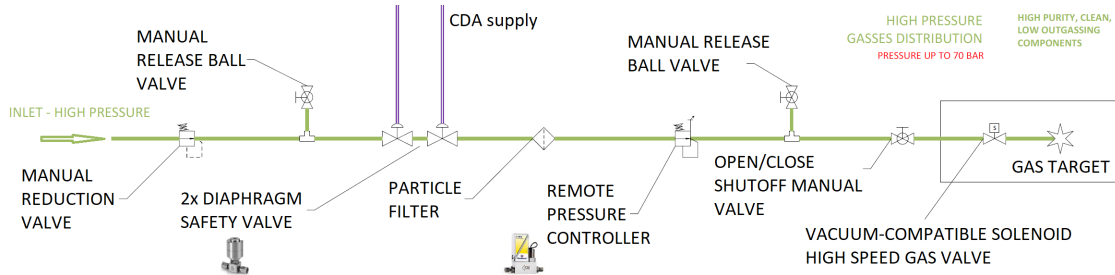
Figure 6.1: Diagram of the ALFA gas supply system. The green line denotes the inlet gas for the target. The purple line denotes the external compressed decontaminated air (CDA) supply used to operate the safety valve. The black rectangle marks the walls of the vacuum chamber.

radiation, ultra-fast radiobiology and radiochemistry, and radiation effect on electronics research.

6.1.1 System description

ALFA is located in the laser hall L1 and is driven by the L1-Allegra laser. The laser system is designed to generate < 20 fs pulses with energy exceeding 100 mJ per pulse at a high repetition rate (1 kHz). The concept of the laser is based entirely on the amplification of frequency chirped picosecond pulses in an optical parametric chirped pulse amplification (OPCPA) chain consisting of a total of seven amplifiers. The OPCPA amplifier stages are pumped by precisely synchronized picosecond pulses generated by state-of-the-art thin-disk-based Yb:YAG laser systems. The summary of design and actual (for the year 2023) parameters is noted in Table 6.1.

Feature	Designed	Actual (2023)
Output pulse energy	100 mJ	30 mJ
Pulse duration	< 20 fs	15 fs
Repetition rate	1 kHz	1 kHz
Central wavelength	830-860 nm	750-920 nm

Table 6.1: Summary of the design and actual (2023) parameters of L1-Allegra laser system.

This laser's key features for LWFA are its multi-stage power scalable design (final output expected up to 100 mJ), the absence of nanosecond contrast being pumped by 3 ps Yb:YAG thin-disk lasers and its power and pointing stability (few % level) over many hours of continuous operation.

The L1-Allegra laser pulses are characterized (near field, time duration, and spectrum) before its injection into the ALFA accelerator vacuum chamber. The laser pulses are focused by a 76.2 mm focal length off-axis parabola into in-house designed and characterized gas jet targets - see Section 5.1.
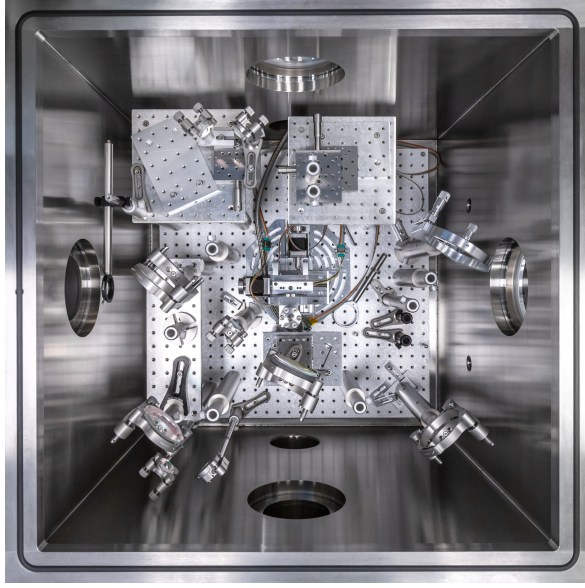
Figure 6.2: Top view of the ALFA vacuum chamber and the optical setup inside.

The gas target is supplied by a sophisticated gas system, as illustrated in Figure 6.1. The ALFA gas supply system is optimized to accommodate backing pressures of up to 70 bar, and it offers the flexibility to use any inert gas or their mixtures. The system comprises several components, including a gas bottle (up to 300 bar), a manual reduction valve, a safety shut-off valve system, a particle filter with a pore size of 0.5 µm, a remote pressure controller, two release ball valves, a vacuum-compatible high-speed gas valve from Parker Hannifin Corp., and finally, the gas target itself.

Thanks to the ALFA vacuum chamber's dedicated turbo-molecular vacuum pump, which operates independently from the laser compressor chamber, and thanks to very small nozzle throat (diameter of 100 μm), the system enables continuous flow operation of the target over multiple seconds.

The accelerated electron beams are characterized by an electron spectrometer. The system of the LANEX screen coupled to the camera has been calibrated on a tunable medical linear electron accelerator and is designed to measure the electron energies from 1 to 100 MeV. The laser diagnostics are FROG (time duration), near field, and focal spot (offline and in-air at low power, with microscopic objective). The laser energy and spectrum are measured on a shot-to-shot basis. The laser-plasma diagnostics are ultra-short probe beam synchronized with a delay line (from mirror leak), shadowgraph, interferometer, and multi-channel Thomson scattering. All the ALFA setup is arranged inside $0.8 \times 0.8 \times 0.6$ m vacuum chamber - see Figure 6.2.

6.1.2 Commissioning experiment 2022

During the 2022 commissioning experiment, the L1-Allegra laser was operated with six amplification stages, resulting in a pulse energy of 26 mJ measured inside the interaction chamber. The laser pulses were focused down to a measured focal spot size (see Figure 6.3a)) with full width at half maximum (FWHM) values of 4.2 µm and 3.1
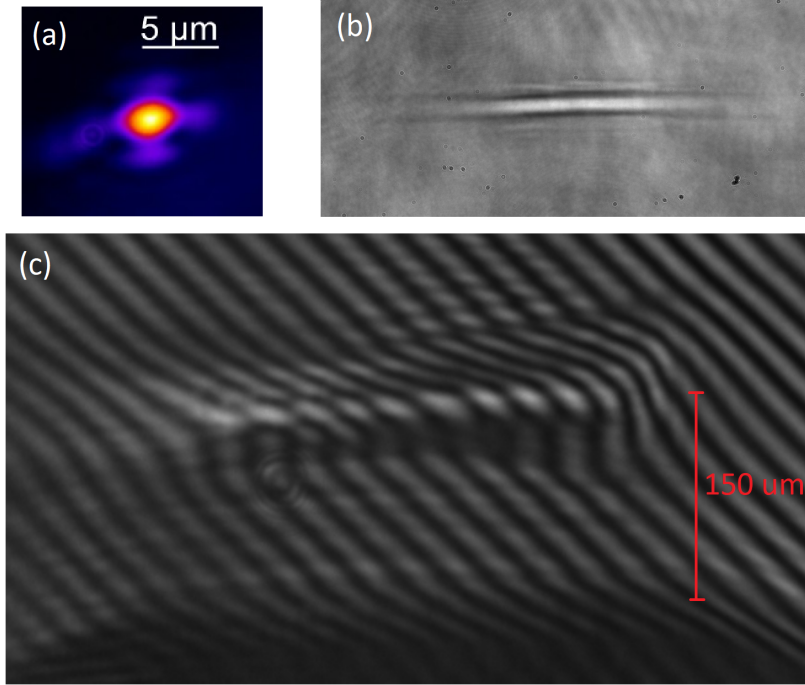
Figure 6.3: Data from ALFA diagnostics. (a) Focal spot measurement. (b) Shadowgraphy side-view of the plasma channel (c) Side-view interferometry of the plasma density.

µm along the horizontal and vertical axes, respectively. The laser power delivered to the target was $P_{laser} = 1.7$ TW, significantly exceeding the self-focusing threshold $P_{SF} = 0.52$ TW, considering the optimal electron density for this experiment, $n_e = 5.7 \times 10^{19}$ cm^{-3}. This facilitated self-guiding within the plasma, as evidenced by the side-view shadowgraphy diagnostic (Figure 6.3b).

The laser pulse was focused in the first half of the 300 µm diameter flat-top gas jet (refer to Section 5.1), positioned 150 µm above the nozzle exhaust (Figure 6.3c). The gas target position was meticulously optimized in three dimensions with precision at the level of the plasma wavelength $\lambda_{plasma} = 4.5$ µm, ensuring the optimal focusing position within the plasma profile. The characteristics of the accelerated electron beams were analyzed using a calibrated electron spectrometer, consisting of a 0.1 T permanent magnetic dipole and a LANEX Fast Back scintillator screen.

A critical aspect of the alignment process involved synchronizing the arrival of the laser pulse with the opening of the gas valve. Interferometric measurements and computational fluid dynamics simulations revealed that the gas flow inside the micro nozzle targets stabilizes after approximately 5 ms. Consequently, shots arriving before this time failed to achieve the desired plasma density profile necessary for stable acceleration.

The gas pressure has been then tuned by an electronic valve to achieve simultaneously relativistic self-focusing and electron injection in the plasma wave. The laser pulses have been delivered on target at a 1 kHz repetition rate for the whole duration of the experiment, to reach thermal equilibrium in all the system components. The gas jet opening time, synchronized with the arrival of the driving pulse by a trigger, was set

as either pulsed or continuous, depending on the regime of operation. The possibility of running continuous gas flow kept the laser-driven acceleration process throughout several hours of continuous operation.
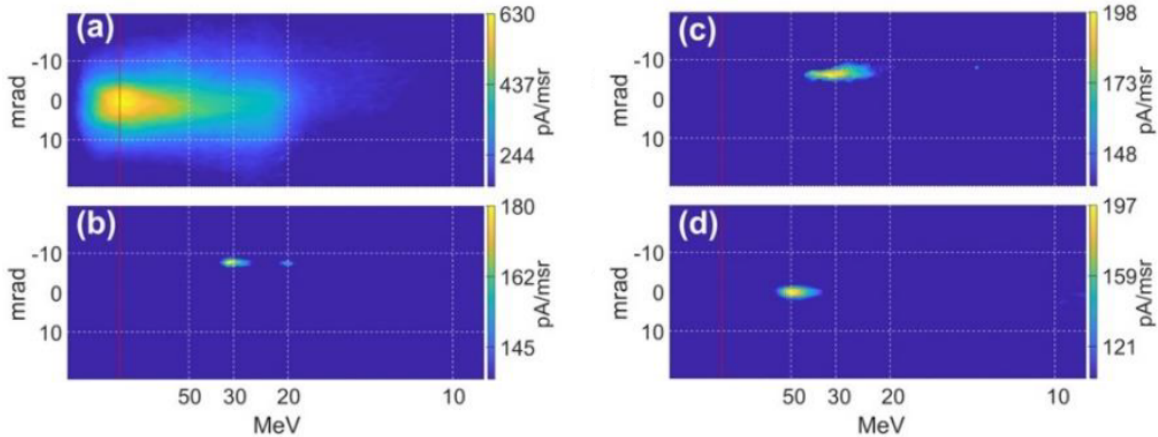

Figure 6.4: High-energy quasi-monoenergetic electrom beams produced with ALFA beamline[104]. (a) Reference electron trace on Lanex without magnetic field for the Nitrogen-Helium mixture target operating at a plasma density $n_e/n_{cr} = 0.034$. (b-d) Selected spectra with magnetic field on, showing monoenergetic characteristics. In (d) is shown the 50 MeV energy spectrum.

Feature	High energy mode	High power mode
Energy	32 ± 5 MeV	22 ± 2 MeV
Energy spread (FWHM)	8 MeV (25%)	15 MeV (68%)
Current	12 ± 6 pA	276 ± 28 pA
Divergence (FWHM)	2.1 ± 0.8 mrad	7.8 ± 1.2 mrad
Electron beam power output	0.4 mW	6 mW

Table 6.2: ALFA electron beam averaged parameters for the high energy and the high power modes[104].

The most energetic and collimated electron beams have been obtained by shooting the laser on a gas mixture of Helium (98%) and Nitrogen (2%), which allowed acceleration at an electron plasma density as low as $n_e = 5.7 \times 10^{19}$ cm^{-3}. This corresponds to a fraction of the plasma critical density $n_e/n_{critical} = 0.034$. In this configuration, record-high energy electron beams have been obtained, as detailed in our work C. M. Lazzarini et al., "50 MeV electron beams accelerated by a terawatt scalable kHz laser", arXiv:2302.11415, 2023 [104], with enery up to 50 MeV (Figure 6.4d). By averaging over thousands of shots (a sample of which is shown in Figure 6.4b-d) we observed an average energy of 32 ± 5 MeV (std), with an average energy spread of 8 MeV (25%, FWHM), and a beam divergence of 2.1 ± 0.8 mrad (FWHM). The LWFA process in this new space of parameters presents new challenges. In fact, despite obtaining very stable electron beams in the optimal configuration, small changes in any parameter can significantly affect the acceleration process.

Given the reliance of medical applications on high-current electron beams at energies exceeding 20 MeV, we have fine-tuned our LWFA source to operate in two distinct modes: the high-energy mode and the high-power mode. In the former, illustrated in Figure 6.4a-d, we maximize beam energy and collimation by adjusting laser-plasma interactions at the lowest achievable plasma density, considering the available laser power. This configuration enables operation of the accelerator at a 1 kHz repetition rate with a continuous flow target (i.e., gas valve open over many thousands of shots).

Conversely, in the high-power mode, we prioritize optimizing electron beam power by operating at a slightly higher plasma density, albeit at the expense of average peak energy and collimation. The key parameters characterizing these two modes of operation are summarized in Table 6.2.

6.2 Electron Beamline for Fundamental Science (ELBA)

ELBA (Electron Beamline for Fundamental Science) is the first all-optical laser-electron collider of its kind, being designed on the unique capabilities of the high average power, high repetition rate L3-HAPLS laser (30 J, 30 fs, 10 Hz). These unique features call for applications in the fields of laser wakefield acceleration, muon generation, laser-electron collider experiments, and nonlinear QED experiments at high repetition rates ($\sim$100 000 shots per day).

6.2.1 System description

The ELBA beamline is driven by an L3-HAPLS laser, which is designed to deliver PW pulses with energy of at least 30 J and duration $<$ 30 fs, at a repetition rate of 10 Hz. This system was developed at the Lawrence Livermore National Laboratory, with ELI-Beamlines cooperating on the development of the PW pulse compressor, the short-pulse diagnostics, and the short-pulse part controls and timing. The laser pump engine employs two Nd-doped glass amplifiers operating at 10 Hz, which are cooled by helium gas. Each amplifier is pumped by high-power laser diode arrays. The beam format is rectangular super-Gaussian with the size 214 $\times$ 214 mm. The summary of the design and actual (for the year 2023) parameters is noted in Table 6.3.

Feature	Designed	Actual (2023)
Output pulse energy	30 J	13.3 J
Pulse duration	$<$ 30 fs	27.3 fs
Repetition rate	10 Hz	3.3 Hz
Peak power	1 PW	0.49 PW
Central wavelength	810 nm	810 nm

Table 6.3: Summary of the design and actual (2023) parameters of L3-HAPLS laser system.

ELBA is located in the underground radiation-shielded experimental hall E5. L3-HAPLS laser pulses propagate for 108 meters after the grating compressor before
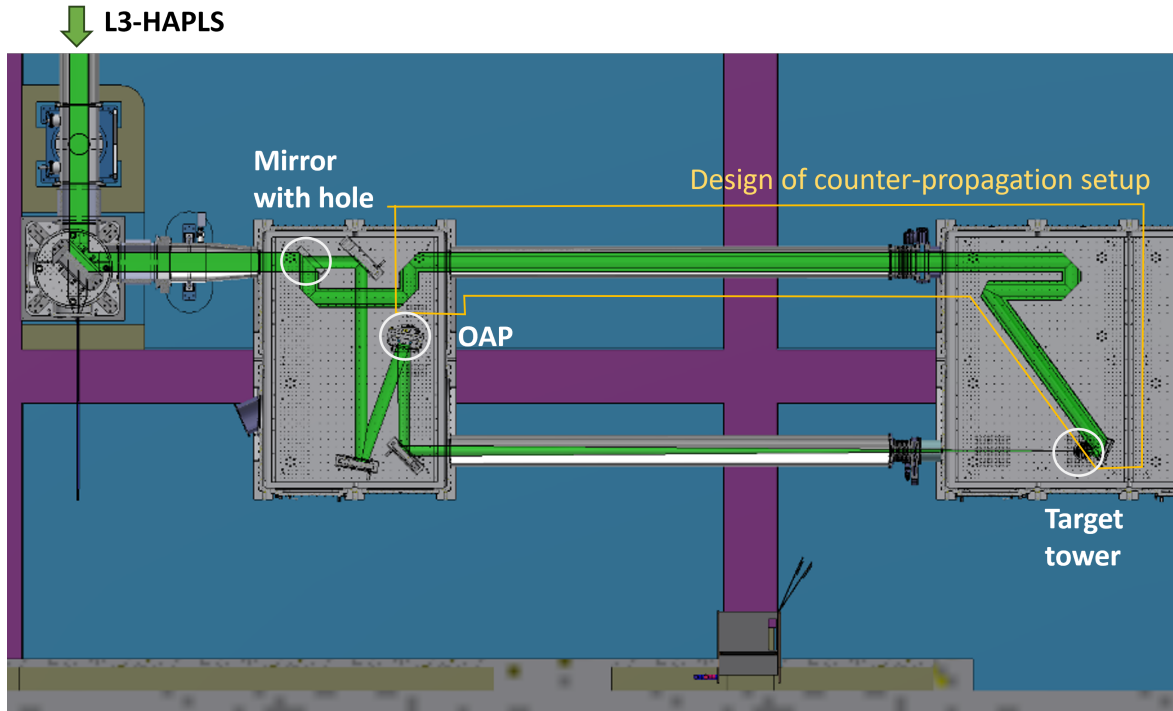
Figure 6.5: ELBA electron-photon collider full optical layout.

reaching the ELBA vacuum chamber. The ELBA optical layout is depicted in Figure 6.5. The first optical element is a 50 : 50 wavefront splitting mirror, which can be inserted before the parabola to get a secondary synchronized laser beam. The laser pulse is shaped by large-aperture dielectric mirrors. The beam is then focused by a 10-meter focal length off-axis parabola (OAP). The laser pulses are focused into in-house designed and characterized gas targets (see Sections 5.2, 5.3 and 5.4), which are mounted on a 5-axis target tower system and are supplied by gas chain setup. There is also a space allocated for a counter-propagation line in the ELBA setup, which was not built in the year 2023.

Large-aperture dielectric ultrafast mirrors

The ELBA optical setup implements 9 large-area dielectric ultrafast mirrors, from which 3 mirrors belong to the electron acceleration setup and 6 mirrors belong to the counter-propagation line. 7 of these mirrors are coated for a 45° incidence angle.

The mirror substrates are manufactured from UV Fused Silica material. The size of the substrate is $440 \times 290 \times 75$ mm. The reflective surface has a clear aperture 396×261 mm with surface quality Scratch-Dig: 20-10 according to U.S. Military Performance Specification MIL-PRF-13830B standard and surface Peak-to-Valley flatness ≤ 80 nm.

The ion beam sputtered dielectric coating applied to the 45° mirrors fulfills the following requirements:

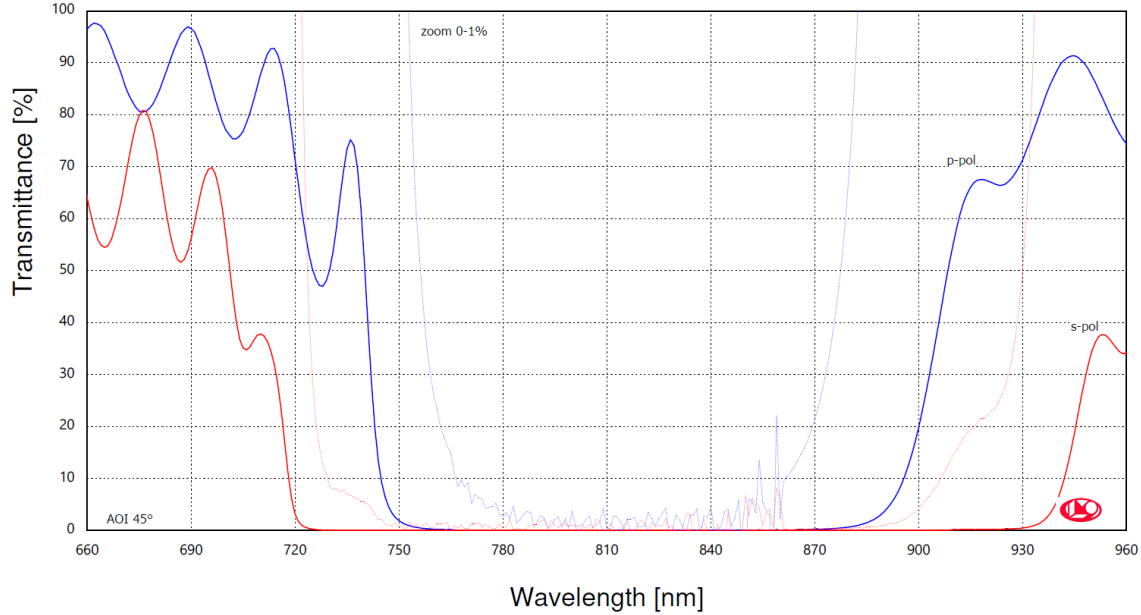- Wavelength bandwidth 772-848 nm centered at 810 nm

- Angle of incidence $45 \pm 1°$

Figure 6.6: Results of the transmittance measurement of the dielectric ultrafast 45°
mirrors coated at Laseroptik GmbH.

- Reflection for p-polarization $R_p > 99.8\%$ and s-polarization $R_s > 99.9\%$

- Group delay dispersion $GDD(R_{p,s}) < 50 fs^2$ over full bandwidth

- Leakage transmission $T_p > 0.01\%$ average over full bandwidth

The result of the transmittance measurement performed by the coating supplier
is displayed in Figure 6.6. The laser-induced damage threshold (LIDT) of the mirrors
was tested with s-polarized light and has a measured multi-pulse damage threshold of
$0.9\ J/cm^2$ (42 fs, 1 kHz, 805 nm test laser, 100k shots) [105].

5-axis target tower

The ELBA setup is equipped with a 5-axis high-precision high-stiffness posi-
tioning system for gas target alignment (target tower). The target tower allows for
3 translation movements (TX-laser-axis, TY-lateral, and TZ-vertical) and 2 rotation
movements (RZ-around Z axis, RY-around Y axis). The stages were designed to achieve
$1\ \mu m$ resolution and great repeatability of the positions obtained by using a backlash
compensation strategy in the software (the movements always finish in the same direc-
tion). The functional parameters of each stage are summarized in Table 6.4.

Each movement is obtained thanks to stepper motor gear (VSS type from Phytron
Company). Motor gears are resistant to EMP radiation up to 10^2 J/kg. The 3 trans-
lations are obtained through a screw-nut system with a preload spring to avoid the
backlash. Guiding uses linear bearings without ball recirculation. The Z rotation is
obtained through a worm gear and the Y rotation is thanks to a dedicated goniome-
ter. These rotations also integrate a preload by spring to avoid backlash and improve

73

Axis	Range	Speed	Resolution	Repeatability
TX	20 mm	0.23 mm/s	$< 1\ \mu m$	$< 3\ \mu m$
TY	10 mm	0.23 mm/s	$< 1\ \mu m$	$< 3\ \mu m$
TZ	20 mm	0.1 mm/s	$< 1\ \mu m$	$< 3\ \mu m$
RZ	340°	0.16°/s	$< 0.001°$	$< 0.003°$
RY	10°	0.18°/s	$< 0.001°$	$< 0.003°$

Table 6.4: Summary of the performance parameters of 5-axis ELBA target tower.

stability during laser shooting. The rotation axis around Y will be located 350 ±1 mm (laser beam height above the optical table) above the target tower base while all stages are in the central position. The Z-translation has 4 high-precision guides to reach a high stiffness. The maximum payload is > 10 kg. Origins for each axis are obtained thanks to NC limit switches. Vacuum-compatible mechanical switches are used to be resistant to radiation. All the cables are also protected against EMP radiation by overall polyimide jackets.

The important dimensions of the target tower are depicted in Figure 6.7. The height of the top plate is only 220 mm above the optical table to reserve enough space for the accommodation of complex gas target systems. All the systems are clean at the ISO5-level according to ISO 14644-1 standard and are suitable for long-term high vacuum operation (10^-6 mbar).

Gas supply system

The ELBA gas delivery system, designed to supply gas targets, accommodates all inert gases and their mixtures. A schematic illustration of the gas line and its components is provided in Figure 6.8. Its crucial elements are the remote pressure controller and the vacuum-compatible high-speed gas valve. The pressure controller facilitates real-time monitoring and precise adjustment of the backing pressure within the target during experiments, achieving precision up to 1 millibar. At the terminus of the gas line (target position), the maximum allowed pressure is 60 bar. The high-speed gas valve ensures rapid and precise gas delivery to the target, with millisecond-level opening time precision. Depending on the specific requirements of the gas target, either Smartshell Co. or Parker Hannifin Corp. gas valve technology is employed. Moreover, the laboratory equipment allows for duplication of the gas delivery system, enabling the simultaneous supply of gas targets with two independently controlled gas stages.

6.2.2   Commissioning experiment 2023

The commissioning experiment for the ELBA electron acceleration beamline took place at the end of the year 2023. As of the finalization of the thesis in January 2024, the dataset, which comprises approximately 50,000 shots that are equal to 1 terabyte of data, had not been fully processed and characterized. Therefore only measured parameters of individual shots are presented here without proper statistical analysis.

The L3-HAPLS laser was running pulses with energy 10 J on target. The pulse
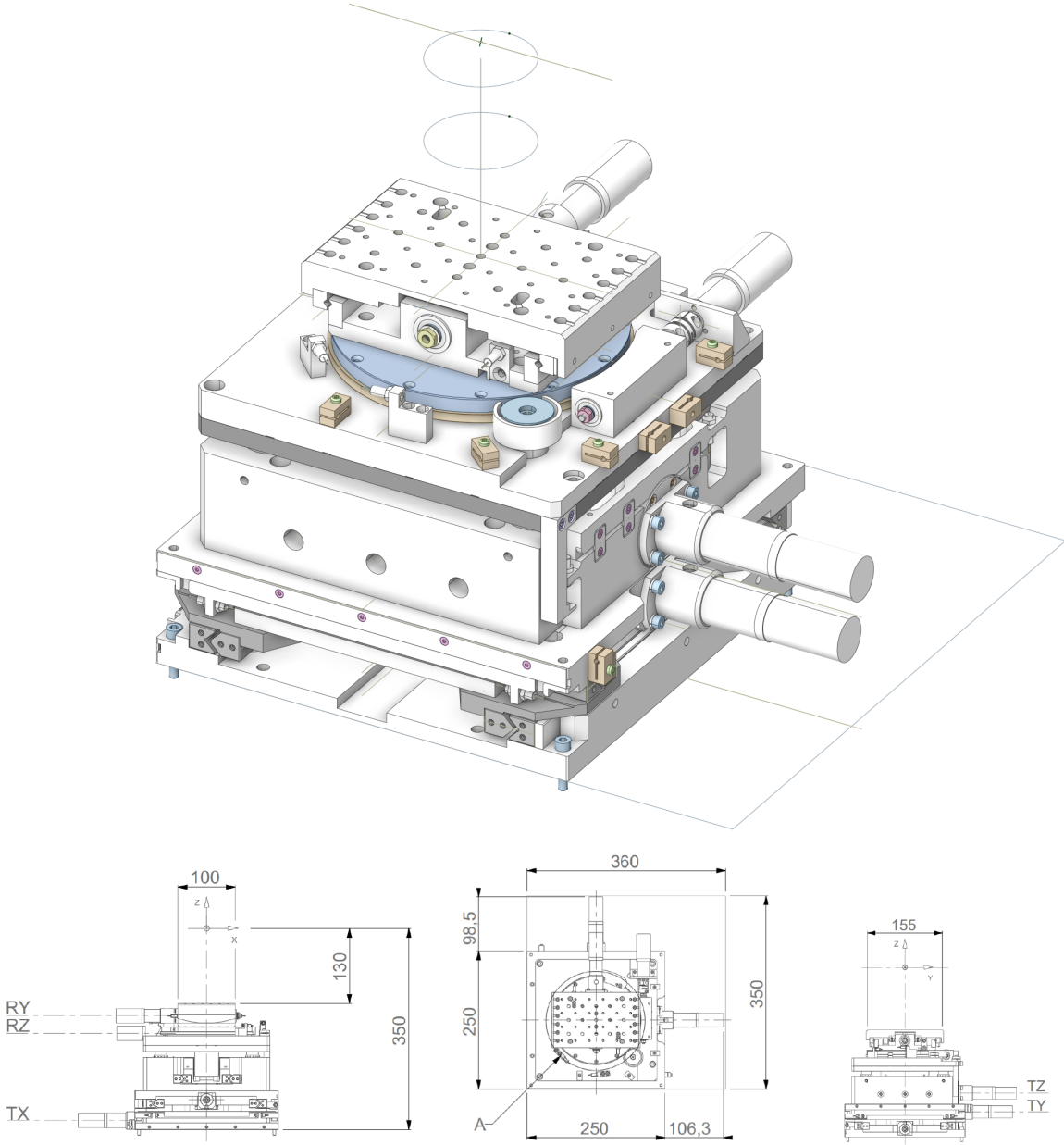
Figure 6.7: Image of ELBA 5-axis target tower 3D model and its significant dimensions(bottom).
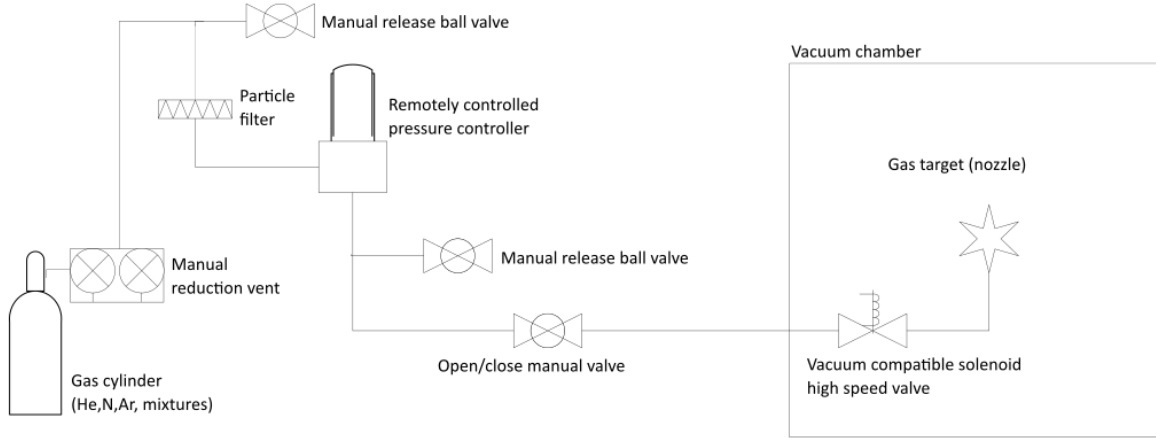
Figure 6.8: Scheme of ELBA gas supply system

duration was measured at 27.3 fs (FWHM) in the laser room after the compressor. The laser pulses were focused down by 10 m focal length off-axis parabola (OAP) to a measured focal spot size (FWHM) 22 μm and 17.5 μm along the horizontal and vertical axes, respectively. The laser power available on target was $P_{laser} = 0.35$ PW. To maintain relativistic self-focusing the electron density in the target was set as $\sim 2 \times 10^{18}$ $1/cm^3$.

The experimental setup is displayed in Figure 6.9. During this experiment, the hollow-mirror beam splitter was out of the beam path. The beam is propagating through three flat mirrors and an off-axis parabolic mirror. The laser pulse was focused on the edge of the 10 mm long slit nozzle target (see Section 5.2), approximately 1 mm above the nozzle exhaust. The gas target position has been optimized in three dimensions with a high-accuracy target tower positioning system leading to the optimal focusing position inside the plasma profile. The self-guiding phenomenon within the plasma was monitored using a top-view diagnostic. The accelerated electron beams were characterized by a calibrated electron spectrometer consisting of two motorized magnetic dipoles and a LANEX Fast Back scintillator screen. There is a beam sampler and focal spot diagnostic setup built before the target area. The remaining diverging laser light after the target is stopped by an aluminum-foil beam dump.

Given that comprehensive electron beam statistics are not yet available, we present a single representative electron beam shot is presented here. The top-view of the accelerating channel, and side-view interferometry electron spectrometer images are depicted in Figure 6.10. Evaluation of spectrometer data is presented in Figure 6.11. However, it's important to note that the current evaluation process lacks the suppression of low-energy-end noise, which requires further analysis and treatment.

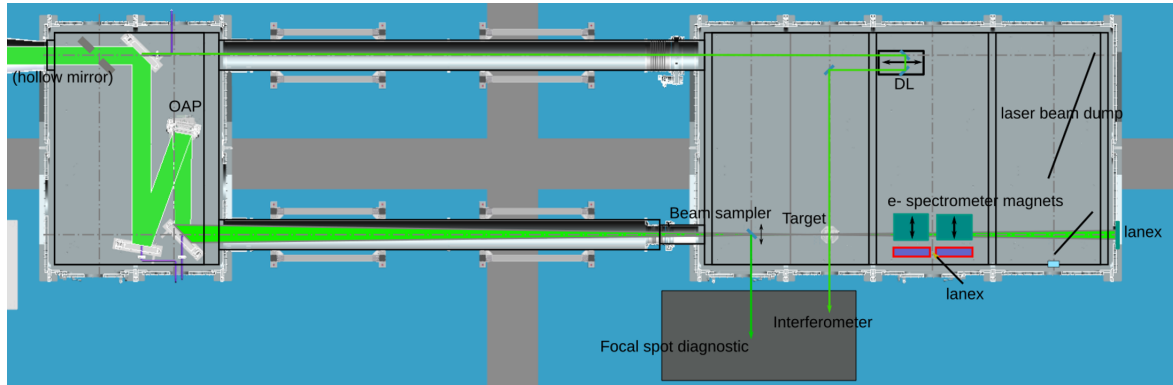Throughout the campaign, we encountered several challenges.

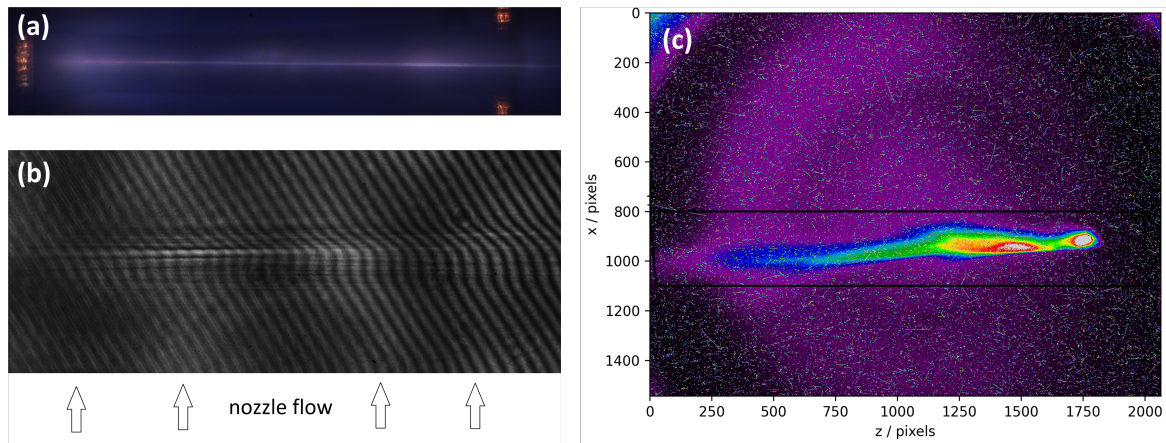Figure 6.9: ELBA 2023 commissioning experiment setup.

Figure 6.10: Raw data from ELBA diagnostics relevant to a single shot. (a) top-view of the accelerating channel, (b) side-view interferometry, and (c) record on electron spectrometer.
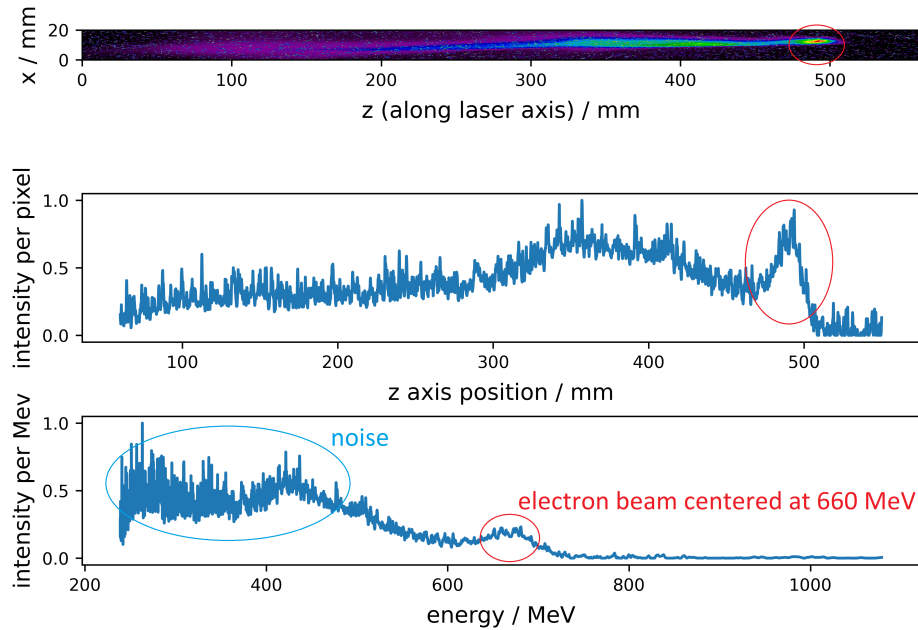
Figure 6.11: ELBA electron accelerator spectrometer image processing. The data refers to the same shot as Figure 6.10.

Plasma-generated electromagnetic pulses (EMPs) disrupting the functionality of systems

Plasma-generated electromagnetic pulses (EMPs) were causing disruptions to the functionality of both the automatic pressure regulator (APR) and the high-speed gas valve (HSGV) driver. During single-shot operation, the APR control system required frequent restarts, approximately every second shot, while the HSGV driver needed restarting after approximately every 100 shots.

The first measure taken was to apply ferrite beads to the cablings of both the APR and HSGV. This intervention significantly improved the operation of the APR, enabling approximately 100 shots to be carried out consecutively without the need for device restarts.

The second measure involved manufacturing a nonconducting adapter to connect the stainless steel nozzle with the HSGV. This adapter effectively disconnected the gas target, which is the closest device to the plasma, from the rest of the system. As a result, this additional measure completely resolved the problems, allowing for continuous operation at 3.3 Hz over extended periods of time.

Imperfect laser intensity distribution at focal spot position damaging the gas target outer shell

The natural imperfections of the laser beam and focusing optics led to a dispersion of a portion of the laser intensity beyond the intended focal spot. Despite this being only a small fraction of the laser's overall intensity, the combination of the laser's high power and repetition rate resulted in significant damage to the target. This damage

78

Figure 6.12: (a) Damage on the supersonic nozzle caused by second-order focal spot after $\sim$ 20000 shots, (b) damage on the aluminum beam-dump caused by a residual diverging laser beam after $\sim$ 20000 shots.
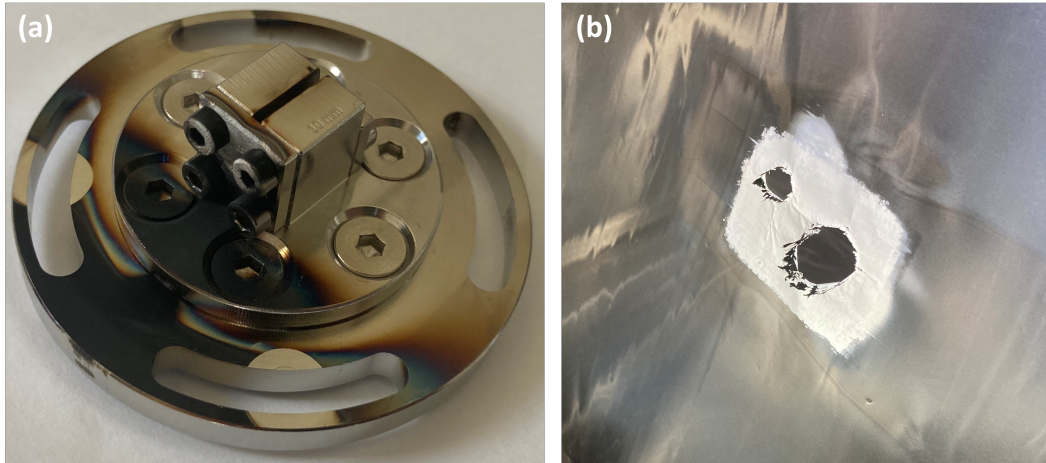
extended up to 5 mm below the focal spot position.

Figure 6.12(a) depicts the damage sustained by the nozzle after 20,000 shots. The image reveals that the front surface of the target experienced elevated temperatures, resulting in material removal of approximately 50 μm in depth. However, despite the noticeable external damage, the functionality of the target, particularly gas flow, remained unaffected throughout the entire 20,000-shot duration.

It is crucial to emphasize that a 3D printed plastic or resin nozzle would not withstand such a high repetition rate operation, primarily due to its lower melting point (approximately 200°C).

Residual diverging laser beam light ablating aluminum materials

Typically, a fraction of the laser pulse is not depleted during plasma interaction and continues to propagate (divergently) beyond the target. This poses a potential hazard for devices situated near the target, such as the magnets and the back wall of the vacuum chamber in the ELBA setup. To safeguard these components, an aluminum foil beam dump was installed on the front face of the first magnet, within the magnet surfaces, and after the magnet to intercept the central portion of the beam.

Despite orienting the foil to intercept the laser at a large angle, significant heating occurred, leading to the ablation of aluminum nanoparticles from the beam dump. These particles dispersed into the surrounding area of the aluminum components inside the vacuum chamber, posing a high risk of damaging large optical elements. Fortunately, since the major optics in the ELBA setup are housed within a separate vacuum chamber, no damage was observed on them. Nevertheless, for future ELBA experiments, it is imperative to develop a more robust beam dump to effectively mitigate the risk of damage to critical optical components.

Conclusion

At the beginning of the thesis, the principles of Laser Wakefield Electron Acceleration and injection schemes were presented. The gas target is the core part of the accelerator since the whole injection and acceleration take place inside the target. Theory and particle-in-cell simulations introduce scaling laws, which postulate theoretical demands on the targets. The role of the gas target technology development is to reach these theoretical demands. Then, the current gas target technology used for self-guided LWFA is presented. The problems and limits of each target type are addressed. The main problems of the targets are gas flow stability, gas load into the vacuum chamber, and scalability.

The development process of gas targets for LWFA consists of the following steps (see Figure 6.13):

1. Proposition of the conceptual design (in case of new solution)

2. Calculation of the desired plasma density profile shape from the theoretical scaling laws

3. Design of the target inner shape with the use of CFD simulations to achieve desired flow properties

4. Modeling of the molecular-based effects, like rarefied gas flow, heavy gas enrichment in expanding jets, or nanoparticle tracking by DSMC method

5. Performing technical particle-in-cell simulation for prediction of the accelerated electron beam parameters

6. Building product design and prototyping

7. Experimental characterization of the neutral gas flow in prototype to validate the predicted profile - the interferometry measurement method and tomographic reconstruction algorithms are used

8. Performing in-situ test of the target in the accelerator setup with plasma and electron beam diagnostics

We proved the ability of fully in-house development and implementation of gas targets for LWFA experiments.
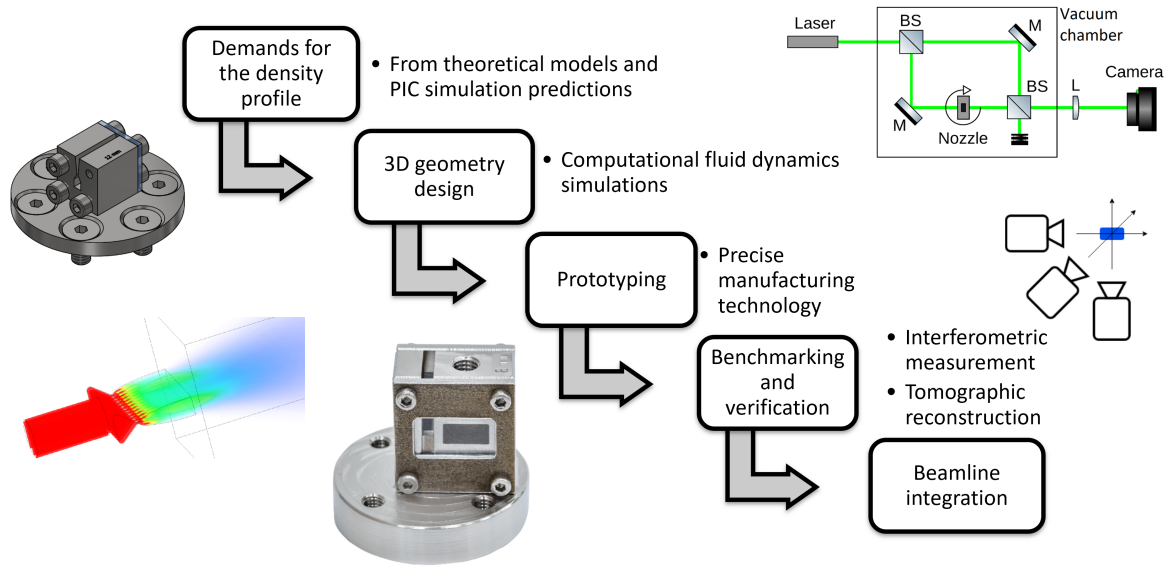
Figure 6.13: Scheme of the full in-house gas target development process.

This work also consists of improvement of the gas target development process. The DSMC rarefied gas dynamics simulation method has been successfully implemented into the process for the first time. The novel 4-pass interferometry station measurements are used to benchmark the gas target simulations. Five 3D tomographic algorithms that are typically used for target density profile reconstruction were tested and evaluated on their performance. Based on the testing, a new algorithm FARM for reconstructions from a low number of projections has been introduced.

One laser-plasma interaction diagnostic method has been experimentally investigated. We demonstrated a compact in-vacuum setup for down-collimation of a low peak intensity probe laser pulse and compression of its duration using the CafCA approach in the optimum regime from ~ 50 fs down to 18 fs while keeping the pulse synchronized in space and time with the driving laser pulse. Compression to the shortest pulses reduced the motion blur from 15 μm down to 5.4 μm, which already allows to study the density micro-structures in relativistic plasma experiments. We also characterized the shot-to-shot fluctuations. It has been proved that the down-compression allowed efficient self-phase modulation and increased the probe-to-self-emission brightness ratio, while not leading to probe image quality degradation.

Two LWFA beamlines have been assembled and commissioned in ELI Beamlines. The ELBA beamline driven by PW-class L3-HAPLS laser has been equipped with three large-aperture dielectric-coated mirrors, an ultra-stiff 5-axis target tower with μm-positioning system, and a remotely controlled complex gas supply system. The in-house developed fast slit supersonic nozzle optimized for low gas load supplied by SmartShell Co. gas valve has been implemented into the beamline. The whole electron acceleration beamline was successfully commissioned in 2023 with the electron beam parameters: up to 1 GeV energy, X pC charge, and 3.3 Hz repetition rate.

Another four gas targets suitable for PW-class laser experiments were developed (not only for future ELBA experiments):

- Slit nozzle with a gas reservoir for improved flat-top density profile generation

- Long (> 50 mm) slit nozzle with multiple inlet gas valves for multi GeV electron experiments

- Slit supersonic nozzle with injector section designed for improved electron injection into accelerating phase

- Dual-stage gas target for improved electron injection and reduced gas load into the vacuum chamber at the same time

The compact ALFA beamline driven by kHz L1-Allegra laser has been built to create an electron beam source suitable for biomedical applications. The ALFA setup implements in-house designed supersonic micro-nozzles with conical shapes and 300 μm opening. The nozzles were manufactured with electric discharge drilling technology to achieve low inner-wall surface roughness. The ALFA beamline was successfully commissioned in 2022 with the following electron beam parameters: up to 50 MeV energy, 0.28 pC charge, and 1 kHz repetition rate.

Bibliography

[1] T. Tajima and J. M. Dawson, "Laser electron accelerator", *Physical Review Letters*, vol. 43, no. 4, pp. 267–270, 1979.

[2] S. P. D. Mangles *et al.*, "Monoenergetic beams of relativistic electrons from intense laser–plasma interactions", *Nature*, vol. 431, p. 535, 2004.

[3] C. G. R. Geddes *et al.*, "High-quality electron beams from a laser wakefield accelerator using plasma-channel guiding", *Nature*, vol. 431, p. 538, 2004.

[4] J. Faure *et al.*, "A laser–plasma accelerator producing monoenergetic electron beams", *Nature*, vol. 431, p. 541, 2004.

[5] A. J. Gonsalves *et al.*, "Petawatt laser guiding and electron beam acceleration to 8 gev in a laser-heated capillary discharge waveguide", *Physical Review Letters*, vol. 122, p. 084801, 2019.

[6] B. Miao *et al.*, "Multi-gev electron bunches from an all-optical laser wakefield accelerator", *Physical Review X*, vol. 12, p. 031038, 2022.

[7] W. Wang *et al.*, "Free-electron lasing at 27 nanometeres based on a laser wakefield accelerator", *Nature*, vol. 595, p. 516, 2021.

[8] A. R. Maier *et al.*, "Decoding sources of energy variability in a laser-plasma accelerator", *Physical Review X*, vol. 10, p. 031039, 2020.

[9] D. Guénot *et al.*, "Relativistic electron beams driven by kHz single-cycle light pulses", *Nature Photonics*, vol. 11, no. 5, pp. 293–296, 2017.

[10] F. Salehi *et al.*, "Laser-accelerated, low-divergence 15-mev quasimonoenergetic electron bunches at 1 khz", *Physical Review X*, vol. 11, p. 021055, 2021.

[11] F. Brandi and L. A. Gizzi, "Optical diagnostics for density measurement in high-quality laser-plasma electron accelerators", *High Power Laser Science and Engineering*, vol. 7, no. e26, 2019.

[12] K. Iwata, "Chapter 6 - phase imaging and refractive index tomography for x-rays and visible rays", vol. 47 of *Progress in Optics*, pp. 393–432, Elsevier, 2005.

[13] B. Landgraf *et al.*, "High resolution 3D gas-jet characterisation", *Review of Scientific Instruments*, vol. 82, p. 083106, 2011.

[14] J. P. Couperus *et al.*, "Tomographic characterisation of gas-jet targets for laser wakefield acceleration", *Nuclear Instruments and Methods in Physics Research Section A: Accelerators, Spectrometers, Detectors and Associated Equipment*, vol. 830, pp. 504–509, 2016.

[15] A. Adelmann *et al.*, "Real-time tomography of gas-jets with a wollaston interferometer", *Applied Sciences*, vol. 8, no. 3, 2018.

[16] *Web page of Center for Ultrafast Optical Science, Michigen University*, accessed April 20, 2019. `https://cuos.engin.umich.edu/researchgroups/hfs/research/laser-wakefield-acceleration/`.

[17] A. Popp, *Dynamics of electron acceleration in laser-driven wakefields: Acceleration limits and asymmetric plasma waves*. PhD thesis, LMU Munich, 2011.

[18] F. F. Chen, *Introduction to Plasma Physics and Controlled Fusion*. Springer US, 2 ed., 1984.

[19] E. Esarey *et al.*, "Physics of laser-driven plasma-based electron accelerators", *Reviews of Modern Physics*, vol. 81, pp. 1229–1285, 2009.

[20] J. M. Dawson, "Nonlinear electron oscillations in a cold plasma", *Physical Review*, vol. 113, pp. 383–387, 1959.

[21] A. Akhiezer and R. Polovin, "Theory of wave motion of an electron plasma", *Soviet Physics - JETP*, vol. 3, no. 5, 1956.

[22] S. Bulanov *et al.*, "Particle injection into the wave acceleration phase due to nonlinear wake wave breaking", *Physical Review E*, vol. 58, pp. R5257–R5260, 1998.

[23] J. Vyskočil, *Simulace urychlování elektronů při interakci krátkých laserových pulsů s plynem*. Bachelor's thesis, KFE, FNSPE, CTU in Prague, 2009.

[24] W. Lu *et al.*, "Generating multi-gev electron bunches using single stage laser wakefield acceleration in a 3d nonlinear regime", *Physical Review Accelerators and Beams*, vol. 10, p. 061301, 2007.

[25] J. Faure *et al.*, "Controlled injection and acceleration of electrons in plasma wakefields by colliding laser pulses", *Nature*, vol. 444, pp. 737–739, 2006.

[26] C. McGuffey *et al.*, "Ionization induced trapping in a laser wakefield accelerator", *Physical Review Letters*, vol. 104, p. 025004, 2010.

[27] A. J. Gonsalves *et al.*, "Tunable laser plasma accelerator based on longitudinal density tailoring", *Nature Physics*, vol. 7, pp. 862–866, 2011.

[28] M. Chen *et al.*, "Electron injection and trapping in a laser wakefield by field ionization to high-charge states of gases", *Journal of Applied Physics*, vol. 99, no. 5, p. 056109, 2006.

[29] M. Chen *et al.*, "Theory of ionization-induced trapping in laser-plasma accelerators", *Physics of Plasmas*, vol. 19, no. 3, p. 033101, 2012.

[30] K. Schmid *et al.*, "Density-transition based electron injector for laser driven wakefield accelerators", *Physical Review Special Topics - Accelerators and Beams*, vol. 13, no. 091301, pp. 1–5, 2010.

[31] M. H. Cho. *et al.*, "Controlled electron injection facilitated by nanoparticles for laser wakefield acceleration", *Scientific Reports*, no. 8, p. 16924, 2018.

[32] C. Aniculaesei *et al.*, "Novel gas target for laser wakefield accelerators", *Review of Scientific Instruments*, vol. 89, p. 025110, 2018.

[33] C. Aniculaesei *et al.*, "The acceleration of a high-charge electron bunch to 10 gev in a 10-cm nanoparticle-assisted wakefield accelerator", *Matter and Radiation at Extremes*, vol. 9, p. 014001, 2024.

[34] Y. Fukuda *et al.*, "Ultrarelativistic electron generation during the intense, ultrashort laser pulse interaction with clusters", *Physics Letters A*, vol. 363, no. 1, pp. 130–135, 2007.

[35] T. M. York and H.-B. Tang, "Chapter 8 - hydromagnetics—fluid behavior of plasmas", in *Introduction to Plasmas and Plasma Dynamics*, pp. 137–193, Oxford: Academic Press, 2015.

[36] S. Lorenz, *Design of a gas target for laser-plasma electron acceleration.* Research project, KFE, FNSPE, CTU in Prague, 2018.

[37] B. Beaurepaire *et al.*, "Effect of the laser wave front in a laser-plasma accelerator", *Phys. Rev. X*, vol. 5, p. 031012, 2015.

[38] A. Golovanov *et al.*, "Design of a gas cell for laser wakefield acceleration of electrons", *Problems of Atomic Science and Technology*, vol. 116, pp. 70–75, 01 2018.

[39] T. Audet *et al.*, "Gas cell density characterization for laser wakefield acceleration", *Nuclear Instruments and Methods in Physics Research Section A: Accelerators, Spectrometers, Detectors and Associated Equipment*, vol. 909, pp. 383 – 386, 2018.

[40] M. Vargas *et al.*, "Improvements to laser wakefield accelerated electron beam stability, divergence, and energy spread using three-dimensional printed two-stage gas cell targets", *Applied Physics Letters*, vol. 104, no. 17, p. 174103, 2014.

[41] J. Daniels, *Capillary waveguide improvements for laser plasma accelerators.* MSc thesis, Eindhoven University of Technology, 2013.

[42] D. J. Spence *et al.*, "First demonstration of guiding of high-intensity laser pulses in a hydrogen-filled capillary discharge waveguide", *Journal of Physics B: Atomic, Molecular and Optical Physics*, vol. 34, no. 21, p. 4103, 2001.

[43] W. Leemans *et al.*, "Gev electron beams from a centimetre-scale accelerator", *Nature Physics*, vol. 2, 09 2006.

[44] W. P. Leemans *et al.*, "Multi-GeV electron beams from capillary-discharge-guided subpetawatt laser pulses in the self-trapping regime", *Physical Review Letters*, vol. 113, p. 245002, 2014.

[45] K. Schmid, *Supersonic Micro-Jets and Their Application to Few-Cycle Laser-Driven Electron Acceleration*. PhD thesis, LMU Munich, 2009.

[46] F. Salehi *et al.*, "Characterization of a 100 micrometer-scale cryogenically cooled gas jet for near-critical density laser-plasma experiments", *Review of Scientific Instruments*, vol. 90, p. 103001, 2019.

[47] C. Thaury *et al.*, "Shock assisted ionization injection in laser-plasma accelerators", *Scientific Reports*, no. 5, p. 16310, 2015.

[48] S. Semushin and V. Malka, "High density gas jet nozzle design for laser target production", *Review of Scientific Instruments*, vol. 72, no. 7, pp. 2961–2965, 2001.

[49] K. Schmid and L. Veisz, "Supersonic gas jets for laser-plasma experiments", *Review of Scientific Instruments*, vol. 83, no. 5, p. 053304, 2012.

[50] F. Sylla *et al.*, "Development and characterization of very dense submillimetric gas jets for laser-plasma interaction", *Review of Scientific Instruments*, vol. 83, no. 3, p. 033507, 2012.

[51] W. T., *High-gradient gas-jet targets for laser wakefield acceleration*. Master's thesis, University of Twente, 2011.

[52] R. Azambuja *et al.*, "Three-dimensional characterisation of high-density non-cylindrical pulsed gas jets", *Journal of Physics D: Applied Physics*, vol. 32, 1999.

[53] G. Golovin *et al.*, "Tomographic imaging of nonsymmetric multicomponent tailored supersonic flows from structured gas nozzles", *Applied optics*, vol. 54, no. 11, pp. 3491–3497, 2015.

[54] S. Lorenz *et al.*, "Characterization of supersonic and subsonic gas targets for laser wake field electron acceleration experiments", *Matter and Radiation at Extremes*, vol. 4, p. 015401, 2019.

[55] G. Grittani *et al.*, "High energy electrons from interaction with a structured gas-jet at flame", *Nuclear Instruments and Methods in Physics Research Section A: Accelerators, Spectrometers, Detectors and Associated Equipment*, vol. 740, pp. 257–265, 2014. Proceedings of the first European Advanced Accelerator Concepts Workshop 2013.

[56] G. Bird, "Molecular gas dynamics and the direct simulation of gas flows", 1994.

[57] A. Garcia and F. Baras, "Direct simulation monte carlo: Novel applications and new extensions", *Proceedings of the Third Workshop on Modelling of Chemical Reaction Systems, Heidelberg*, 1997.

[58] C. White *et al.*, "dsmcfoam+: An openfoam based direct simulation monte carlo solver", *Computer Physics Communications*, vol. 224, pp. 22–43, 2018.

[59] M. Sabouri and M. Darbandi, "Numerical study of species separation in rarefied gas mixture flow through micronozzles using dsmc", *Physics of Fluids*, vol. 31, no. 4, p. 042004, 2019.

[60] J. Fernandez de la Mora and J. Rosell-Llompart, "Aerodynamic focusing of heavy molecules in seeded supersonic jets", *The Journal of Chemical Physics*, vol. 91, no. 4, pp. 2603–2615, 1989.

[61] S. Karatodorov *et al.*, "Multi-pass probing for high-sensitivity tomographic interferometry", *Scientific Reports*, vol. 11, no. 15072, 2021.

[62] J. Couperus *et al.*, "Tomographic characterisation of gas-jet targets for laser wakefield acceleration", *Nuclear Instruments and Methods in Physics Research Section A: Accelerators, Spectrometers, Detectors and Associated Equipment*, vol. 830, pp. 504 – 509, 2016.

[63] Y. M. Li and R. Fedosejevs, "Density measurements of a high-density pulsed gas jet for laser-plasma interaction studies", *Measurement Science and Technology*, vol. 5, pp. 1197–1201, 1994.

[64] S. Lorenz *et al.*, "Tomographic reconstruction algorithms for structured gas density profiles of the targets for laser wakefield acceleration", *Measurement Science and Technology*, vol. 31, p. 085205, jun 2020.

[65] A. C. Kak, *Principles of Computerized Tomographic Imaging*. 2001.

[66] D. Gottleib *et al.*, "On the direct fourier method for computer tomography", *IEEE Transactions and Medical Imaging*, vol. 19, no. 3, pp. 223–232, 2000.

[67] L. A. Shepp *et al.*, "The fourier reconstruction of a head section", *IEEE Transactions on Nuclear Science*, vol. 21, no. 3, pp. 21–43, 1974.

[68] S. Kaczmarz, "Angenäherte auflösung von systemen linearer gleichungen", *Bull Acad. Pol. Sci. Lett. A*, vol. 6-8A, pp. 355–357, 1937.

[69] R. Gordon *et al.*, "Algebraic reconstruction techniques (ART) for three-dimensional electron microscopy and x-ray photography", *Journal of Theoretical Biology*, vol. 29, no. 3, pp. 471 – 481, 1970.

[70] P. Gilbert, "Iterative methods for the three-dimensional reconstruction of an object from projections", *Journal of theoretical biology*, vol. 36, pp. 105–17, 08 1972.

[71] D. Verhoeven, "Limited-data computed tomography algorithms for the physical sciences", *Applied optics*, vol. 32, pp. 3736–3754, 1993.

[72] D. Mishra *et al.*, "A robust mart algorithm for tomographic applications", *Numerical Heat Transfer, Part B: Fundamentals*, vol. 35, no. 4, pp. 485–506, 1999.

[73] A. Buck *et al.*, "Real-time observation of laser-driven electron acceleration", *Nature Physics*, vol. 7, no. 7, pp. 543–548, 2011.

[74] N. H. Matlis *et al.*, "Snapshots of laser wakefields", *Nature Physics*, vol. 2, no. 11, pp. 749–753, 2006.

[75] M. F. Gilljohann *et al.*, "Direct observation of plasma waves and dynamics induced by laser-accelerated electron beams", *Physical Review X*, vol. 9, no. 1, 2019.

[76] A. Sävert *et al.*, "Direct observation of the injection dynamics of a laser wakefield accelerator using few-femtosecond shadowgraphy", *Physical Review Letters*, vol. 115, p. 055002, 2015.

[77] J. Xu *et al.*, "Dynamics of electron injection in a laser- wakefield accelerator", *Physics of Plasmas*, vol. 24, p. 083106, 2017.

[78] M. C. Kaluza *et al.*, "Measurement of magnetic-field structures in a laser-wakefield accelerator", *Physical Review Letters*, vol. 105, no. 11, 2010.

[79] M. C. Downer *et al.*, "Diagnostics for plasma-based electron accelerators", *Reviews of Modern Physics*, vol. 90, no. 3, 2018.

[80] M. Kando *et al.*, "Demonstration of laser-frequency upshift by electron-density modulations in a plasma wakefield", *Physical Review Letters*, vol. 99, p. 135001, 2007.

[81] A. S. Pirozhkov *et al.*, "Frequency multiplication of light back-reflected from a relativistic wake wave", *Physics of Plasmas*, vol. 14, p. 123106, 2007.

[82] A. S. Pirozhkov *et al.*, "Burst intensification by singularity emitting radiation in multi-stream flows", *Scientific Reports*, vol. 7, p. 17968, 2017.

[83] A. Sagisaka *et al.*, "Observation of burst intensification by singularity emitting radiation generated from relativistic plasma with a high-intensity laser", *High Energy Density Physics*, vol. 36, p. 100751, 2020.

[84] T. Z. Esirkepov *et al.*, "Optical probing of relativistic plasma singularities", *Physics of Plasmas*, vol. 27, no. 5, p. 052103, 2020.

[85] R. A. Fisher *et al.*, "Subpicosecond pulse generation using the optical kerr effect", *Applied Physics Letters*, vol. 14, no. 4, pp. 140–143, 1969.

[86] T. Nagy *et al.*, "High-energy few-cycle pulses: post-compression techniques", *Advances in Physics: X*, vol. 6, no. 1, 2020.

[87] R. Szipöcs *et al.*, "Chirped multilayer coatings for broadband dispersion control in femtosecond lasers", *Optics Letters*, vol. 19, no. 3, p. 201, 1994.

[88] R. Szipöcs and A. Köhazi-Kis, "Theory and design of chirped dielectric laser mirrors", *Applied Physics B: Lasers and Optics*, vol. 65, no. 2, pp. 115–135, 1997.

[89] N. Matuschek *et al.*, "Theory of double-chirped mirrors", *IEEE Journal of Selected Topics in Quantum Electronics*, vol. 4, no. 2, pp. 197–208, 1998.

[90] M. B. Schwab *et al.*, "Few-cycle optical probe-pulse for investigation of relativistic laser-plasma interactions", *Applied Physics Letters*.

[91] D. R. Symes *et al.*, "Operation of the astra ta2 hollow fibre pulse compressor with increased pump energy", *CLF Annual Report 2008/2009*, no. S7, p. 229, 2009.

[92] J. I. Kim *et al.*, "Sub-10 fs pulse generation by post-compression for peak-power enhancement of a 100-tw ti:sapphire laser", *Optics Express*, vol. 30, no. 6, p. 8734, 2022.

[93] E. A. Khazanov *et al.*, "Nonlinear compression of high-power laser pulses: compression after compressor approach", *Phyhics-Uspekhi*, vol. 62, no. 11, pp. 1096–1124, 2019.

[94] A. V. Kotov *et al.*, "Enhanced diagnostics of radiating relativistic singularities and biser by nonlinear post-compression of optical probe pulse", *Journal of Instrumentation*, vol. 17, no. 7, p. 07035, 2022.

[95] M. B. Schwab *et al.*, "Visualization of relativistic laser pulses in underdense plasma", *Physical Review Accelerators and Beams*, vol. 23, no. 3, 2020.

[96] T. Nagy *et al.*, "Generation of above-terawatt 1.5-cycle visible pulses at 1 khz by post-compression in a hollow fiber", *Optics Letters*, vol. 45, 2020.

[97] S. Lorenz *et al.*, "In-vacuum post-compression of optical probe pulse for relativistic plasma diagnostics", *Optica Open*, 2023. https://doi.org/10.1364/opticaopen.23559879.v2.

[98] A. S. Pirozhkov *et al.*, "Approaching the diffraction-limited, bandwidth-limited petawatt", *Optics Express*, vol. 25, no. 17, p. 20486, 2017.

[99] H. Kiriyama *et al.*, "Enhancement of pre-pulse and picosecond pedestal contrast of the petawatt j-karen-p laser", *High Power Laser Science and Engineering*, vol. 9, 2021.

[100] A. Moulet *et al.*, "Single-shot, high-dynamic-range measurement of sub-15 fs pulses by self-referenced spectral interferometry", *Optics Letters*, vol. 35, no. 22, p. 3856, 2010.

[101] Z. Bor, "Distortion of femtosecond laser pulses in lenses and lens systems", *Journal of Modern Optics*, vol. 35, no. 12, pp. 1907–1918, 1988.

[102] Z. Bor, "Distortion of femtosecond laser pulses in lenses", *Optics Letters*, vol. 14, no. 2, p. 119, 1989.

[103] R. Antipenkov *et al.*, "TW-class Allegra Laser System at ELI-Beamlines", in *High Power Lasers and Applications*, vol. 11777, p. 117770E, SPIE, 2021.

[104] C. M. Lazzarini *et al.*, "50 MeV electron beams accelerated by a terawatt scalable khz laser", *arXiv:2302.11415*, 2023.

[105] T. Willemsen *et al.*, "Large area ion beam sputtered dielectric ultrafast mirrors for petawatt laser beamlines", *Optics Express*, vol. 30, no. 4, pp. 6129–6141, 2022.

Curriculum vitae

Sebastian Lorenz

Private contact

Address:	Zahradní 356, 683 52 Šaratice, Czech Republic
Phone:	+420 773 123 560
Email:	sebastianlorenz686@gmail.com

Professional contact

Institute:	Extreme Light Infrastructure ERIC, ELI Beamlines Facility
Address:	Za Radnicí 835, 252 41 Dolní Břežany, Czech Republic
Email:	sebastian.lorenz@eli-beams.eu

Education

PhD student   **since 10/2019**

Czech Technical University in Prague, Faculty of Nuclear Sciences and Physical Engineering

Main research field: Development of gas-targets for laser-driven electron acceleration.

Supervisor: prof. Ing. Jiří Limpouch, CSc.

Master's degree 10/2017-6/2019
Czech Technical University in Prague, Faculty of Nuclear Sciences and Physical Engineering
Study branch: Computational Physics

Bachelor's degree 10/2014-9/2017
Czech Technical University in Prague, Faculty of Nuclear Sciences and Physical Engineering
Study branch: Computational Physics

High school 9/2010-6/2014
Gymnázium Brno, třída Kapitána Jaroše
Mathematical gymnasium with leaving examination

Experience

Research assistant since 5/2019
Extreme Light Infrastructure ERIC, ELI Beamlines Facility   Dolní Břežany, Czech Republic
Neutral gas flow modeling, complex systems setup, experimental activities, presentations on conferences

Long-term student internship 9/2016-4/2019
Czech Academy of Sciences, Institude of Physics, ELI Beamlines project   Dolní Břežany, Czech Republic
Neutral gas flow modeling and experimental activities

Skills

- Languages: Czech (native speaker), English (advanced), German (intermediate)

- Programming skills: MATLAB (advanced), Python (intermediate), C++(intermediate), LaTeX (advanced), UNIX (intermediate)

- Advanced knowledge of ANSYS Fluent and OpenFoam simulation software

- Driver's license (B)

Publication list

Journal articles

- **S. Lorenz**, G. Grittani, E. Chacon-Golcher, C. M. Lazzarini, J. Limpouch, F. Nawaz, M. Nevrkla, L. Vilanova, T. Levato, "Characterization of supersonic and subsonic gas targets for laser wakefield electron acceleration experiments", Matter and Radiation at Extremes 4, 015401 (2019), DOI: 10.1063/1.5081509

- **S. Lorenz**, G. Grittani, L. V. Goncalves, C. M. Lazzarini, J. Limpouch, M. Nevrkla, S. Bulanov, G. Korn, "Tomographic reconstruction algorithms for structured gas density profiles of the targets for laser wakefield acceleration", Measurement Science and Technology 31, 085205 (2020), DOI: 10.1088/1361-6501/ab7cf5

- S. Karatodorov, R. Lera, M. Raclavsky, **S. Lorenz**, U. Chaulagain, J. Nejdl, "Multi-pass probing for high-sensitivity tomographic interferometry", Scientific Reports 11, 15072 (2021), DOI: 10.1038/s41598-021-94436-6

- C. M. Lazzarini, G. M. Grittani, P. Valenta, I. Zymak, R. Antipenkov, U. Chaulagain, L. V. N. Goncalves, A. Grenfell, M. Lamac, **S. Lorenz**, M. Nevrkla, V. Sobr, A. Spacek, W. Szuba, P. Bakule, G. Korn and S. V. Bulanov, "50 MeV electron beams accelerated by a terawatt scalable kHz laser", arXiv:2302.11415 (2023)

- **S. Lorenz**, G. Grittani, K. Kondo, A. Kon, Y.-K. Liu, A. Sagisaka, K. Ogura, N. Nakanii, K. Huang, A. Bierwage, S. Namba, H. Ohiro, T. Pikuz, J. Koga, P. Chen, H. Kiriyama, M. Kando, T. Esirkepov, S. Bulanov, A. Pirozhkov, "In-vacuum post-compression of optical probe pulse for relativistic plasma diagnostics", OpticaOpen.23559879.v2 (2023)

Patent

- **S. Lorenz**, G. M. Grittani, "Gas target for laser controlled electron accelerators and method of accelerating electrons", CZ national patent n. 2021-247, published 30th November 2022, ISSN 2336-7288

Conference papers

- C. M. Lazzarini, L. V. Goncalves, G. M. Grittani, **S. Lorenz**, M. Nevrkla, P. Valenta, T. Levato, S. V. Bulanov, G. Korn, "Electron acceleration at ELI-Beamlines: Towards high-energy and high-repetition rate accelerators", International Journal of Modern Physics A 34, 1943010 (2019), DOI: 10.1142/S0217751X19430103

- U. Chaulagain, S. Karatodorov, M. Raclavsky, **S. Lorenz**, M. Lamac, M. Albrecht, V. Tomkus, J. Dudutis, M. Mackeviciute, P. Gecys, J. Nejdl, "Tomographic characterization of gas jets for laser-plasma acceleration with increased sensitivity", Proceedings Volume 11886, International Conference on X-Ray Lasers 2020; 118860A (2021), DOI: 10.1117/12.2592861

Conference presentations

- Oral talk titled "Computational Fluid Dynamics Simulations for LWFA Gas Target Development" delivered at the International Conference on Extreme Light (2019, Dolní Břežany, Czech Republic)

- Poster presentation titled "Tomographic Reconstruction Algorithms for Laser Wakefield Acceleration Gas Targets" delivered at the OSA High-Brightness Sources and Light-Driven Interactions Congress (2020, online)

- Poster presentation titled "Development of Gas Targets for Stable Laser Wakefield Electron Acceleration at ELI-Beamlines" delivered at the Laser and Accelerators Workshop (2023, Lagos, Portugal)

- Oral talk titled "Development of Gas Targets for Stable Laser Wakefield Electron Acceleration" delivered at the SPIE Optics + Optoelectronics Conference (2023, Prague, Czech Republic)